The Pennsylvania State University

The Graduate School

Department of Engineering Science and Mechanics

NUMERICAL SIMULATION OF SOLID-STATE SINTERING OF METAL POWDER COMPACT DOMINATED BY GRAIN BOUNDARY DIFFUSION

A Thesis in

Engineering Science and Mechanics

by

Rui Zhang

Submitted in Partial Fulfillment
of the Requirements
for the Degree of

Doctor of Philosophy

December 2005

The thesis of Rui Zhang was reviewed and approved* by the following:

Reneta S. Engel
Professor of Engineering Science and Mechanics
Thesis Advisor
Chair of Committee

Randall M. German
Brush Chair Professor in Materials

Nicholas J. Salamon
Professor of Engineering Science and Mechanics

Clifford J. Lissenden
Associate Professor of Engineering Science and Mechanics

Panagiotis Michaleris
Associate Professor of Mechanical Engineering

Judith A. Todd
P. B. Breneman Department Head Chair
Head of the Department of Engineering Science and Mechanics

*Signatures are on file in the Graduate School

ABSTRACT

The research effort is oriented towards the modeling of metal powder sintering to accurately predict the densification and distortion of a sintered part, which is mainly due to the differential shrinkage of a green compact. This research focuses on the study of the simulation of the sintering process that is dominated by grain boundary diffusion, which is recognized as one of the dominating sintering mechanisms. Specifically, a viscoelasticity model that accounts for the microstructural grain growth has been developed to simulate the thermal induced creep deformation in sintering. Sintering stress is treated as an equivalent hydrostatic pressure that links the microscale evolution to the macroscale deformation. To support that linkage, a grain boundary counting procedure has been modified to quantify the grain size distribution. The material resistance of viscous flow is included in the model as a thermally activated process using an Arrhenius-type temperature relation to represent the apparent viscosity.

The finite element method is used to implement the simulation. Results of the compaction simulation such as shape change, residual stress and density distribution data are transferred into the sintering simulation as initial conditions. Since no extra heat source is generated during sintering, the thermal analysis is independent of the creep analysis so that an uncoupled heat transfer analysis yields time-dependent temperature fields that are used to drive the sintering simulation. The simulation is performed in ABAQUS, and an in-house FEM code (SinSolver) is used as a supporting tool and verification.

Stainless steel 316L is chosen in this research due to its wide range of industrial applications and representative sintering mechanisms. Comparison and analysis on the simulation versus the dilatometry experiments of shrinkage are consistently close and improve the understanding of when and how the sintering mechanisms act in a sintering cycle.

TABLE OF CONTENTS

LIST OF FIGURES

LIST OF TABLES

LIST OF SYMBOLS

$\mathbf{B_{nl}}$	strain operator
$\mathbf{C}$	elasticity stiffness matrix
d	grain facet size
$\mathbf{D}$	displacement gradient
E	Young's modulus
$\mathbf{E}$	green strain matrix
$\mathbf{F}$	deformation gradient
G	average grain size
$\mathbf{G_N}$	geometric operator
J	Jacobians of the reference mapping
k	Boltzmann's constant
$\mathbf{n}$	deviatoric stress potential
$\mathbf{N}$	shape function matrix
p	equivalent hydrostatic pressure
P_L	effective Laplace pressure
$\mathbf{P}$	the first Piola-Kirchhoff stress
$\tilde{q}$	Mises equivalent deviatoric stress
Q_G	activation energy for grain growth
Q_v	activation energy for viscous flow
r_0	mean radius of powder particles
R	universal gas constant
$\mathcal{R}$	the global residual
$\mathbf{R}$	the element residual
$\mathbf{S}$	the second Piola-Kirchhoff stress
$\overline{\mathbf{S}}$	the second Piola-Kirchhoff stress written in vector form
$\widetilde{\mathbf{S}}$	expanded stress matrix
T	absolute temperature
T_t	transition temperature for sintering stress
$\mathbf{U}$	element displacement
$\mathcal{U}$	global displacement
α	thermal expansion coefficient
γ	shear strain
γ_b	grain boundary diffusion energy
γ_s	surface tension energy
θ	porosity
Ω	atomic volume
$\dot{\varepsilon}_{ij}$	strain rate component
$\dot{\boldsymbol{\varepsilon}}^{cr}$	creep strain rate

$\dot{\boldsymbol{\varepsilon}}^{e}$	equivalent elastic strain rate
$\dot{\boldsymbol{\varepsilon}}^{t}$	thermal strain rate
$\boldsymbol{\varepsilon}$	green strain in engineering form
$\Delta\bar{\varepsilon}^{\mathrm{sw}}$	equivalent incremental volumetric swelling strain
$\Delta\bar{\varepsilon}^{\mathrm{cr}}$	equivalent incremental uniaxial equivalent "creep" strain
η	apparent viscosity
η_b	bulk viscosity modulus
η_s	shear viscosity modulus
η_0	pre-exponential material constant
ρ	relative density
μ	fluidity
δ_{ij}	Kronecker symbol
δD_b	grain boundary diffusion coefficient
σ	stress
$\dot{\sigma}$	stress rate
σ'_{ij}	stress deviator
σ_m	hydrostatic stress
$\sigma_{\mathbf{s}}$	sintering stress

ACKNOWLEDGEMENTS

I would like to thank Professor R.S. Engel for advising me on the thesis and am grateful to her for encouraging me throughout the duration of this research. Her devotion to research and teaching has made all the difference. I am also grateful to the members of my doctoral committee for their suggestions and encouragement during this work.

The experimental results that I present were conducted in the Center for Innovative Sintered Products at the Penn State University by Professor R.S. Engel, Professor R.M German, and Professor N.J. Salamon. I am obligated to Professor N.J. Salamon and Professor Panagiotis Michaleris for enlightening lectures on the finite element analysis. I am grateful to Dr. Yang Liu, Dr. Cathy Lu, Dr. Y.S. Kwon, Dr. Debby Blaine, Dr. Yunxin Wu, and Dr. Seong-Jin Park for interesting technical discussions. The powder metallurgy and the metallography conducted by Lou Campbell, Kristina Cowan, Chantal Binet and Yi He are appreciated. Experimental support from NSF REU students Michael Mutch, Suzie Paden, Marshal Blessing, and Brent Selby is gratefully acknowledged.

I would like to thank National Science Foundation and the Center for Innovative Sintered Products at the Penn State University for sponsoring this work (Grant No. 0200554 and Grant No. 0097610).

Finally, I would like to thank my family for all the support they gave me during my study at Penn State.

Dedication

To my love Danhong

Chapter 1

Introduction

1.1 Powder Compaction and Sintering Process

Powder metallurgy (P/M) is one of the most widely used manufacturing techniques in the metalwork industry. This technology has the potential to fabricate complex parts to close tolerances in an economical manner, especially for those metals with high melting points and high hardness levels. The specific technique of die pressing and sintering is economically one of the more attractive manufacturing methods in the P/M industry. A typical process consists of the compaction of the loose powder and the thermal treatment of the green compact.

During the compaction stage, the metal powder is physically pressed in the die to form a certain shape. However, there is no bonding between particles during this stage. Therefore, the compact is usually very weak. Often a wax binder is mixed with the powder to help form the shape. As pressure is applied, the powder in the die undergoes several stages: rearrangement of the particles, elastic deformation, plastic deformation, fragmentation (for brittle materials) or strain hardening (for ductile materials) and bulk deformation [1]. Because of the friction between the die wall and the powder and the cross-section variation, density gradients, residual stresses and cracks can occur in the green compact.

During the sintering stage, the brittle green compact is put into the furnace and heated to some temperature below the melting point, usually with a holding period. Particle bonding is formed mainly due to the atomic motions that eliminate the high surface energy associated with the powder. Several atomic motion paths have been found and categorized to six mechanisms of mass transportation according to modern sintering theory [2],[3]. Among these mechanisms, the grain boundary diffusion tends to be more important to the densification of most crystalline materials and appears to dominate the densification of many common metal powder systems.

From a macroscopic point of view, when the material consolidates during the solid-state sintering, it is inevitable that the part shrinks. If the shrinkage is uneven, the part distorts. The primary reason for the distortion is that the powder compact is not a uniform material. This inhomogeneity is due to the nonuniform density distributions that were created during compaction. It has been reported that 50-90% of the total component cost is due to extra machining to achieve the net desired shape [4]. In order to avoid an additional stage of hard machining to address the distortion and achieve the desired high densities for the industry, the process specification must be tailored to minimize density variation in the compaction stage and to provide controlled/expected shrinkage during the sintering stage.

1.2 Necessity of the Research

One of the main goals in the modern P/M industrial production process is the optimization of the processing route with respect to the geometry of the as-sintered part

thereby eliminating or reducing the need for additional machining operations and obtaining crack-free parts. The metal powder compaction and sintering stages are complicated processes and the geometry of the parts can be complex as well. Therefore, numerical methods are ideal tools to develop specific simulations of the process. As the computer technology and numerical algorithms develop rapidly nowadays, numerical tools such as the Finite Element Method (FEM) and Discrete Element Method (DEM) become more popular and powerful. They can also be combined with the other CAE techniques that are used in the manufacturing industry. Compared with the empirical optimization (trial and error method), numerical simulation is less expensive and is a more efficient use of time, especially for newly designed products.

One can distinguish three major approaches in the modeling of the sintering process: (i) microscale model (physically-based), (ii) mesoscale model (stereological), and (iii) macroscale model (phenomenological). Briefly, the scientific work performed in the first approach has advanced the fundamental understanding of thermal dynamics of sintering, such as densification kinetics, influence of externally applied forces and structure heterogeneities on sintering. However, this approach lacks practical parameters that can be directly employed in the modern P/M industry. The stereological approach numerically reconstructs the particle systems and enables a mesoscopic analysis of the evolution of the particle-particle bonding during sintering. Significant work still needs to be done before the mesoscale model becomes practical. The application of the phenomenological model enables a macroscopic analysis of powder material deformation during sintering, which has many practical uses in the P/M industry.

This research focuses on developing generalized computer models, which account for grain boundary diffusion, density gradient, residual stress and other complexities of sintering situations, to accurately simulate the dimensional changes during grain boundary diffusion dominated solid phase sintering process for metal compacts. With the consideration of the sintering stress as an equivalent hydrostatic stress that is a function of average grain size and relative density, a link is built between the microstructure evolution, i.e., grain growth mechanism, and the macroscale deformation in sintering.

1.3 Research Objectives

The final target is to build an accurate numerical model to determine the shape change, i.e., shrinkage and distortion, of the compacted metal powder parts during sintering. To achieve this objective, the following intermediate goals have been identified.

- Develop a viscoelasticity model for the simulation of the thermal induced creep behavior in sintering.
- Build links between the microscale and macroscopic descriptions of sintering. Develop the corresponding phenomenological approach in the constitutive model of sintering.
- Develop an intercept counting procedure for the grain size measurement during sintering of porous material.

- Abstract a quantitative result from the microstructure evolution of metal powder compacted parts during sintering. The result must be directly applicable to the sintering model.
- Build links between the simulations of die compaction and sintering.

1.4 Selection of the Material

Stainless steel 316L has been selected in this research. This material exhibits good corrosion resistance and creep strength. It is used extensively in the chemical industry and in power plants, particularly in advanced nuclear technology. Moreover, the sintering mechanism of stainless steel 316L is relatively simple. The process is dominated by the grain boundary diffusion mechanism and has no disturbances such as phase transformation or chemical reaction. It has practical applications in industry and is a good candidate for an academic study on sintering simulation.

1.5 Thesis Structure

The thesis consists of five chapters and four appendixes. Chapter 1 starts with an introduction to the research problem and the need for numerical simulation with the objectives laid out. Chapter 2 introduces the sintering mechanisms and reviews the sintering models. A viscoelasticity model is developed with the consideration of grain growth during sintering. Sintering stress is characterized as a hydrostatic stress and applied in the calculation of creep strain rate with a transition temperature triggering the

mechanism. Viscosity moduli are functions of relative density and apparent viscosity. Finally, the thermal profile and its effect on thermal expansion during sintering are incorporated in the model. Chapter 3 introduces the grain growth mechanism and measurement of grain growth for porous material using an intercept counting procedure based on ASTM standard E112-96. The distribution of grain size is analyzed and a curve fitting Arrhenius type equation is employed to accurately describe the grain growth behavior. Chapter 4 lays out the algorithm for the finite element method (FEM) to simulate the shrinkage and distortion in sintering. SinSolver, an in-house FEM solver developed in MATLAB is used as a supporting tool and comparison for ABAQUS. Results of 3 groups of samples made of powders with different mean particle sizes are analyzed and compared so that the particle size effect is also studied. Chapter 5 shows some conclusions and future research suggestions. In-house computer programs are developed for grain growth measurement and Sinsolver. All the codes and input parameters are attached in the appendices.

Chapter 2

Sintering Theory and Modeling

The goals of the simulation of sintering are to develop generalized computer models, which account for most of the complexities of real sintering situations, and to accurately predict the dimensional changes during solid phase sintering of metal compacts. To accomplish these goals, the continuum model should account for the significant driving mechanisms, such as creep behavior, diffusion, grain growth, and thermal expansion/contraction.

The traditional approaches [5],[6] in the theory of sintering were directed toward the investigation of the local kinetics of the process. The major concerns that affected sintering were the powder particles and pores and their interaction. The results of the particle-level research helped advance the understanding of grain growth. In the late 1970s and early 1980s, Ashby and co-workers [2],[7] established the foundation for the development of constitutive laws for the sintering of powder compacts. They considered porous bodies under surface tension and developed models for sintering densification resulting from various diffusional transport processes of the material. As one of Ashby's major contributions to the sintering modeling, a number of HIP maps have been created. They can be used to select the detailed temperature and pressure history required to achieve a certain desired final state. Coble and co-workers [8],[9] have also studied the grain and pore microstructure evolution during sintering and proposed useful conclusions that can be used to optimize sintering conditions.

In the past two decades, efforts have been made to improve the sintering process simulation and the recent studies [10] have identified that linking the microscopic mechanism with the macroscopic descriptions of sintering is one of the biggest challenges. Several research groups have made progressive contributions to the development of constitutive equations for sintering of particular powder systems. For grain boundary diffusion dominated sintering process, Riedel and co-workers [11] derived a set of constitutive equations from a microscopic model with hexagonal grains and pores at the triple points. Olevsky and co-workers [12] proposed the generalization of the rheological sintering theory by considering macroscopic factors resulting from average microstructure characteristics. Johnson and co-workers [13] linked the shrinkage rate with two separate dimensionless parameters that characterize the microstructure for grain boundary diffusion and volume diffusion dominated sintering. Cocks and co-workers [14] studied the general structure of constitutive laws for two of the dominant mechanisms for deformation and densification: power-law creep and grain boundary diffusion. A similar study was further explored by Kim and co-workers [15], who developed a set of constitutive equations for sintering densification under diffusional creep and grain boundary diffusion.

In each of these models, the kinematical constraints, externally applied forces and inhomogeneity of properties in the volume have been considered to some degree thus making the simulation study closer to the practical application. Some models have a complex system of parameters to characterize grain microstructure and diffusional creep; others have a few parameters that are relatively simpler and more intuitive. Among them, the most appropriate constitutive models for continuum systems are introduced below.

This chapter also investigates several critical components of the selected model, such as sintering driving force, transition temperature, and material resistance.

2.1 Solid Phase Sintering Mechanism

Sintering is the particle bonding that occurs during heat treatment. The bonds reduce the surface energy by removing free surface and reduce grain boundary area via grain growth. This is the sintering driving force for sintering of most metals and alloys. It is well-known that under certain suitable sintering conditions, it is possible to reduce the pore volume so that the porous material becomes denser, even to a full dense level. However, the associated dimensional change may not be desired.

The temperature needed to induce sinter bonding versus densification depends on the material and particle size. Volume conservation and surface energy minimization dictate the change during sintering. Various mass transport mechanisms have been proposed to contribute to sintering [2]. The transport mechanisms detail the paths by which mass moves, either from internal mass sources or surface sources, i.e., volume transport processes or surface transport processes. The proposed processes include surface diffusion, volume diffusion, grain boundary diffusion, viscous flow, plastic flow, and vapor transport from solid surfaces. An illustration of these sintering mechanisms based on a two-sphere sintering model can be seen in Figure **2.1**.

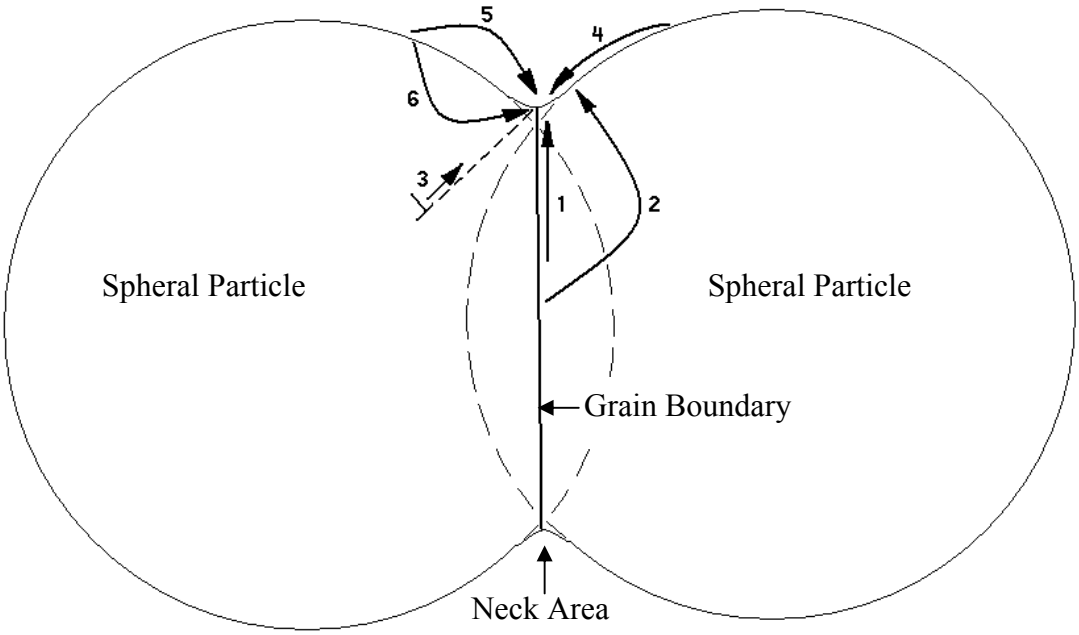

Fig. **2.1**: Sintering Mechanisms as Applied to the Two-Sphere Sintering Model. Volume Transport Processes: 1. Grain Boundary Diffusion; 2. Volume Diffusion; 3. Plastic Flow; Surface Transport Processes: 4. Surface Diffusion; 5. Evaporation-Condensation; 6. Volume Diffusion.

Based on phenomenological observations, sintering theory defines that the sintering process includes 3 sintering stages. Although there is no clear distinction between these stages, some phenomena [3] can still be used to tell the difference. In the initial sintering stage, bonding (neck) between contacting particles grows rapidly. However, the actual volume change of the porous body is small because it only takes a small mass to form a neck. It is generally characterized by a microstructure with large curvature gradients, and the grain size is no larger than the initial particle size. In the intermediate stage, the pores are smoother and become interconnected. The concomitant reduction in curvature and surface area results in slower sintering. Grain growth occurs

late in this stage. In the final stage, pores become spherical, closed, and isolated. The densification rate becomes slow and the grain growth is evident. Generalized sintering models have been developed for multiple stages of sintering, as well as particular models for certain stages.

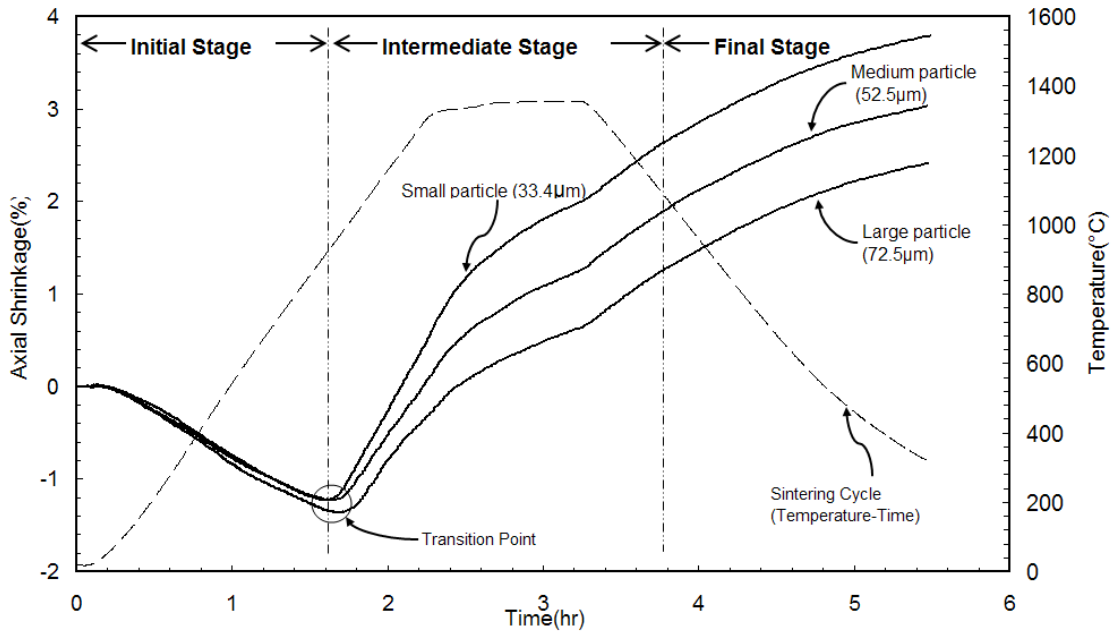

Fig. **2.2**: Stages of Sintering and Transition Point on Dilatometry Plots of Shrinkage Versus Time and Temperature: Stainless Steel 316L Powder Compact with Different Particle Mean Size Sintered in Hydrogen at 10°C/min to 1350°C with 60-min Holding.

For stainless steel 316L, because the desired density is usually low, i.e., less than 95%, the major concern is the initial and intermediate stages of sintering. For example, Figure **2.2** shows axial shrinkage curves in different sintering stages of 3 groups of stainless steel 316Lwith different mean particle sizes. No significant shrinkage occurs in the initial stage, which is only dominated by thermal expansion. While in the intermediate stage, when the temperature is higher than the transition point, the shrinkage

rate increases dramatically, thus the sintering mechanism dominates the thermal expansion. In the final stage, shrinkage due to sintering is almost zero, and thermal contraction accounts for the shrinkage. Also the mean particle size of the powder has an effect on the shrinkage.

2.2 Continuum Mechanics Based Sintering Models

Grain boundary diffusion is the dominant sintering mechanism for stainless steel 316L. Several continuum mechanics based sintering models which incorporate grain boundary diffusion have been developed in the past two decades. Three of those models will be presented in detail, because they have direct application to the viscoelasticity model that accounts for the grain boundary diffusion mechanism for the simulation of sintering stainless steel 316L.

2.2.1 Riedel and Co-workers' Model [11]

Based on a simple two-dimensional hexagonal grain structure with pores at the triple points, Riedel employed an isotropic linear viscous constitutive equation to describe sintering dominated by grain boundary diffusion. With the assumption that the local stresses on the boundaries are equilibrated with the macroscopic stresses, the relation between macroscopic stresses and strain rates was defined as:

$$\dot{\varepsilon}_{ij} = \frac{12\Omega\delta D_b}{\sqrt{3}kTd_f{}^3(1-\omega)^3}\left\{2\sigma'_{ij} + \delta_{ij}\left[\sigma_m - (1-\omega)\sigma_s\right]\right\}, \qquad \text{Eq. } \mathbf{2.1}$$

where Ω is atomic volume, δD_b is the grain boundary diffusion coefficient, k is Boltzmann's constant, T is temperature, d_f is the grain facet size, ω is an abbreviation describing the cavitated area fraction of grain boundaries and function of the average pore size, σ'_{ij} is the deviatoric stress, σ_m is the hydrostatic stress, σ_s is the sintering stress, and δ_{ij} is the Kronecker symbol.

With the consideration of the effect of relative density and pore size distribution, the strain rate equation was later [16] revised as

$$\dot{\varepsilon}_{ij} = \frac{\sigma'_{ij}}{2\eta_s} + \delta_{ij}\frac{\sigma_m - \sigma_s}{3\eta_b} \quad , \qquad \text{Eq. } \mathbf{2.2}$$

where η_s and η_b are the viscous shear modulus and bulk modulus, respectively,

$$\eta_s = \frac{\sqrt{3}kT(1-\omega)^3 d^3}{48\Omega\delta D_b}, \qquad \text{Eq. } \mathbf{2.3}$$

$$\eta_b = \frac{4\eta_s}{3}\left(\frac{1-\rho_1}{1-\rho}\right)^{\frac{m+1}{m+5/3}}, \qquad \text{Eq. } \mathbf{2.4}$$

where ρ is the relative density, ρ_1 is a reference density, and m is a parameter that characterizes the shape of the pore size distribution function.

Riedel's model considered the effect of pore size distribution on the sintering process dominated by grain boundary diffusion. This model obtained qualitatively reasonable predictions of the shape distortion after sintering; however, grain growth was not taken into account.

2.2.2 Johnson and Co-workers' Model [13]

Based on the general flux equation [6] and the rationale of conversion of atomic flux to shrinkage [17], Johnson and co-workers derived a combined-stage sintering model for the entire sintering process, which includes all of the three stages of sintering, i.e., the initial, intermediate and final stage. The fundamental concept of the combined-stage sintering model involves using two separate parameters (geometry M and scale Γ) to characterize the microstructure. Compared with the linear viscoelasticity models [11],[12], the combined-stage model has the potential to simulate the situation with larger density variance. However, it is difficult to determine the parameters in this model, especially the scale parameter. The primary reason is that the physical meaning of the scale parameter is not clear.

Johnson's combined-stage model is described as:

$$-\frac{dL}{Ldt} = \frac{\gamma_s \Omega}{kT}\left(\frac{\Gamma_v D_v}{M^3} + \frac{\Gamma_b \delta D_b}{M^4}\right), \qquad \text{Eq. } \mathbf{2.5}$$

where the left-hand side is the instantaneous linear shrinkage rate, γ_s is the surface energy, Ω is the atomic volume, k is the Boltzmann constant, T is the absolute temperature, M is the mean grain diameter which is a function of relative density, and D_v and D_b are the coefficients of volume and grain boundary diffusion, respectively. $\Gamma(\rho)$ is the lumped scaling parameter, which is related to the driving force, mean diffusion distance, and other geometric features of the microstructure. It should be noted that the parameters in this model all have wide distributions. In particular, the grain size

distribution could vary as much as ±60% from the mean grain size. Accordingly, appropriate averaging schemes are required to determine these parameters.

For most metals, grain boundary diffusion is the dominant mechanism in the sintering process. Thus, only the terms related to the grain boundary diffusion mechanism are considered in this study. Accordingly, by eliminating the terms related to volume diffusion in Equation **2.5**, the following equation is derived,

$$-\frac{dL}{Ldt} = \frac{\gamma\Omega}{kT}\frac{\Gamma_b \delta D_b}{M^4} \ , \qquad \text{Eq. } \mathbf{2.6}$$

where Γ_b is the scaling parameter for grain boundary diffusion dominated process. The definition is

$$\Gamma_b = \frac{\beta C_b C_K}{C_\lambda C_h C_a} \ , \qquad \text{Eq. } \mathbf{2.7}$$

where β is a constant of proportionality relating the chemical potential gradient at the pore surface and the distance over which material is drawn to the pore. The physical meaning of the other scaling factors can be seen in Table **2.1**

Equation **2.7** describes the physical meaning of Γ_b. This equation can be used in any sintering approach. Some of the scaling factors can be estimated empirically from sintering experiments. For instance, C_h can be experimentally obtained through grain growth measurement. However, because the estimations are sensitive to abnormalities in the microstructure arising from wide particle and pore size distributions, grain shape differences and other factors, it is difficult to quantitatively describe all the scaling parameters in Table **2.1**.

Table **2.1**: Physical Meaning of the Scaling Factors

Scaling parameters	Relation with grain size	Equation	Type
C_b	The total grain-boundary-pore intersection length.	$\frac{1}{2}L_b = C_b G$	Grain shape
C_K	The grain-pore interface curvature.	$K = -\frac{C_K}{G}$	Grain shape
C_λ	The mean distance over which material is drawn to the pore.	$\lambda = C_\lambda G$	Grain growth
C_h	The centroid-to-base distance.	$h = C_h G$	Grain growth
C_a	The grain boundary area.	$S^b = C_a G^2$	Grain growth

2.2.3 Olevsky and Co-workers' Model [12]

Olevsky and co-workers developed a phenomenological model of sintering. The model involved the rheological theory of sintering, which was originally built by Skorohod in his book *Rheological Basis of the Theory of Sintering* (1972) published in Russian. The stress-strain rate equation is given by

$$\sigma_{ij} = 2\eta\left(\varphi\dot{\varepsilon}'_{ij} + \psi\dot{\varepsilon}_{ii}\delta_{ij}\right) + P_L\delta_{ij} \qquad \text{Eq. } \mathbf{2.8}$$

where η is the apparent viscosity of the porous body skeleton, P_L is the effective Laplace pressure (sintering stress, σ_s), φ and ψ are the coefficients of the effective shear and bulk moduli, respectively:

$$\varphi = (1-\theta)^2 \qquad \text{Eq. } \mathbf{2.9}$$

and

$$\psi = \frac{2}{3}\frac{(1-\theta)^3}{\theta}, \qquad \text{Eq. } \mathbf{2.10}$$

where the porosity θ is defined as the ratio of the volume of pores V_{pores}, to the total volume V_{total}:

$$\theta = \frac{V_{pores}}{V_{total}}. \qquad \text{Eq. } \mathbf{2.11}$$

Equation **2.8** can also be written as:

$$\sigma_{ij} = p\delta_{ij} + \tilde{q} \qquad \text{Eq. } \mathbf{2.12}$$

where p is the equivalent hydrostatic pressure and $\tilde{q}$ is the Mises equivalent deviatoric stress, defined as

$$p = \frac{1}{3} tr\sigma = 2\eta\psi\dot{\varepsilon}_{ii} + P_L, \qquad \text{Eq. } \mathbf{2.13}$$

and

$$\tilde{q} = \sqrt{\sigma'_{ij}\sigma'_{ij}} = 2\eta\varphi\sqrt{\dot{\varepsilon}'_{ij}\dot{\varepsilon}'_{ij}}, \qquad \text{Eq. } \mathbf{2.14}$$

respectively, where σ'_{ij} is the deviatoric stress tensor.

The derivation of the expression for the effective Laplace pressure based upon the stochastic approach [12] showed that

$$P_L = \sigma_s = \frac{3\gamma_s}{r_0}(1-\theta)^2, \qquad \text{Eq. } \mathbf{2.15}$$

where r_0 is the mean radius of powder particles, and γ_s is the surface tension energy (surface of pores).

2.2.4 Summary of Models

In general, the relation between strain rate and stress can be described as either Equation **2.2** in Riedel's model [11] or Equation **2.8** in Olevsky's model [12]. These two equations are equivalent to each other. Different models can be built in terms of different definitions of the parameters: shear and bulk moduli, sintering stress, etc. For example, the strain rate Equation **2.2** was used in Kwon's study [18] and different sets of parameters were employed for the initial and final stage of densification.

The combined-stage sintering model defined the instantaneous linear shrinkage rate, which has advantages on the qualitative prediction. This particular model might not be applicable to the practical simulation of sintering process due to the inability to measure the range of the parameters; however, the inclusion of physical parameters associated with grain size is desirable and was pursued in the model proposed in this research.

As a conclusion, sintering models such as the creep law [11] and the linear viscoelasticity model [12] are more suitable for our task. These models have fewer parameters. Most of the parameters have clear physical meaning and can be easily empirically determined. Thus the finite element simulation will use this kind of model to describe the material response during sintering.

2.3 Linear Viscoelasticity Theory

The general development and broad application of the linear theory of viscoelasticity has been primarily directed toward applications with polymeric materials.

Unlike those materials accounted for in the theory of elasticity or Newtonian viscous fluid in a nonhydrostatic stress state, materials which are inside the scope of viscoelasticity theory possess a capacity to both store and dissipate mechanical energy. For these materials, a state of stress induces an instantaneous deformation followed by a flow process which may or may not be limited in magnitude as time grows. In general, the external loading could be not only mechanical force or stress, but also thermal induced loading, such as the hydrostatic sintering stress.

Because a viscoelastic material exhibits both an instantaneous elasticity effect and creep characteristics, the material response is not only determined by the current state of stress, but is also determined by all past states of stress. The incremental theory of plasticity also accounts for the history dependent material behavior. However, the underlying difference between the theories of plasticity and viscoelasticity is that the former is independent of the time scale involved in loading and unloading while the latter theory has a specific time or rate dependence.

At the high temperatures associated with sintering, the porous material response shows both elastic and viscous types of behavior. During pressure or pressureless sintering, whether there is a constant or zero mechanical loading, a time-dependent strain will emerge during the long process. This thermal induced strain is called the sintering strain, or viscous strain, or creep strain. It is similar to the traditionally defined creep strain which results from the constant mechanical loading and is both permanent and time-dependent. Therefore, the viscoelasticity theory can be used in the simulation of sintering. The basic structure of the constitutive equations for viscoelasticity theory is briefly described in this section.

2.3.1 Newton's Law of Viscosity

The set of equations that defines viscous flow is similar to that which describes elastic deformation. For example, analogous to the strain-stress relation defined by Hooke's Law, Newton's Law of viscous flow defines the relation between the shear strain rate $\left(\frac{d\gamma}{dt}\right)$ of a viscous material to the applied shear stress τ, i.e.,

$$\frac{d\gamma}{dt} = \mu\tau \ , \qquad \text{Eq. } \mathbf{2.16}$$

or

$$\tau = \eta\frac{d\gamma}{dt} \ , \qquad \text{Eq. } \mathbf{2.17}$$

where μ is termed the fluidity and η the dynamical shear viscosity, or apparent viscosity.

By definition, viscosity is the ratio between stress and strain rate. Therefore, it can be directly measured with a dilatometer test. The axial strain rate can be calculated from the measured axial displacement; the corresponding stress can be calculated from the recorded external loading. Another viscosity measurement method is based on the similarity between the elasticity theory and viscosity theory, i.e., Hooke's Law and Newton's Law of viscous flow. For example, a previous study [19] showed that a 3-point bending experiment can be adapted for a time dependent process and viscosity becomes analogous to the elastic modulus. In both of these methods, however, the calculated stress is not always exactly the actual stress – especially under the complex sintering

conditions. For sintering, the actual stress develops from external loading and the surface tension in the porous material.

2.3.2 Viscoelasticity Models

Various viscoelasticity models have been developed to account for a wide range of deformation behaviors. These models combine elastic and viscous components in various configurations. For instance, the elastic component can be represented by an elastic spring and the viscous component by a dashpot – a pot that contains a viscous liquid that can flow under the action of a piston.

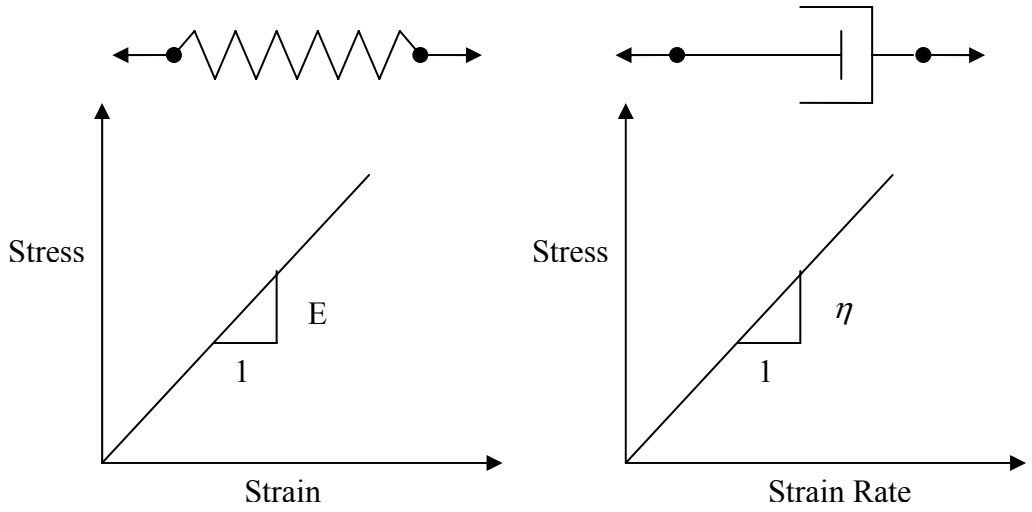

Fig. **2.3**: Spring and Dashpot Components and Their Mechanical Response.

An illustration that shows the deformation behavior of the components can be seen in Figure **2.3** and the equations describing the response are:

$$\sigma = E\varepsilon \text{ and } \sigma = \eta\left(\frac{d\varepsilon}{dt}\right), \qquad \text{Eq. } \mathbf{2.18}$$

where σ is the tensile stress, E is Young's modulus and η is the viscosity.

Different alignment of the components yields different models. For example, the Maxwell model consists of a spring and a dashpot placed in series (Figure **2.4 a**). The overall strain rate is the sum of the contributions from both components. The constitutive equation can be written as

$$\dot{\varepsilon} = \frac{\dot{\sigma}}{E} + \frac{\sigma}{\eta} \; . \qquad \text{Eq. } \mathbf{2.19}$$

On the right hand side of Equation **2.19**, the first part corresponds to the equivalent elastic strain rate, while the second part is the creep strain rate. It is important to note that the equivalent elastic strain rate is a function of stress rate, which might change with time during sintering.

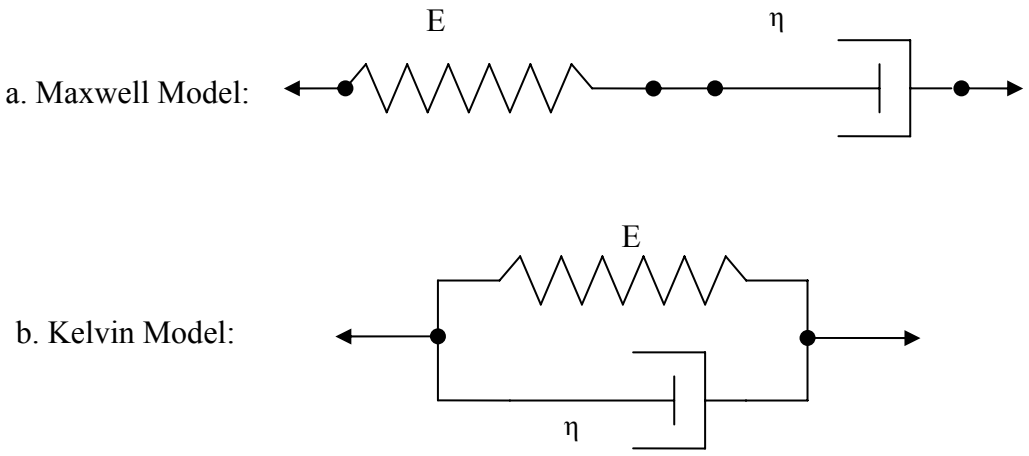

Fig. **2.4**: The Maxwell Model of a Spring and Dashpot in Series and the Kelvin Model of a Spring and Dashpot in Parallel.

An alternative model known as the Voigt or the Kelvin model consists of a spring and a dashpot in parallel (Figure **2.4 b**). For this model, the strains on the two components are always the same and the overall stress is the sum of the stresses on the spring and dashpot. The corresponding constitutive equation is

$$\sigma = E\varepsilon + \eta\dot{\varepsilon} \ . \qquad \text{Eq. } \mathbf{2.20}$$

2.3.3 Constitutive Equations

The constitutive Equation **2.2** in Riedel's model[11] is based on the Equation **2.19** in the Maxwell model, while the constitutive Equation **2.8** in Olevsky's model[12] is corresponding to the Equation **2.20** in the Kelvin model. In this research, a set of viscoelasticity constitutive equations has been developed based on the Maxwell model, which would be more suitable for describing the deformation behavior of metals at high temperature.

For the phenomenological model of sintering, the constitutive equation is selected as a nonlinear viscous incompressible model containing uniformly distributed voids. The strain rate is comprised of the equivalent elastic strain rate $\dot{\boldsymbol{\varepsilon}}^{e}$, thermal strain rate $\dot{\boldsymbol{\varepsilon}}^{t}$, and creep strain rate $\dot{\boldsymbol{\varepsilon}}^{cr}$:

$$\dot{\boldsymbol{\varepsilon}} = \dot{\boldsymbol{\varepsilon}}^{e} + \dot{\boldsymbol{\varepsilon}}^{t} + \dot{\boldsymbol{\varepsilon}}^{cr} . \qquad \text{Eq. } \mathbf{2.21}$$

The portion of elastic strain rate is assumed to be linear and isotropic,

$$\dot{\boldsymbol{\varepsilon}}^{\mathbf{e}} = \dot{\boldsymbol{\sigma}}/\mathbf{C} . \qquad \text{Eq. } \mathbf{2.22}$$

Therefore, Equation **2.22** can be also expressed by the rate form of Hooke's law, i.e.,

$$\dot{\boldsymbol{\sigma}} = \mathbf{C}\dot{\boldsymbol{\varepsilon}}^{e} = \mathbf{C}\left(\dot{\boldsymbol{\varepsilon}} - \dot{\boldsymbol{\varepsilon}}^{t} - \dot{\boldsymbol{\varepsilon}}^{cr}\right). \qquad \text{Eq. } \mathbf{2.23}$$

And the stress can be calculated from the integral of Equation **2.23:**

$$\boldsymbol{\sigma} = \int \dot{\boldsymbol{\sigma}} dt = \int \mathbf{C}\dot{\boldsymbol{\varepsilon}}^{e} dt = \int \mathbf{C}\left(\dot{\boldsymbol{\varepsilon}} - \dot{\boldsymbol{\varepsilon}}^{t} - \dot{\boldsymbol{\varepsilon}}^{cr}\right) dt \ . \qquad \text{Eq. } \mathbf{2.24}$$

Thermal strain is proportional to the change in temperature of the material and is the same in all directions for an isotropic material. It can be calculated by

$$\boldsymbol{\varepsilon}^{t} = \alpha \Delta T \ , \qquad \text{Eq. } \mathbf{2.25}$$

where α is the thermal expansion coefficient, which is usually a function of temperature, ΔT is the difference between the current and reference temperatures.

The creep strain rate consists of two parts: the ratio between the deviatoric stress $\boldsymbol{\sigma}'$ and shear viscosity modulus η_s, and the ratio between the equivalent volumetric stress and bulk viscosity modulus η_b. It obeys a linear viscous law similar to Riedel's model [11] and has the following form,

$$\dot{\boldsymbol{\varepsilon}}^{cr} = \frac{\boldsymbol{\sigma}'}{2\eta_s} + \frac{tr(\boldsymbol{\sigma}) - 3\sigma_s}{9\eta_b}\mathbf{I} \ , \qquad \text{Eq. } \mathbf{2.26}$$

where σ_s is the sintering stress (sintering driving force), $\mathrm{tr}(\boldsymbol{\sigma})$ is the trace of the stress tensor, **I** an identity matrix. The definitions of sintering stress and viscosity moduli are introduced in the next sections.

Figure **2.5** shows a diagram of local stress equilibrium under zero external loading in the sintering model. The sintering stress σ_s is treated as a equivalent hydrostatic pressure and superposed on the stress state to calculate the creep strain rate.

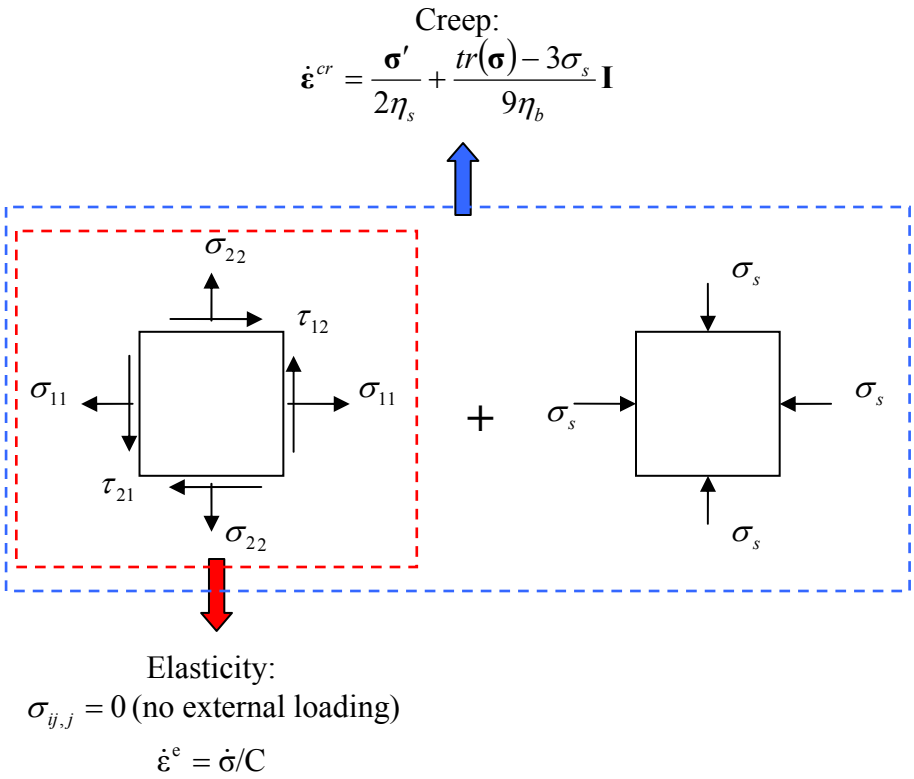

Fig. **2.5**: Diagram of Local Stress Equilibrium under Zero External Loading in Sintering Model.

2.3.4 Viscosity Moduli

Viscosity represents the material resistance to viscous flow. In general, it is temperature-dependent. During sintering, because the temperature has a wide range, the material response is expected to vary. It is reasonable to consider the viscous flow of a thermally activated process and utilize the Arrhenius equation, i.e.,

$$\eta = \eta_0 \exp\left(\frac{Q_v}{RT}\right), \qquad \text{Eq. } \mathbf{2.27}$$

where Q_v is the activation energy for viscous flow, η_0 a pre-exponential material constant, R is the universal gas constant and T is the absolute temperature. It is expected that the Arrhenius temperature relation would be more accurate when the material behaves more like a liquid, e.g., metals at high sintering temperatures.

For porous material, because of the existence of pore area, the parameters in the continuous viscoelasticity theory should be modified before they can be employed. Most of these parameters are functions of porosity. The shear viscosity modulus η_s and bulk viscosity modulus η_b in Equation **2.26** are defined as in Olevsky's model [**20**]:

$$\eta_s = (1-\theta)^2 \eta \ , \qquad \text{Eq. } \mathbf{2.28}$$

and

$$\eta_b = \frac{4}{3}\frac{(1-\theta)^3}{\theta}\eta \ , \qquad \text{Eq. } \mathbf{2.29}$$

where θ is the porosity defined as the ratio of void and bulk volumes, and η is the apparent viscosity as defined in Equation **2.27**.

2.4 Sintering Stress and Transition Temperature

Sintering stress, σ_s, also named sintering driving force, is the equivalent hydrostatic pressure caused by local capillary stresses in porous structures. The resulting stress gradient provides a driving force for mass flow to the neck formed between contacting particles so that the pore area fills with material and the density increases.

2.4.1 Equations of the Sintering Stress

Sintering stress arises from interfacial energies acting over curved surfaces and has been related by several researchers to the surface energy, particle shape, particle size, and/or relative density. For example, Equation **2.30** [3] shows an equation that expresses σ_s associated with the geometric shape of a curved surface.

$$\sigma_s = \gamma_s \left(\frac{1}{R_1} + \frac{1}{R_2} \right), \qquad \text{Eq. } \mathbf{2.30}$$

where γ_s is the surface energy, and R_1 and R_2 are the principal radii of curvature for the surface and represent the particle shape. Other researchers [16] relate sintering stress to relative density via

$$\sigma_s = \sigma_{s1} \left(\frac{1-\rho_1}{1-\rho} \right)^{1/(3m+5)}, \qquad \text{Eq. } \mathbf{2.31}$$

where σ_{s1} is the sintering stress at the reference density, m is a parameter that characterizes the shape of the pore size distribution function and ρ_1 is the reference density. Another sintering stress model is derived from a local equilibrium state under the actions of surface tension, grain boundary diffusion, surface diffusion, and any other major sintering mechanisms. The equilibrium can be expressed as,

$$\sigma_s dV = \gamma_b dA_b + \gamma_s dA_s, \qquad \text{Eq. } \mathbf{2.32}$$

where γ_b is grain boundary diffusion energy, γ_s is the surface tension energy, dV is a virtual volume change, dA_b and dA_s are the associated changes of the grain boundary area and surface area, respectively. Previous studies [3], [21],[22],[23],[24],[25] showed a form of

sintering stress associated directly with interfacial energies, geometric dimensional parameters, and relative density. Specifically, Olevsky and co-workers used a sintering stress in the form of

$$\sigma_s = \frac{3\gamma_s}{\bar{r}}(1-\theta)^2, \qquad \text{Eq. } \mathbf{2.33}$$

where θ the porosity which is defined as the ratio of the volume of pores to the total volume, and $\bar{r}$ denotes the average void size [12] or average particle radius[20].

For most crystalline materials, grain boundary diffusion is one of the dominant mass transport mechanisms in the intermediate stage of solid-state sintering. In this research, because the sintering process of stainless steel 316L is dominated by grain boundary diffusion, the sintering stress relationship deemed most appropriate is one that incorporates surface tension, relative density and average grain size. Specifically the sintering stress is defined by the following function

$$\sigma_s = \frac{6\gamma_s}{G}(1-\theta)^2, \qquad \text{Eq. } \mathbf{2.34}$$

where G is the average grain size representing the influence of grain boundary diffusion.

2.4.2 Sintering Stages and Transition Temperature

Some transient phenomena during sintering are introduced in this section. These phenomena are the reason why a transition temperature for sintering stress has been identified and incorporated into the model.

Sintering begins with weak powder particle compacts and ends with strong nearly full density products. The sintering process for some powder systems, such as

stainless steel 316L, can be divided into three stages: the initial stage with neck growth and minor level of densification, the intermediate stage with grain growth and significant densification, and the final stage with lower densification rate. Due to different dominating mechanisms in these stages, a variety of descriptive models are used to characterize the material behavior. In this research, since axial shrinkage is the major concern, more effort has been focused on the intermediate stage, when significant densification occurs at a faster rate.

It is normally difficult to define the boundary between stages of sintering. However, in some cases, the boundary is quite clear. For instance, according to the dilatometry measurements for stainless steel 316L (see Figure **2.2**), nickel and bronze (see Figure **2.6**), the boundary between the initial and intermediate stages can be easily found by the trend of the axial shrinkage curves: the initial stage has negative gradient and the intermediate stage has positive one. In this research, the boundary is defined as a transition point and the corresponding sintering temperature is defined as transition temperature, T_t, above which the shrinkage rate will increase dramatically.

Since the kinetics of sintering densification are so slow that they can be omitted in the initial stage, an assumption is made that the sintering stress is zero until T_t is reached. This assumption is consistent with observations from other experimental studies [**26**],[**27**],[**28**]. Also, zero sinter stress happens during cooling. From the dilatometry data (see Figure **2.2**) of shrinkage rate versus temperature, one can determine that the transition temperature for stainless steel 316L compacts ranges from 900°C to 1000°C. The smaller the particle size, the lower the transition temperature.

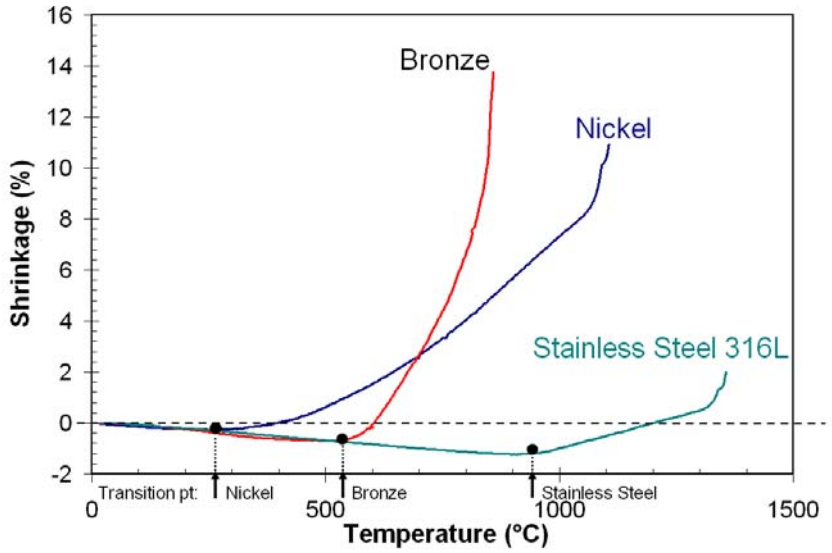

Fig. **2.6**: Transition Points for Nickel, Bronze and Stainless Steel 316L during Sintering

2.5 Thermal Effects

For porous materials that endure a relatively small amount of densification during solid state sintering, the thermal deformation should not be ignored. For instance, the total shrinkage for a stainless steel 316L green compact with relative density around 75% is only 3% to 5%. Accurate simulations of the entire sintering process require the consideration of not only the creep strain but also the thermal strain.

For solid state sintering of most metals and alloys, because there is no major chemical reaction occurring during sintering, it is reasonable to assume that no extra heat source is considered to be generated during the process. Therefore, the heat transfer process can be deemed as an independent process to the sintering process.

2.5.1 The Recipe: Sintering Cycle

The sintering cycle is the set-up of thermal conditions specifically for densifying powder metal compacts. Generally, the optimal cycle is material and application dependent. A complex set of factors needs to be considered for the determination of an appropriate sintering cycle. These factors include heating rate, maximum temperature, hold time, and atmosphere. Basically, one can select a suitable cycle from any available experimental database, such as that listed in [**3**].

The sintering cycle selected for stainless steel 316L is shown in Figure **2.7**. It begins with heating in pure hydrogen at a rate of 10°C/min to a maximum temperature of 1350°C. After a 1 hour hold, the part is cooled at 10°C/min. However, the actual sintering cycle might differ a little bit from the designed one due to the capability of the furnace. Especially, the cooling rate might not be as expected. If the densification is near complete after the hold, slight variation in the cooling should not have a significant influence on the final shrinkage. A comparison of the prescribed sintering cycle and an actual one can be seen in Figure **2.7**.

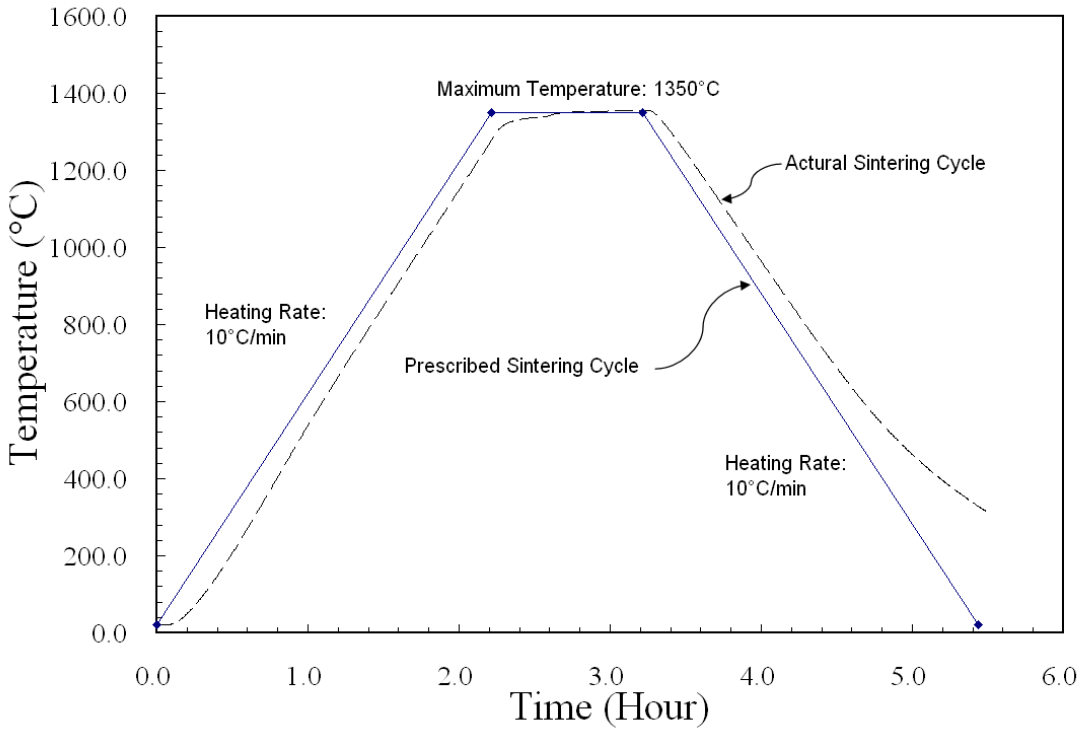

Fig. **2.7**: Comparison of the Prescribed & Actual Sintering Cycle for Stainless Steel 316L

2.5.2 Thermal Expansion Coefficient

For materials with relatively small sintering shrinkage, the thermal expansion may dominate some portion of the sintering process. Based on the assumption that prior to the transition temperature a negligible amount of sintering creep occurs making the thermal expansion the major deformation mechanism in this initial period. For stainless steel 316L, this period ranges from room temperature up to around 900°C. Within this range, previous research [29] has shown that for continuous material the coefficient of thermal expansion (CTE), α , monotonically increases as temperature increases. For porous

material, it has been shown [30] that TEC can be treated as a function of relative density within a narrow range of temperature, i.e., from room temperature to 200°C. The curve fitting empirical equation follows a power law. However, in this research, it has been found through dilatometer tests that TEC is a function of temperature. Although the relation is more complex than using the linear law at some local portions, the overall relation is close to linear for the temperature from room temperature to 900°C. The measurement of the TEC is discussed in detail in Chapter 4.

2.6 Summary

A model to capture the shrinkage of stainless steel 316L compacts during sintering has been developed to incorporate thermal expansion during the initial stage and shrinkage due to the grain boundary diffusion which dominates the intermediate stage of sintering. Based on a review of several previous sintering models, a linear viscoelasticity model has been selected for the simulation of the thermally induced creep behavior of stainless steel 316L powder compacts. The viscosity moduli are assumed to be functions of relative density and apparent viscosity, and the sintering stress has been deemed as an equivalent hydrostatic pressure in the calculation of creep strain rate. In the sintering stress equation, σ_s is proportional to the reciprocal of grain size. It is this relation that builds a link between the microstructure evolution and macroscale deformation. Compared with other sintering models, this model has the following advantages:

1. It is a simple and practical model that all of the parameters have clear physical meaning and can be experimentally determined with fairly simple tests.
2. This continuum mechanics based sintering model links characteristics on the microscale level with the macroscale deformation, which provides additional insight into the sintering process.
3. It can be directly employed in the finite element analysis and has a wide range of applications with the aid of computers and commercial FEM/CAD/CAM software.

To obtain the material parameters, measurements of grain size and experimental studies on the sintering stress have been performed. Details will be presented in the next two chapters.

Chapter 3

Grain Growth Measurement and Simulation

In grain boundary diffusion dominated sintering processes, the sintering stress is proportional to the reciprocal of grain size, as showed in Equation **2.34**. It is this relation that links the macro-scale deformation with the microstructure evolution of the material. Therefore, it is one of the major tasks in this research to perform accurate measurements of grain growth during sintering. In this chapter, a metallographic method that fits the ASTM standard E112-96 is employed to measure the grain size in a porous body; a statistical concept, arithmetic mean, is used to represent the log-normal distribution grain size data; and a numerical model is shown that fits the grain growth curve accurately.

3.1 Grain Boundary Diffusion in Sintering

Grain boundary diffusion is a mass flow mechanism used to describe the solid-state sintering of many materials during their densification [3]. These materials include various ferrous alloy systems, Ni, Fe, Cu, etc. Grain boundaries form in the interface between crystals with different atomic orientations. Basically, grain boundary diffusion consists of lattice defects between grains. Corresponding to large and small rotation angles between adjacent grains, the misorientation could be random and repeated, respectively. Therefore, a grain boundary is as narrow as a crystallite, usually in the scale of nanometer. However, it is still an efficient mass flow path.

During sintering, mass is removed along the grain boundary and flows into the sinter bond. In contrast, vacancies move along the opposite direction. Thus, as sintering progresses, transport between pores via grain boundary leads to pore coarsening. This phenomenon has been observed in this research and reported in the latter sections in this chapter. Resistance for grain boundary diffusion comes from growing grains and gaps between powder particles. The larger the grain grows, the slower the diffusion. As a result, the grain boundary diffusion mechanism is only dominant in the intermediate stage of sintering.

The influence of grain boundary diffusion on sintering depends on several factors: the grain shape, the grain size, and the distribution. To simplify the analysis, it is reasonable to use average behavior representing these factors. In this research, the grain size distribution is measured and an average value is used to represent the overall behavior.

3.2 Grain Growth Mechanism

Grain growth is the process that the average grain size of an aggregate of crystals increases. It is driven by the decrease in surface energy and reduction in the total grain boundary area. Grain growth is closely related to the migration of the grain boundary. For continuous materials, depending on the microstructure character and growth pattern, two different types of grain growth have been reported in previous studies [31],[32],[33]: abnormal grain growth (AGG) and normal grain growth. AGG occurs at temperatures below $0.7T_m$ to $0.9T_m$, where T_m is the melting point. When AGG occurs, most of the

grain boundaries are found to have faceted structures. Additionally, quite a few grains grow rapidly while most of the grains grow slowly. Therefore, the average of the grain size distribution is not changing significantly. When normal grain growth occurs, faceted grain boundaries are replaced with smoothly curved shapes and the grain growth speed increases dramatically despite the initial grain size. The overall grain size distribution can be described by a log-normal distribution.

If the activation energy for grain growth is high, grain growth may not be very fast and neither is the sintering densification. It has been reported in [**34**] that, as the temperature gets to a transition point, the activation energy may shift to a different level, which causes an immediate increase of grain size. As the grain grows bigger, the growth rate becomes slower. Ultimately, the resistance and the driving force may reach a balance point. According to these observations, it is reasonable to conclude that a transition temperature exists for grain growth of continuous material. This transition temperature defines the boundary between AGG and normal grain growth, and also the shift between the two activation energy levels.

Considering the fact that even the smallest pore in a powder compact is much larger than the width of a grain boundary or the size of a dislocation, which is around several nanometers, it is reasonable to believe that the grain growth behavior in a porous body is the same as it is in a full-dense body. Therefore, previous results from the study of grain growth behavior in a continuous material can be used in this research as well. However, the method of grain size measurement should be modified to include the effect of the existence of voids in porous materials. Furthermore some phenomena such as

extremely large grains in AGG might not be obvious in a powder compact due to the resistance of rapid grain growth from the initial gaps between powder particles.

For the stainless steel 316L powder compacts in this research, it has been observed that faceted structures exist below around 1200°C, and facets are reduced when temperature is higher than 1200°C. The grain growth rate is much higher after the temperature is higher than 1200°C. Thus, the transition temperature is 1200°C.

3.3 Grain Size Measurement for Porous Material

Research on grain size measurement has been of interest for more than a century since people realized the relation between mechanical properties and grain size. A number of factors make grain size measurement complicated. Most techniques rely on cutting through the sample to view a sectioned plane. The grain size obtained from a sectioned plane may not represent the three-dimensional size of the grains; however if the number of total measured grains in sectioning planes is representative of the structure, as proven in a previous study [40], the two-dimensional representation may be sufficient. Also, grain shape and type of grains may vary and affect the measurement of grain size throughout the sample. Depending on the interest, several basic concepts are needed for representing the complicated results.

Different measures of grain size complicate the measurement. The planimetric method uses the number of grains per unit area to calculate the average grain size; the intercept method yields a mean intercept length which can be related to average grain size in different ways; other planar grain size distribution methods have also used the number

of grains per unit volume to calculate grain size. It was not until the 1974 revision of ASTM E112-96 that the intercept procedure became the preferred analysis technique. It is proven to be the most efficient method and most precise estimate of the grain size. In addition, recent studies [41],[42] show a new method by using serial sections to reconstruct three-dimensional microstructure volume to estimate the three-dimensional grain size distribution. While promising, this new three-dimensional reconstruction technique is still not practical, so the intercept counting method is preferred.

The difference between the grain size measurement in porous material and continuous material is the existence of voids. For example, in the intercept procedure, there are only 2 elements in a continuous material micrograph: grain and boundary, while there is one more element in a porous material micrograph: pore. In this research, a metallographic method based on the Abrams three-circle intercept procedure [43] has been developed. It is able to distinguish all three elements, grain, pore and boundary, in a micrograph and therefore provide accurate results for grain size measurement for porous material.

3.3.1 Design of the Test Method

It is expected that the grain size during sintering is affected by initial powder particle size, green density and density gradient. Thus, this test method is designed to study the influence of these factors. During the pressing of powder during compaction, deformation may introduce initial grain size variation; therefore, in order to reduce the effect of density gradients, cold isostatic pressing (CIP) stainless steel powder compacts

were used. Three different particle size powders were used in CIP to study the influence of particle size on grain growth, as shown in Table **3.1**. For each batch of particle size powders, samples were compacted to two levels of green densities (75% and 79%).

Table **3.1**: Powder Characterization of Water-atomized Stainless Steel 316L as Affected by Powder Particle Size

Powder[1]	Mean size (μm)	D_{10} (μm)	D_{50} (μm)	D_{90} (μm)	Apparent Density (g/cm^3)	Tap Density (g/cm^3)	Pycnometer Density (g/cm^3)
SS316L-Large	72.5	38.4	67.5	111	2.22	3.41	7.85
SS316L-Medium	52.5	29.5	48.8	79.6	2.36	3.66	7.85
SS316L-Small	33.4	17.3	30.4	52.0	2.41	3.87	7.91

In summary, there are in total 6 groups of specimens. Each is given a name for future citing use, as shown in Table **3.2**. The prescribed sintering cycle for this method is to heat at 10°C/min to 1350°C. Hold the temperature at 1350°C for 1 hour and then cool to room temperature. Because this study involves measuring grain growth during the sintering cycle, the specimen will be quenched at various stages along the sintering cycle (see Figure **3.1**).

Sintered samples were then mounted in fluorescence epoxy. The reason to use fluorescence epoxy rather than regular epoxy is to reduce the error induced by material pull out from the next step [44]. Mounted samples were ground and polished to obtain flat and smooth surfaces for optical microscopic study. Because porous material has weak particle bonding, different procedures were necessary for different levels of relative density. The lower the density, the less aggressive the procedure should be.

---

[1] Supplied by Hoeganeas Inc.

Table **3.2**: Summary of the Samples for Grain Growth Measurement

Group Name	S75	S79	M75	M79	L75	L79
Mean Particle Size (μm)	33.4	33.4	52.5	52.5	72.5	72.5
Green Density Level (%)	75	79	75	79	75	79

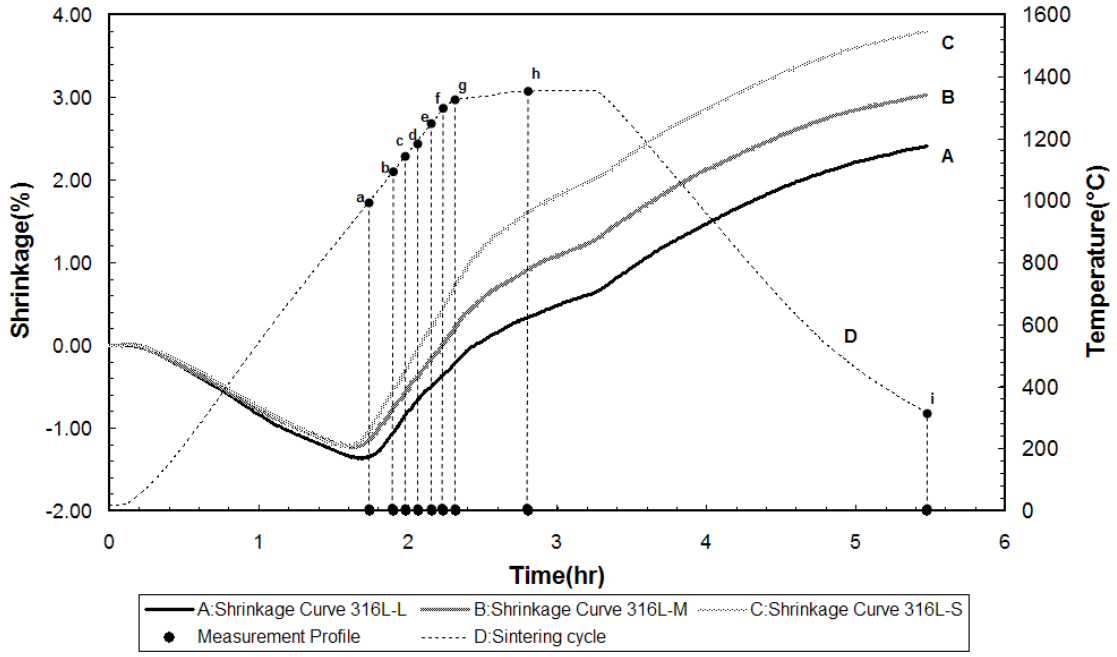

Fig. **3.1**: Arrangement of the Measurement Profile along A Sintering Cycle (Measure Points Shown from a to i)

It can be observed under the optical microscope that the polished surface consists of grain and pore area. In order to reveal the grain boundary within the grain area, a chemical etching method was used. For austenitic alloys such as stainless steel 316L, it is very difficult to etch completely so that all the grain boundaries are visible [45]. Furthermore, if the austenitic alloy contains annealing twins the grain size measurements are adversely affected as the twin boundaries must be ignored when rating grain size. These difficulties make it hard to measure the grain size with a high degree of precision.

Several techniques have been employed in the following image analysis procedure to reduce the effects of annealed twins and provide more precise results.

Metallographic images with grain structure were analyzed by the Abrams three-circle intercept procedure [43]. Specific adaptations for this research include: the boundary between pore and grain area was treated as a grain boundary; intercepts located within grain area were counted as grain intercepts; and intercepts located within the pore area were counted as pore intercepts. The collection of grain intercepts yields a grain size distribution, while a collection of pore intercepts yields a pore size distribution. This procedure is completed semi-automatically: manual determination of intersections by visual inspection and counting by a computer program. The outcome of the digital image analysis is a distribution of grain size. According to the shape of the distribution histogram, one of the statistical concepts is chosen to efficiently represent the average grain size. Details are presented in the later sections of this chapter.

As a summary, a flow chart describing the method for grain size measurement of porous material is listed in Figure **3.2**.

3.3.2 Preparation of Metallographic Specimens

The three groups of powders shown in Table **3.1** were sieved, mixed and blended from the same raw powder resource supplied by Höganäs Inc. Figure **3.3** shows the shape and size for different groups of stainless steel 316L powders under the Scanning Electron Microscope (SEM). Although these are water-atomized powders, some rounded shapes

can also be seen. This is the reason why the compression for these powders is very difficult.

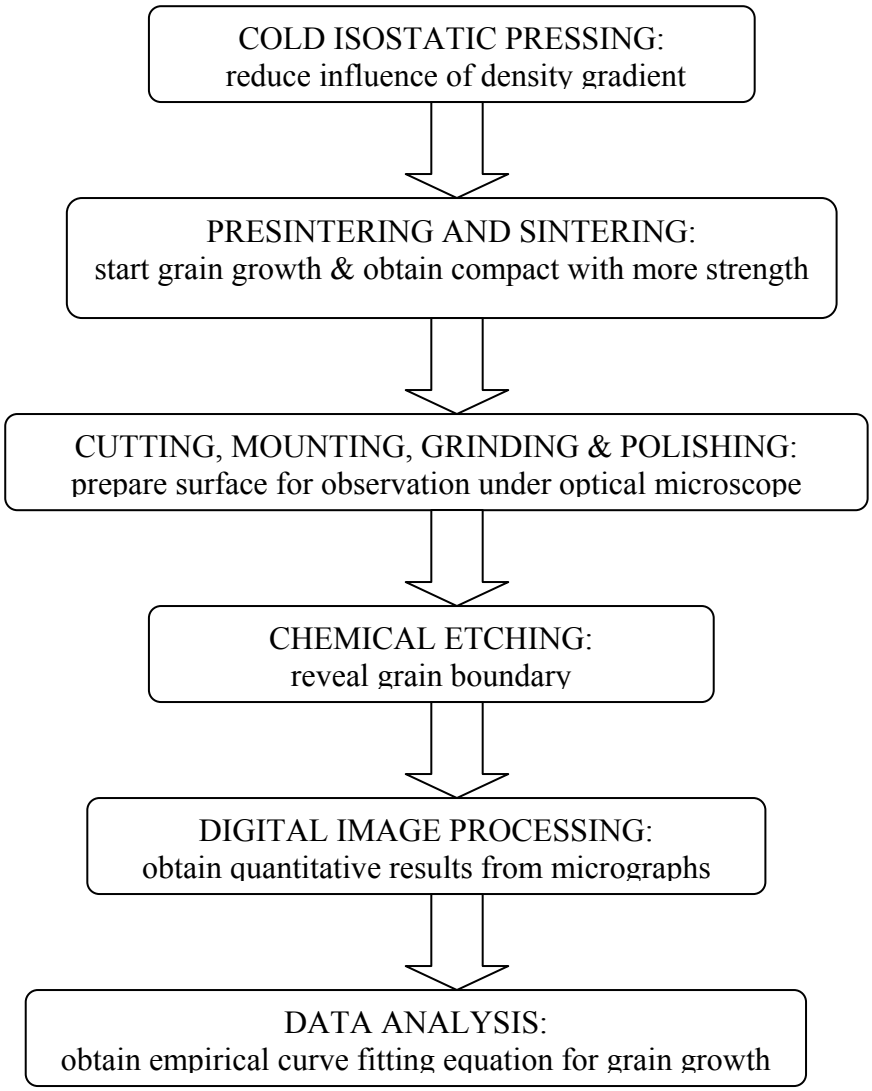

Fig. **3.2**: Flow Chart of the Test Method for Grain Size Measurement of Porous Material

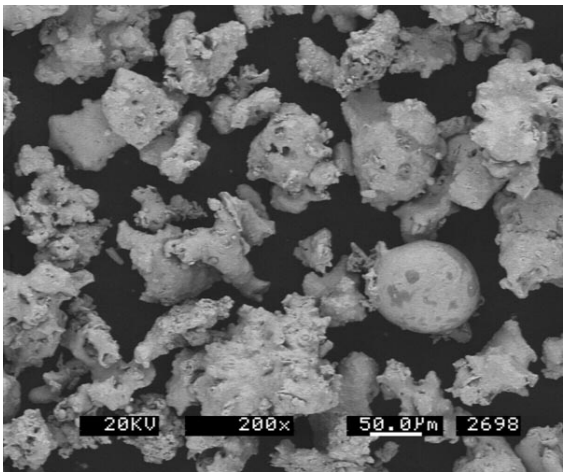

(a) 316L large size powder (200×)

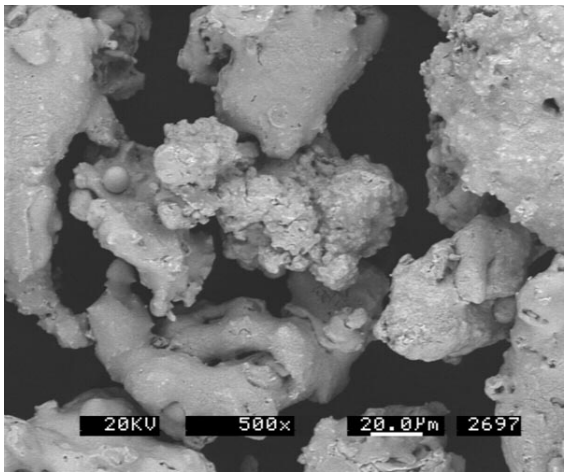

(b) 316L large size powder (500×)

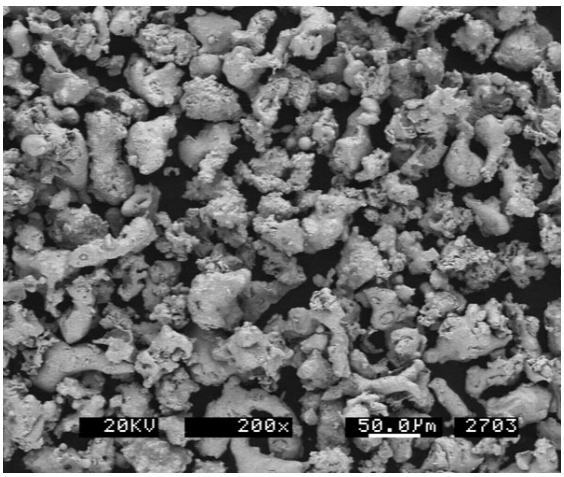

(c) 316L medium size powder (200×)

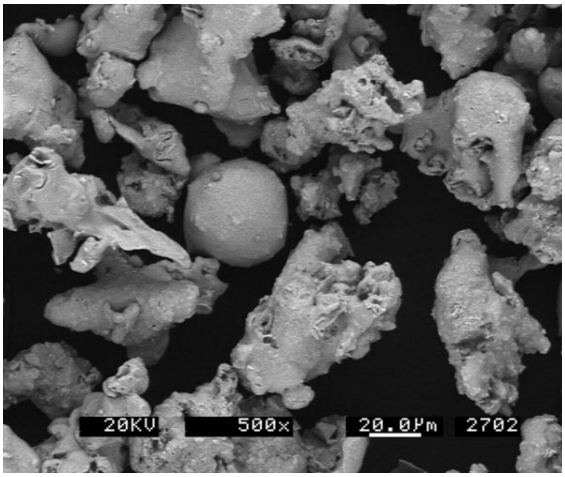

(d) 316L medium size powder (500×)

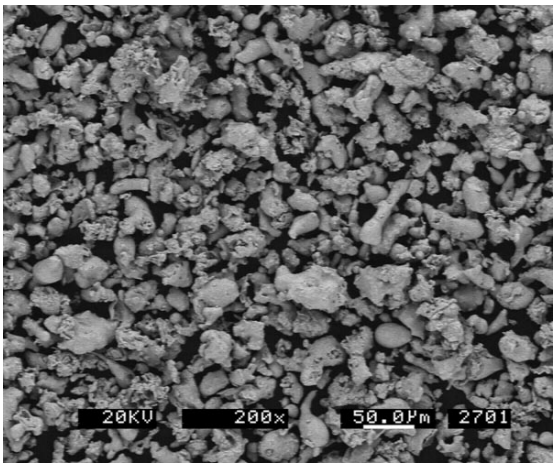

(e) 316L small size powder (200×)

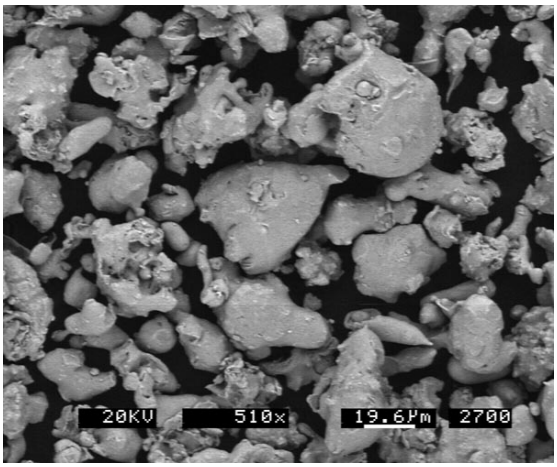

(f) 316L small size powder (500×)

Fig. **3.3**: SEMs of Water Atomized Stainless Steel 316L Powders

CIP is a powder compaction technique to obtain a compact with uniformly distributed density at room temperature. Basically, it uses a flexible mold, usually made of rubber, under a high hydrostatic pressure in a hydraulic pressure chamber. The diameter of the cylindrical CIP samples is approximately 25 mm. Two density levels were set up to test the effect of green density on grain growth: 75% relative density and 79% relative density.

The cylindrical CIP compacts were presintered before they were strong enough to be cut into half cylinders using the rotary saw with diamond blades. The cutting speed was set to 8 m/s and the weight bar was ¾ of the way back. After being cut, the samples were put into a vertical quench furnace for sintering to the preset temperature and quenched in cold water to freeze the grain structure. Sintered samples were then hand ground until their surfaces were smooth. All samples were mounted in a 1.5-inch LECO mounting cup using an epoxy mixture made of 25 parts by weight Struers Epofix resin and 3 parts by weight Struers Epofix hardener. To impregnate the sample, a vacuum of 80 kPa was applied for a total of 8 minutes. After impregnation, the samples were cured in air at room temperature for 24 hours. The samples were plane-ground on a LECO VP-50 hand grinder. They were then polished using a Struers RotoForce-4 sample mover attached to a Struers RotoPol-22 automatic polisher. The grinding and polishing conditions are listed in Table **3.3**.

A chemical etching method was used on the polished samples to reveal the grain boundaries. To overcome the etching difficulty for stainless steel 316L mentioned in [**45**], various etchants recommended in [**45**], [**46**] and [**47**] were tried: Fry, Marble, Kalling and Methanolic Aqua Regia (MAR, HCl:HNO_3:Methanol, 9:3:4). These etchants all tended to

burn before bringing out the boundaries clearly, except for MAR. Therefore, MAR was chosen to perform the etching, though it was not always effective on every sample.

Table **3.3**: Grinding and Polishing Conditions

Condition	Grinding	Polishing[2]		
		Fine[3]	Fine	Final
Material	500 grits Silicon Carbide	9 μm diamond	3 μm diamond	OP-A/OP-S
Pressure	Hand grinding[4]	30 N	30 N	15 N
Time	Hand grinding	5 min	4 min	1 min 20 sec[5]
Cloth	Silica-carbide	MD-PLAN	MD-MOL	MD-CHEM
Lubricant	water	blue liquid	water	water

At the beginning of the etching process, a few drops of MAR were applied on the entire sample surface with a pipette. Then the sample was tapped to get bubbles off the sample surface and held for one minute. For repolished samples and samples sintered at high temperature, a little less etching time is needed. It is important to know that MAR must be used right after being made because it may lose its effectiveness in a few hours. Its yellow/orange color is a good indicator of whether it is still effective. These chemical etchants need to be handled extremely carefully and the waste needs to be diluted (10:1) and put in a waste storage area.

---

[2] Each polishing step was followed by 5 minutes of ultrasonic cleaning.
[3] This step was repeated three times.
[4] Hand ground until the surface was flat and without defects.
[5] Longer final polishing time up to 2 min 10 sec is suggested to remove old etchant.

3.3.3 The Micrograph of Grain Structure

The hardware used in this research to obtain optical micrographs of grain structures includes a Nikon Epiphot 300 optical microscope and a Polaroid Digital Camera Model PDMC-2 linking to a PC. The CLEMEX Vision PE^{TM} 3.5 system was installed on the PC for image analysis.

Three different scales were used: 200×, 500×, and 1000×. The larger scale was used for samples sintered at temperatures below the transition point (1200°C). The smaller scale was used for fully sintered samples. However, it was also found that the 500× scale covered the grain size range of all the samples.

Digital images were stored in computer hard drive in TIF format for further analysis. Each image contained a three dimension matrix of 1280×1024×256. The first two numbers represent the resolution (in pixels) of the image, while the last number refers to the gray intensity (range from 0 to 255) at the position defined by the first two coordinates. An example of the micrograph can be seen in Figure **3.4**. Three elements (grain, pore and grain boundary) are shown in the micrograph.

3.3.4 Challenges in Digital Image Analysis

The purpose of the digital image analysis is to obtain quantitative results of grain growth from the micrographs of the grain structure. Basically, there are six major challenges need to be faced to accomplish this task.

First of all, the total number of micrographs taken in this research for those six groups listed in Table **3.2** is more than 300. Because the amount of analysis work is

substantial, manual measurement is impossible and it must be done with the aid of a computer program. However, some essential parts of the work, such as highlighting the location of grain boundary, are sufficiently complex that they must be done by a person.

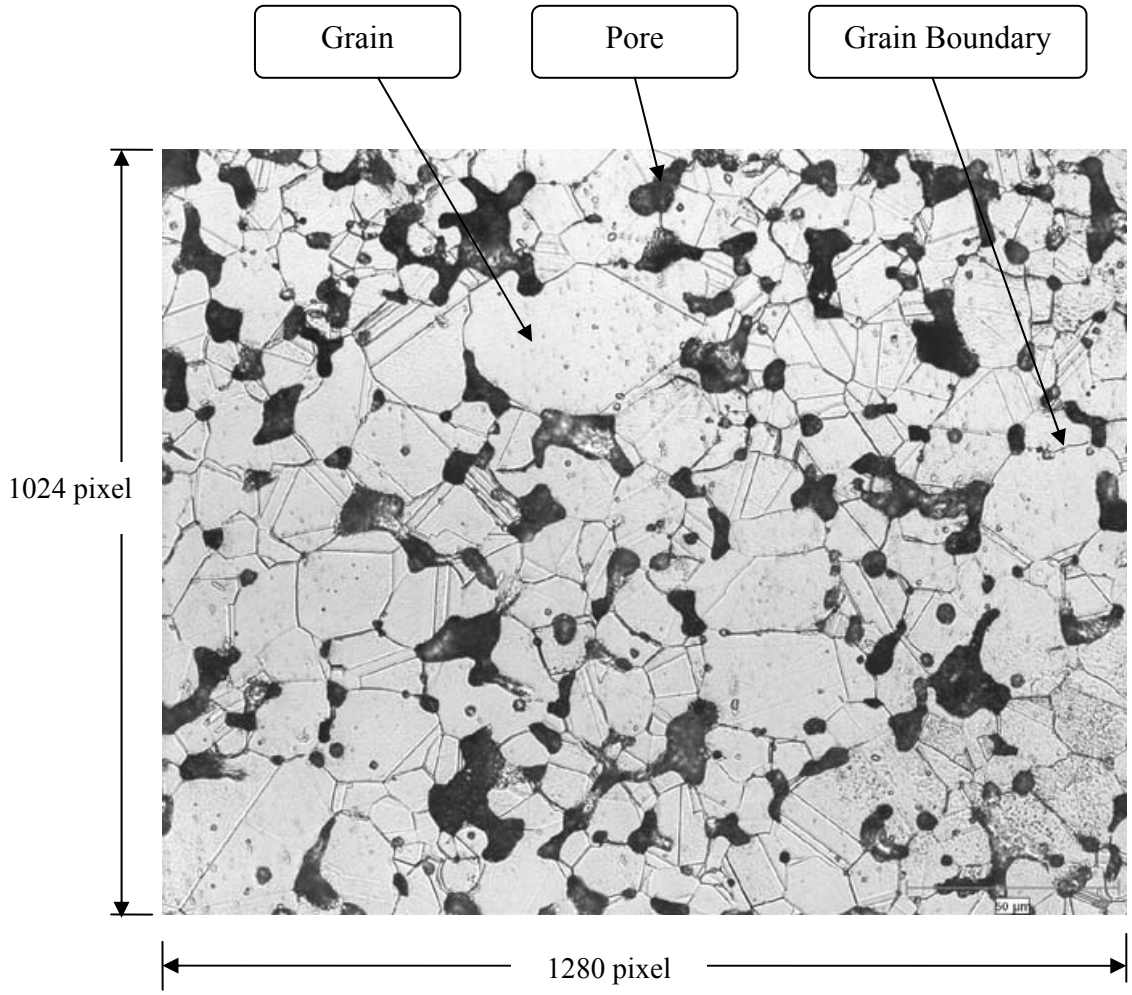

Fig. **3.4**: Grain Microstructure of Stainless Steel 316L, at 500×, Sintered at 1350°C. (S79: Mean Particle Size Value 33.4μm, Die-compacted to 79% Relative Density, Chemical Etched with MAR)

Poor quality images with different kinds of defects also present challenges for automatically counting the grain size. Figure **3.5** shows typical defects such as a scratch,

a burn, and chemical residue. These defects can be reduced to a fairly low level with the previous polishing and etching procedures but are impossible to completely avoid. As a result, commercial metallographic systems such as CLEMEX or LECO may not be suitable to identify and account for them appropriately. Human judgment on distinguishing grain structure characters from defects is necessary.

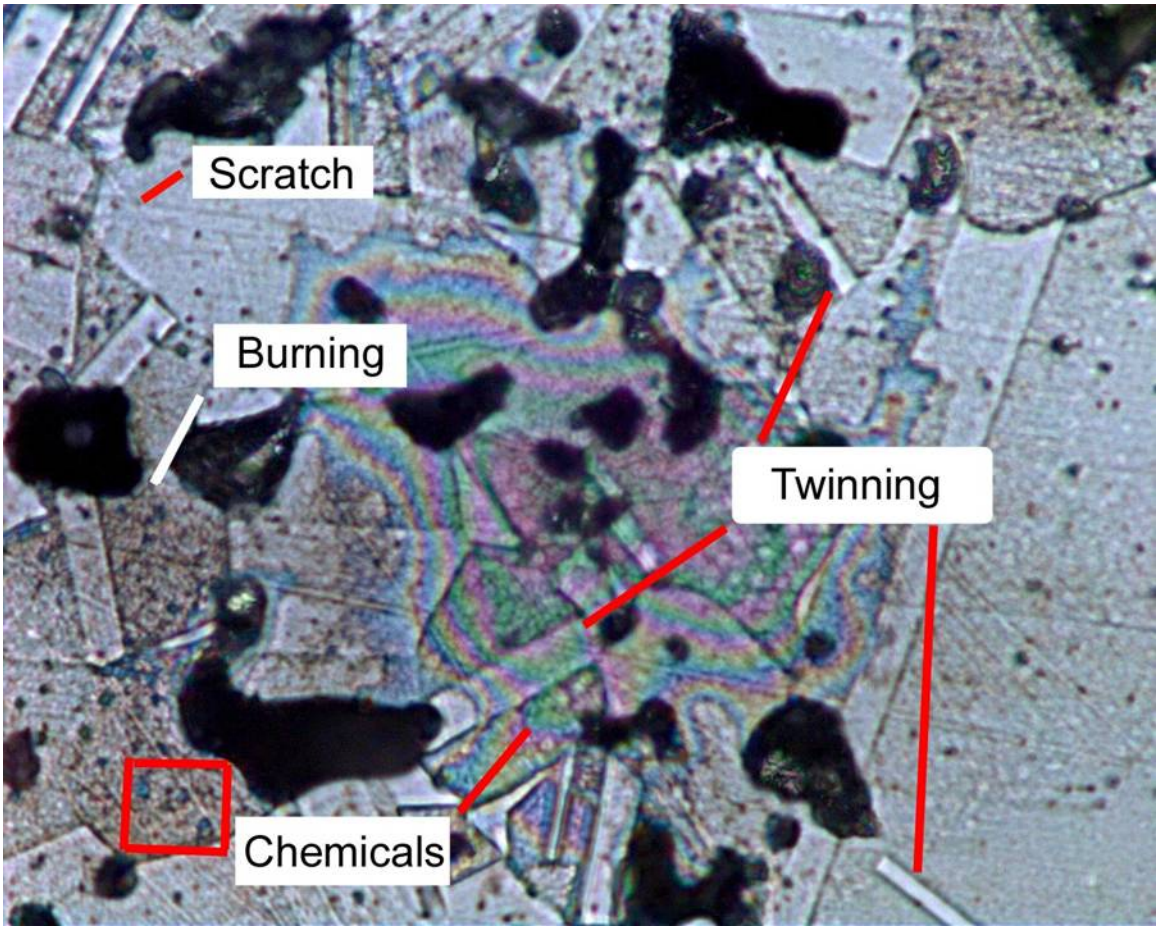

Fig. **3.5**: Typical Defects and Twins in a Poor Quality Micrograph

When etched with MAR, twin boundaries were also revealed (see Figure **3.5**). They must be ignored when rating grain size. These boundaries have similar gray intensity level as grain boundaries. Therefore it is difficult for a digital analysis program

to tell the difference between these two types of boundaries. However, because of the facet shape of twin structure, it is relatively easy for a human to distinguish the twin boundary from a grain boundary. As a result, highlighting the locations of grain boundary was finished manually.

Dendrites are formed in metal powders that are manufactured with an atomization technique (see Figure 3.6 **a**). During heating the tree-shape dendritic microstructure recrystallizes into grains and the dendrites pinch off. This transformation is usually slow, so it happens during early sintering. In this research, dendritic microstructures were observed in a few micrographs from early sintering (see Figure 3.6 **b**). These dendrites may cause confusion when finding the grain boundaries. It is assumed that the dendrites formed in one grain will not generate new grain boundary within the same area.

For grain size measurements of porous material, the existence of pores should not be ignored. ASTM E112-96 is applicable for continuous materials only. There are no rules concerning how to deal with the pore area in a section plane. Therefore, modification and adjustment on these methods are necessary before they can be applied to porous materials.

As a summary, a new test method needs to be devised and applied for grain size measurement for porous material. This method should be able to efficiently distinguish grain boundaries from all kinds of defects and anomalies.

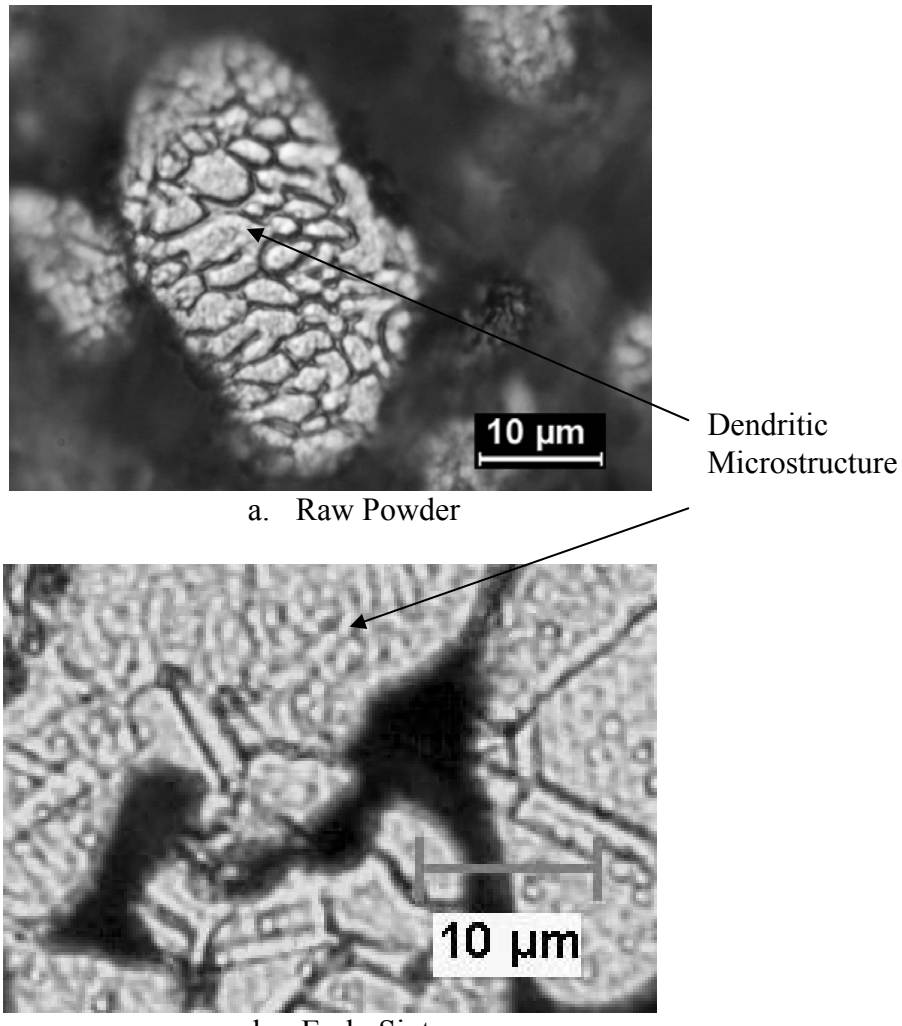

a. Raw Powder

b. Early Sinter

Fig. **3.6**: Dendritic Structure in Gas-Atomized Stainless Steel Powder and Sample in Early Sintering when Temperature Reaches 1200°C. (M79: Particle Size Mean Value 52.5µm, Die-compacted to 79% Relative Density)

3.3.5 Procedure of Metallographic Analysis for Porous Material

Considering the complexity of image analysis of the metallographic microscopies for porous material, a semi-automatic procedure was developed for this research. The technique used the same process presented in the Abrams three-circle intercept

procedure. Human judgment was used only on the determination of the intercept location and the rest of the work such as counting and postprocessing was handled by computer. As was mentioned in **3.3.1**, this procedure is able to count not only the grain size but also the pore size in the micrograph. Details of the procedure are shown below.

3.3.5.1 Step 1: Test Pattern Generation

In MATLAB (see Appendix A.1), a test pattern (see Figure **3.7**) of 3 concentric circles was generated such that the ratio of diameters was 3:2:1. All the coordinates of the points on the circles were sent to an output file along with a 1280×1024 pixel pattern image.

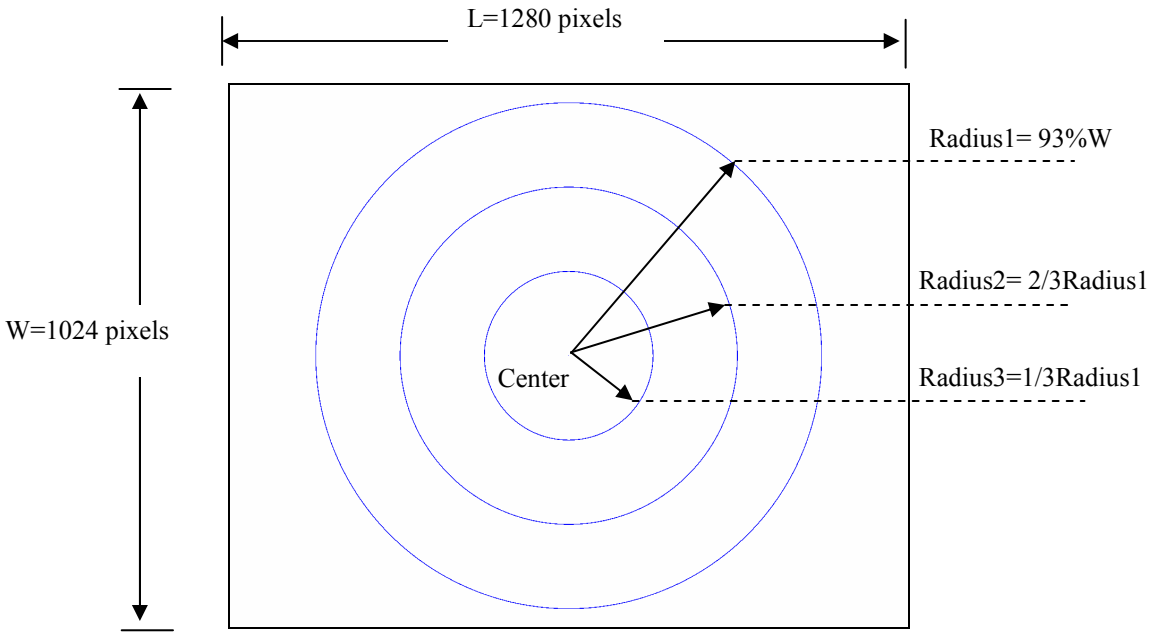

Fig. **3.7**: Illustration of Intercept Counting – Test Pattern for Intercept Counting

3.3.5.2 Step 2: Intercept Marking

In Photoshop, the pixeled image was added as a new layer above the metallographic image. Note that both the pattern and the micrograph image have the same size. By using the eraser tools with the size of 3 pixels, the circle intercepts located in the pore area and on the grain boundaries can be erased, thus breaking the circles into arc segments (see Figure **3.8**). Experience with metallography theory and practice is advantageous with this step to reduce the human error. The modified segmented circles were saved for digital image analysis.

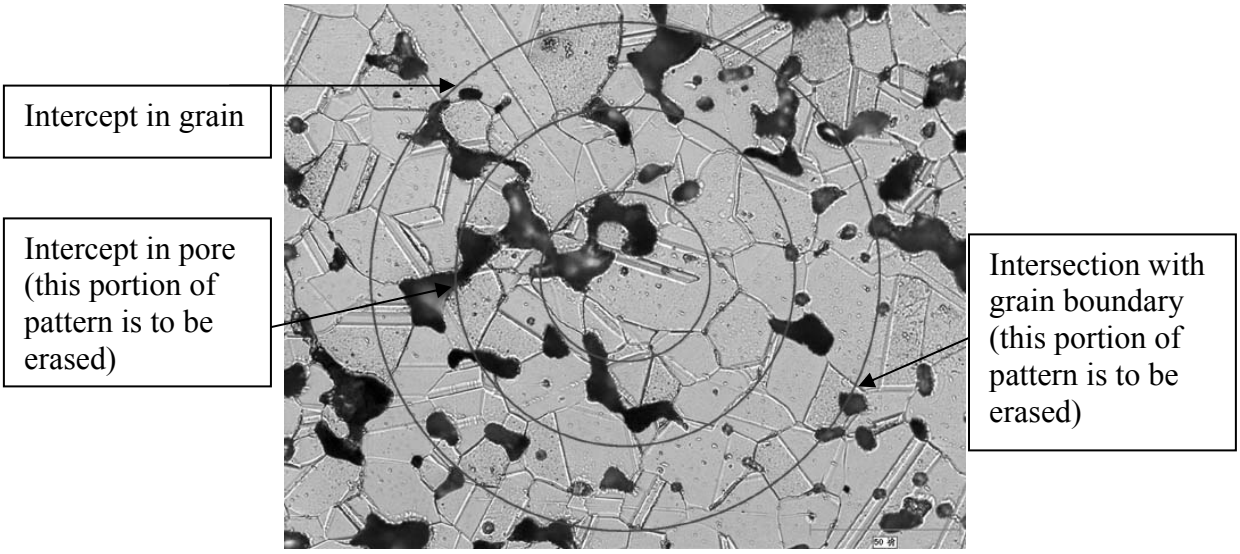

Fig. **3.8**: Illustration of Intercept Counting – Metallograph with Test Pattern (Stainless Steel 316L Sintered at 1350°C with 1-hour Holding, Sample Group M79: Particle Size Mean Value 52.5μm, Die-compacted to 79% Relative Density)

Note that any character smaller than 3 pixels, the size of the eraser brush, will be ignored. The reason to use the 3-pixel eraser is because it is the smallest one that can be comfortably detected by humans and still provide accurate results. For most metals, as

reported in a previous study [48] a grain boundary is approximately 3 atomic diameters wide. That is, the width of a grain boundary is usually on a nanometer scale, which is trivial compared with the length corresponding to a 3-pixel segment in a micrograph, which usually ranges from a quarter of a micrometer to one micrometer. Therefore, the actual length of the eraser should be added to the intercept length and an extra modification step was introduced to account for that length (see section **3.3.5.4**).

3.3.5.3 Step 3: Intercept Counting

An example of the modified pattern image is shown in Figure **3.9**. It consists of the remaining arc segments of the original 3 concentric circles. Different from the mechanism used in most of the commercial image analysis software, the intercept counting procedure in this research is dealing with the test pattern only, not the original micrograph. It has an obvious advantage by simplifying the problem because there are only 2 gray intensity levels (0 and 1) in a pattern image, while there are 256 levels in a micrograph.

The counting of the intercepts was done in an application code programmed in MATLAB (**Appendix A**). Two step filters, 0 to 1 and 1 to 0, were applied along all the concentric circles to determine the start and end of every intercept. An illustration can be seen in Figure **3.10**. Any gap wider than an eraser width was deemed as a pore intercept. The result of the length of each intercept in a pattern image was stored in a data file for analysis in the next step.

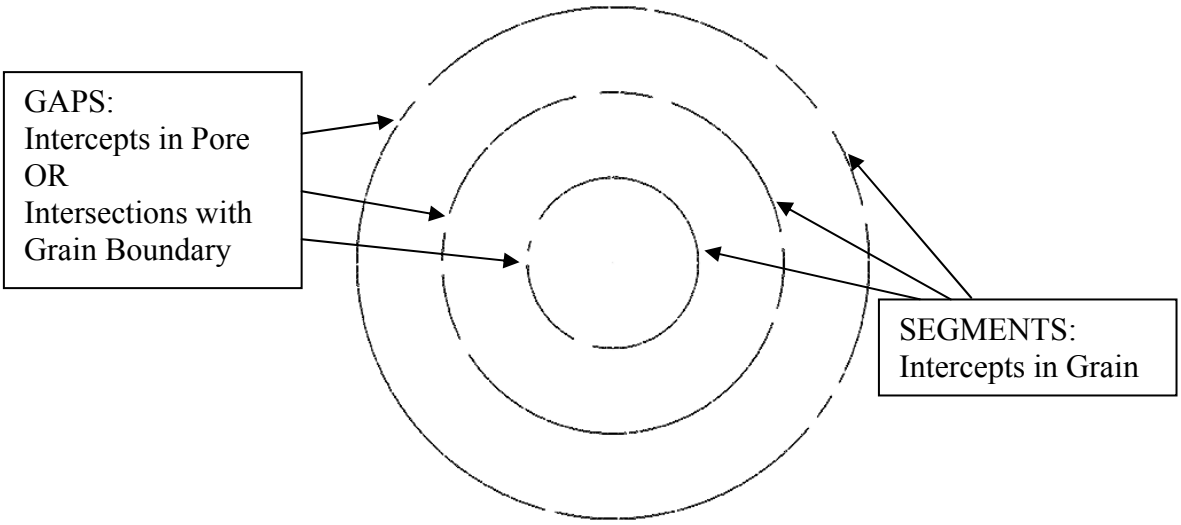

Fig. **3.9**: Illustration of Intercept Counting – Modified Test Pattern

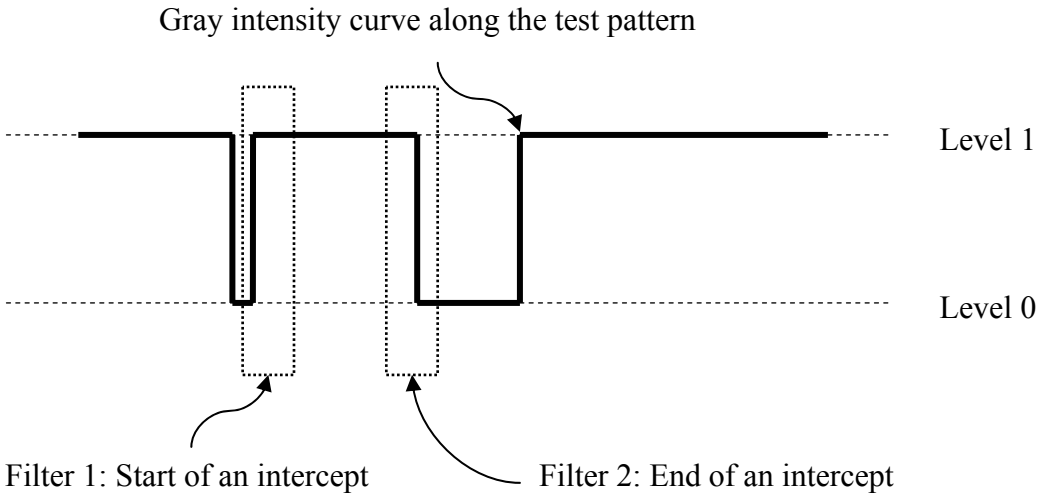

Fig. **3.10**: Step Filters Used in Intercept Counting

3.3.5.4 Step 4: Postprocessing and Error Estimation

In order to reduce the experimental errors, as was discussed in **3.3.5.2**, because it is assumed that the boundary width is trivial and can be ignored, the length of the eraser (3 pixels) needs to be added to the length of each intercept. It was achieved in the MATLAB program (Appendix **A.2**).

In order to make the measurement results practical, it is necessary to convert the data from pixels to a length unit, such as micrometer, using appropriate scales. The micrographs were at one of three magnifications: 200×, 500×, and 1000×. Scales corresponding to all magnifications are listed in Table **3.4**.

Table **3.4**: Scales Converting Pixel to Micrometer

Magnification	200×	500×	1000×
Scale (μm/pixel)	0.433	0.175	0.085

An error estimation was performed to verify the reliability of the results. Two criteria were used in this research. First, the total length of the modified pattern should match the original one. The difference between these two lengths was deemed as one of the candidates of experimental error. Second, the percentage of grain boundary width in the total intercept length is used as another candidate of experimental error. The larger one between these two candidates was used as the estimation of the experimental error, which was usually less than 6%.

The results of the intercept length representing grain size were presented in arithmetic frequency histograms as well as logarithmic frequency distribution curve. An example of the histogram is shown in Figure **3.11**.

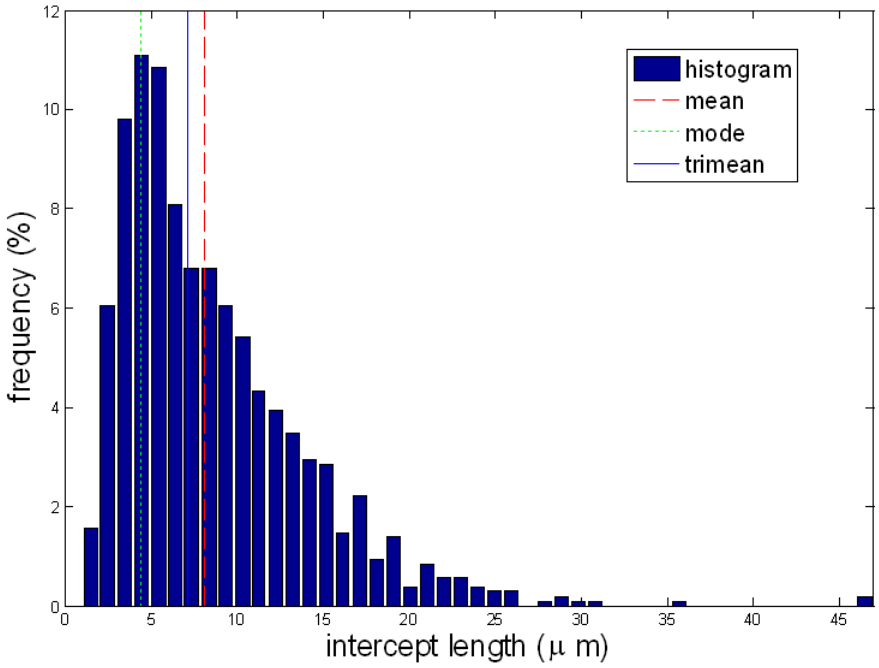

a. Arithmetic Frequency Histogram

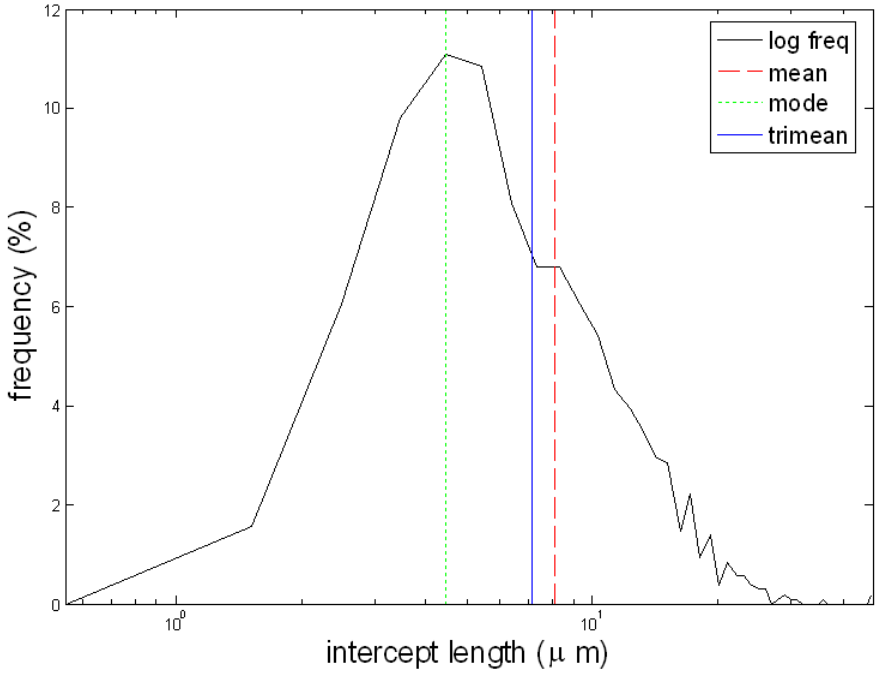

b. Logarithmic Frequency Distribution Curve

Fig. **3.11**: Results of Grain Size Distribution for Stainless Steal 316L Sintered at 1350°C (S79: Particle Size Mean Value 33.4μm, Die-compacted to 79% Relative Density)

3.4 Analysis of the Results

The grain size measurements as shown in Figure **3.11** are distributions of grain size. The result contains information not only about the average value but also the range in which grain sizes would fall. There are many ways to represent the distribution type of results. In this research, the concern is to find a specific variable that can accurately represent the average grain size so that it can be used in a numerical relation such as Equation **2.34**. The following section shows how this specific variable was found and why it is an effective representation.

3.4.1 Comparison of Mean, Mode and Trimean

There are several statistical concepts that are used to analyze experimental data: *mean*, *median*, *mode*, and *trimean*. Some of them are efficient (stable from sample to sample) to the central tendency of normal distribution data; others are efficient to skewed distribution data. Some are highly subject to sampling fluctuations; others are not that sensitive. A comparison of the definitions and characters of these concepts is provided in Table **3.5**.

For stainless steel 316L samples, all of the results showed that grain size distributions are positively skewed or skewed to the right if linear scales are used. In Figure **3.11.b**, the logarithmic frequency curve has a symmetric shape. It is also noted in [**47**] that most of the grain size distributions are log-normal. Figure **3.12** shows the fluctuations and the stability of the mean, mode and trimean from sample to sample for stainless steel 316L sintered at 1200°C and 1250°C.

Table **3.5**: Comparison of Mean, Median, Mode, and Trimean

Concept	Definition	Sampling Fluctuations	Normal Distribution	Skewed Distribution
Mean	Arithmetic average: the sum of all the data divided by the number of data.	sensitive	efficient	Less efficient
Median	The middle of a distribution	less sensitive	efficient	efficient
Mode	The most frequently occurring data in a distribution.	sensitive	efficient	efficient
Trimean	Trimean is computed by adding the 25th percentile plus twice the 50th percentile plus the 75th percentile and dividing by four: $(A_{25\%}+2A_{50\%}+A_{75\%})/4$	Least sensitive	Less efficient	efficient

Notice that *mode* values are much smaller than *mean* and *trimean* for both sintered temperatures. The standard derivations of these variables for both groups of measurement (Table **3.6**) show that the standard derivation of *mode* is the largest among all three variables measured for the same group, which means the *mode* is highly subject to sampling fluctuations as expected. Thus it should not be used as a representation of grain size in this research. Meanwhile, the values of *trimean* and *mean* are very close with the mean value slightly larger than the trimean, The standard derivations of both *trimean* and *mean* are relatively small. While either the *mean* or the *trimean* may be used for this type of distribution, the more popular and accepted concept, arithmetic *mean* is chosen to quantitatively represent the results of grain size measurement.

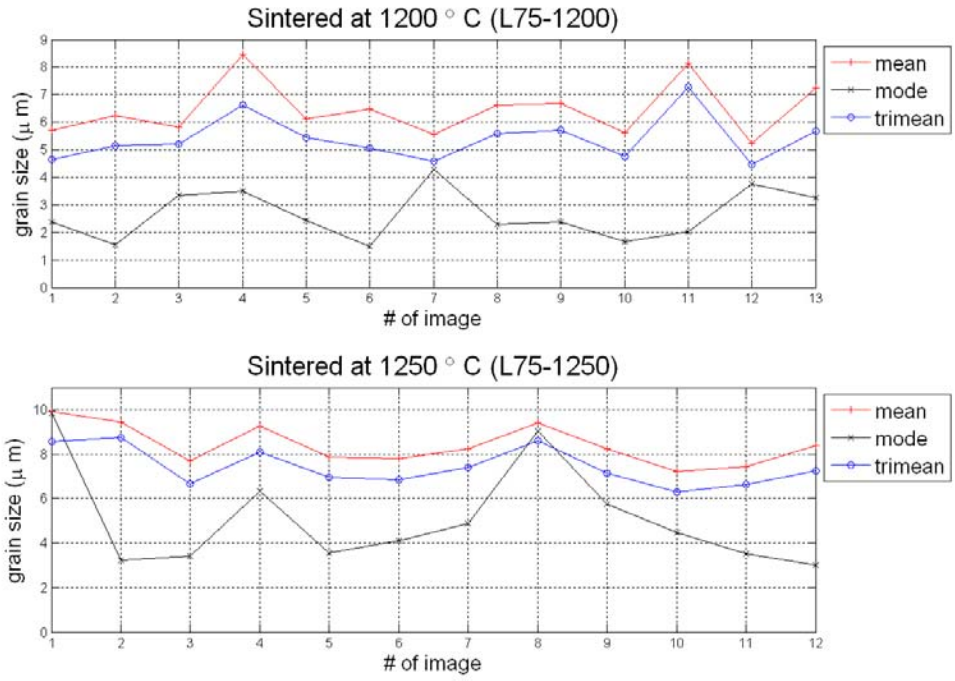

Fig. **3.12**: Comparison of the Stabilities of *Mean*, *Mode* and *Trimean* Results for Grain Size Measurement of Stainless Steel 316L Sintered at 1200°C and 1250°C (L75: Particle Size Mean Value 72.5μm, Die-compacted to 75% Relative Density)

Table **3.6**: Standard Derivation of *Mean*, *Mode* and *Trimean* from Image to Image for Grain Size Measurement of Stainless Steel 316L Sintered at 1200°C and 1250°C (L75: Particle Size Mean Value 72.5μm, Die-compacted to 75% Relative Density)

Sintering Temperature (°C)	Standard Derivation		
	Mean	*Mode*	*Trimean*
1200	0.98	0.90	0.81
1250	0.89	2.28	0.85

3.4.2 Summary of the Results

As it was listed in Table **3.2**, there are 6 samples with 3 different particle sizes and 2 different levels of green densities. The same sintering cycle was applied on every group of samples: free sintered in hydrogen at 10°C/min from room temperature to 1350°C and held for 1 hour. Along one sintering cycle, each group has 4 to 8 test points where the sintered sample was quenched in water to freeze the microstructure so that the grain size could be evaluated. The grain growth data are summarized in Table **3.7** and displayed in Figure **3.13**, where the mean and the distribution range result are shown as a function of time. The 25% value and 75% value have been used as lower and upper bounds, respectively. Due to the skewed distribution, the difference between the upper bound and the mean is slightly larger than that between the lower bound and the mean.

There are two factors that were expected to affect the grain growth data. One is the initial powder size; the other is the relative density of green compact. The test method of grain growth measurement was designed so that samples were prepared to study the influence of both factors. Detailed discussion on this topic can be seen in the next section.

Table **3.7**: Grain Growth Data with Distribution Boundaries for Stainless Steel 316L Free Sintered in Hydrogen at 10°C/min from Room Temperature to 1350°C and Held for 1 Hour. (Grain Size Unit: µm)

Temperature (˚C)	Lower Bound (25% value)	Mean	Upper Bound (75% value)	# of Images	Magnification
L75 (initial particle size 72.5 µm, green density 75%)					
1150	3.48	5.34	7.62	1	1000×
1200	3.22	5.42	8.12	13	1000×
1250	4.43	7.59	11.24	12	500×
1350[3]	10.55	16.32	24.02	4	200×
L79 (initial particle size 72.5 µm, green density 79%)					
1100	3.48	5.68	8.37	10	500×
1200	3.47	5.89	9.29	4	500×
1250	3.49	6.69	10.38	9	500×
1350[3]	10.10	15.96	23.77	9	200×
M75 (initial particle size 52.5 µm, green density 75%)					
1100	2.46	4.63	7.28	10	500×
1150	2.26	5.19	8.13	2	1000×
1200	4.45	6.64	9.32	5	500×
1250	3.20	6.62	11.01	2	1000×
1350[2]	9.07	14.37	20.65	5	200×
1350[3]	10.16	15.32	20.96	8	200×
M79 (initial particle size 52.5 µm, green density 79%)					
1200	3.38	5.77	9.10	11	500×
1250	3.48	5.94	9.38	10	500×
1350[1]	4.40	7.54	11.17	12	500×
1350[3]	8.46	14.16	21.34	15	500×
S75 (initial particle size 33.4 µm, green density 75%)					
1100	2.45	4.36	6.28	10	500×
1150	2.49	4.45	6.41	7	500×
1200	2.49	4.68	7.36	7	500×
1250	3.41	5.80	9.14	2	500×
1350[1]	4.38	7.01	11.07	1	500×
1350[2]	7.15	11.52	16.86	8	200×
1350[3]	9.10	13.71	19.78	7	200×
S79 (initial particle size 33.4 µm, green density 79%)					
1100	2.45	4.31	6.16	1	500×
1150	2.46	4.62	7.25	9	500×
1200	2.46	4.63	7.28	8	500×
1250	3.48	5.69	8.39	10	500×
1300	3.47	6.66	10.34	11	500×
1350[1]	4.45	7.14	11.29	10	500×
1350[2]	5.47	10.38	15.30	10	500×
1350[3]	7.41	12.82	19.21	16	500×

[1]:Sintered at 1350°C with no hold
[2]: Sintered at 1350°C with half hour hold
[3]: Sintered at 1350°C with 1 hour hold

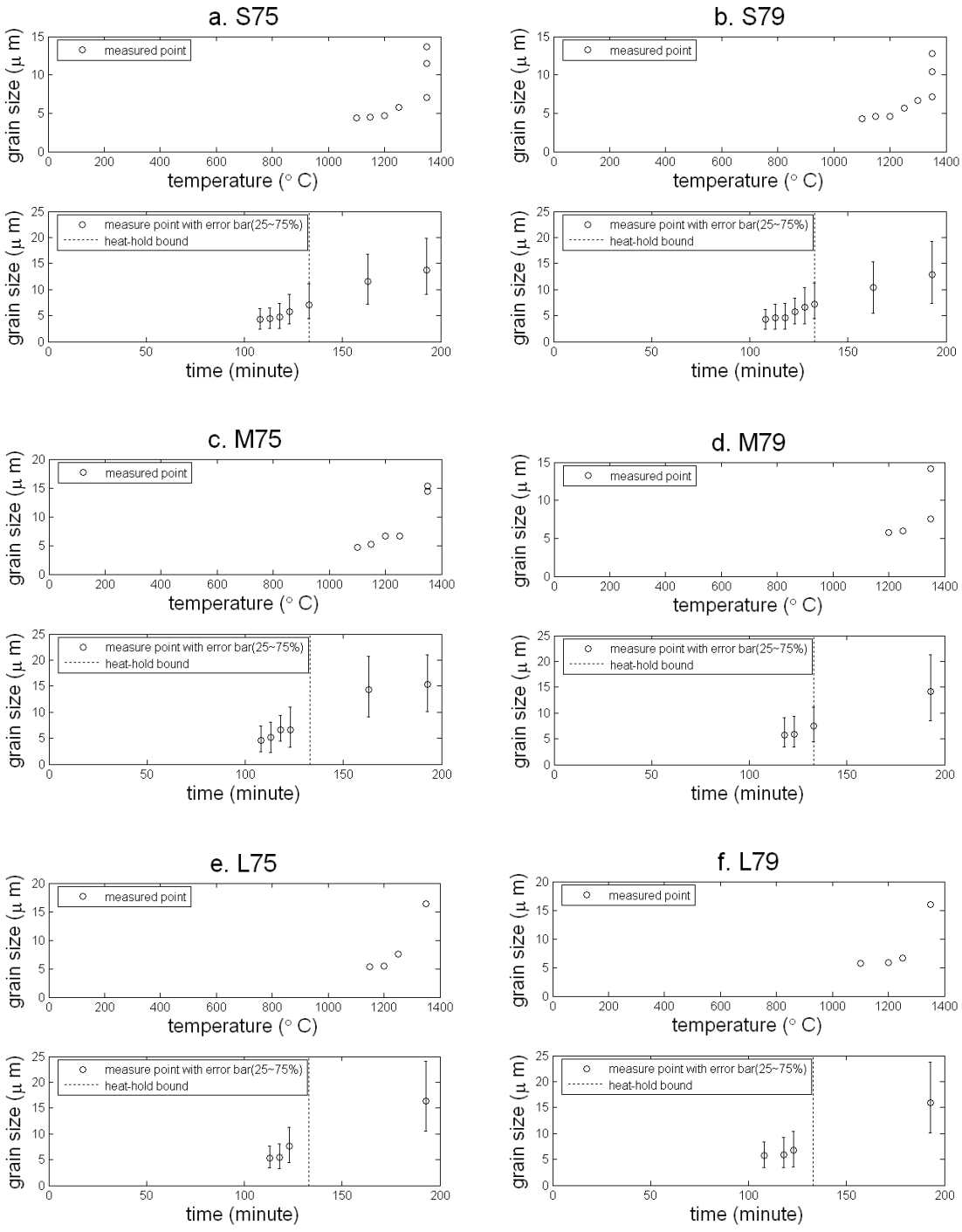

Fig. **3.13**: Grain Growth Trend for Stainless Steel 316L Free Sintered in Hydrogen at 10°C/min from Room Temperature to 1350°C and Held for 1 Hour. (Each Group with 2 Plots Showing the Relations between Grain Size and Sintering Temperature and Grain Size and Sintering Time)

3.4.3 Evolution of Grain Size Distribution

Reported in a previous study [31], the transition temperature between abnormal grain growth (AGG) and normal grain growth of stainless steel 316L (continuous material) is about 1200°C. One of the pieces of evidence was that a few large grains were seen to grow at accelerated rates before 1200°C. The corresponding histograms of grain size distribution had a wide grain size range with a few high frequency bars for large grain sizes. To characterize the grain size distribution for porous material such as stainless steel 316L powder compacts, the histograms throughout the sintering cycle should be reviewed.

A comparison on grain size distribution evolution during sintering is shown in Figure **3.14**. It is clear that histograms at sintering temperatures lower than the transition

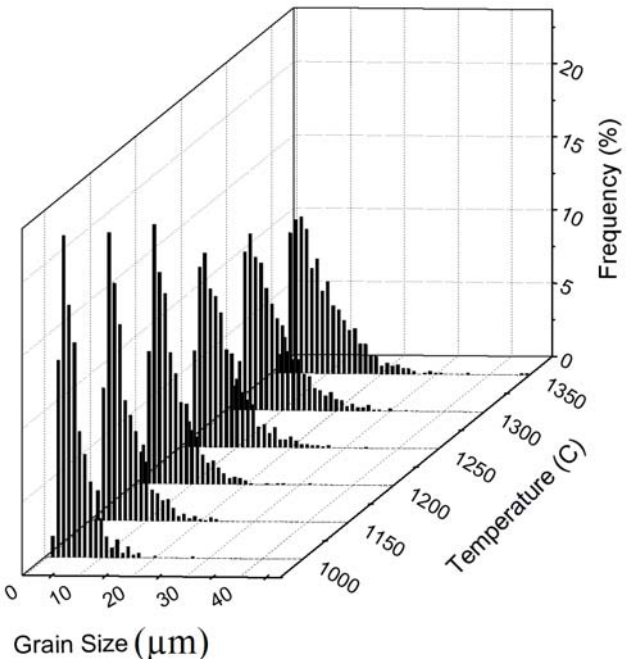

Fig. **3.14**: Comparison of Grain Size Distributions for Stainless Steel 316L (S79: Particle Size Mean Value 33.4μm, Die-compacted to 79% Relative Density) Free Sintered in Hydrogen at 10°C/min from Room Temperature to 1350°C. (Temperature Indicates Where Sintering Stops.)

temperature show a more concentrated distribution, i.e., a narrow range of grain size. The spread widens at higher temperatures, however, high frequencies of large grains did not occur at the higher temperatures. The reason might be that boundaries between powder particles and pores, and powder particles inhibit the rapid growth rate of those large grains. At low temperature, the densification rate was so slow that the gaps between particles (and of course grains) were not filled quickly enough for further growth of a large grain. While at high temperature, relatively large grains did appear (see Figure **3.15**) and the material got much denser as those large grains grew. However, large grains at this final stage of sintering were not indicative of AGG.

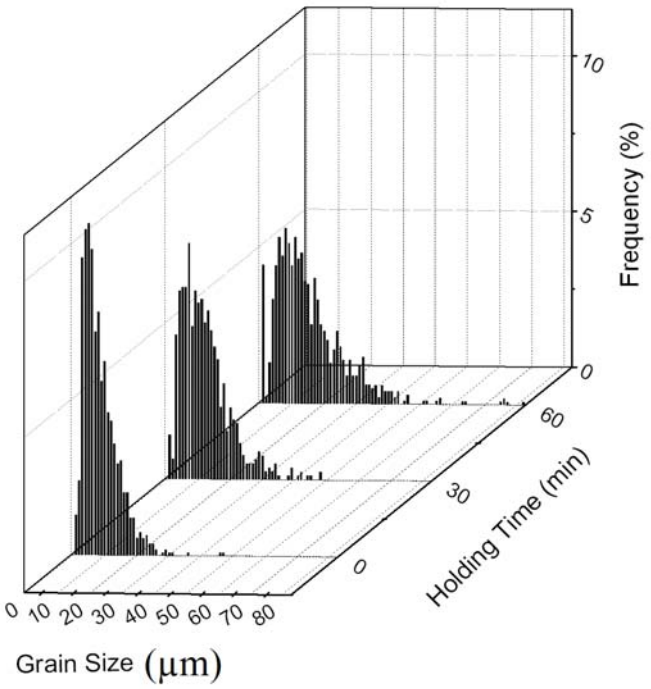

Fig. **3.15**: Comparison of Grain Size Distributions for Stainless Steel 316L (S79: Particle Size Mean Value 33.4μm, Die-compacted to 79% Relative Density) Free Sintered in Hydrogen at 10°C/min from Room Temperature to 1350°C and Held for 0, 30 and 60 minutes.

3.5 Grain Growth Simulation

The computer simulation of microstructure developments such as the grain growth process has been studied for decades. Depending on different grain growth mechanisms, a variety of models have been developed. These models can be categorized into two groups: curve fitting method and Monte Carlo method. Two-dimensional Monte Carlo models [49],[50],[51] incorporate realistic microstructure with different diffusion laws. They can describe grain growth behavior under certain idealized assumptions. In this research, however, the curve fitting method is used to predict grain growth behavior due to its accuracy and reliability.

It was shown in the last section that the mean value can be used to represent the grain size. These quantitative data have been abstracted from metallographs with grain microstructure. In order to apply these results into the FEM simulation of the sintering process, an empirical equation that can accurately describe the grain size change during sintering is needed. In this section, one grain growth model, chosen from several candidates, is described and parameters in this model are specified.

3.5.1 Grain Growth Models

Different grain growth laws have been developed based on different mechanisms. For normal grain growth, a parabolic law and a power law have been used in many grain growth studies [35],[52],[53],[54],[55],[56]. Both assume that grain size is a function of time. The parabolic law model is

$$G^2 - G_0^{\ 2} = K\,t\,, \qquad \text{Eq. } \mathbf{3.1}$$

and the power law model is

$$G = Kt^n\,, \qquad \text{Eq. } \mathbf{3.2}$$

where G is the mean grain size at time t, G_0 is the initial mean grain size, K is a material constant, and n is the grain growth exponent.

Both the parabolic law and power law predict the grain growth in ceramics such as alumina. However, for metal alloys such as austenitic stainless steel, because of the assumption that atomic diffusion in grain growth is a simple thermally activated process, an Arrhenius-type grain growth equation has been commonly used. Based on different experiments, various forms of Arrhenius-type grain growth equations have been developed—a sample of these expressions as reported in the literature is shown in Table **3.8**. Type 3 in this table was chosen for this research due to its popularity for stainless steel 316L.

$$\frac{dG}{dt} = \frac{A\exp(-Q_G / RT)}{G} \qquad \text{Eq. } \mathbf{3.3}$$

where A is a pre-exponent factor, Q_G is the activation energy for grain growth, R is the universal gas constant, T is the absolute temperature and G is the instantaneous grain size. As was mentioned in **3.2**, the activation energy for grain growth shifts from an upper level to a lower level after a transition temperature is reached. For stainless steel 316L, this temperature is approximately 1200°C. Therefore, for this research, the activation energy values for 316L type stainless steel reported in [**34**] were used—specifically 316

kJ/mol was used for temperatures less than 1200°C and 50.0 kJ/mol when temperatures greater than 1200°C.

Table **3.8**: Sample of Literature on Empirical Grain Growth Equation for Continuous Material Stainless Steel

	Equation	Material	Q_G (kJ/mol)	Reference
1	$G^n - G_0^n = At\exp(-Q_G/RT)$ n is an assumed integer ranging from 3 to 5; A is a material constant; Q_G the activation energy for grain growth; G_0 the initial mean grain size.	Austenitic Stainless steel	310±80	[35], [36]
2	$G - G_0 = At^n\exp(-Q_G/RT)$ n is an assumed integer; A is a material constant; Q_G the activation energy for grain growth; G_0 the initial mean grain size.	NdFeB	215~238	[37]
3	$\frac{dG}{dt} = \frac{A\exp(-Q_G/RT)}{G}$ A is a material constant; Q_G, the activation energy for grain growth, shifts to a lower value when temperature is above 1200°C.	Steel	208	[38]
		Stainless steel 316L& Stainless steel 316LB	316 / 50	[34]
		Stainless steel 316	280	[39]
		Stainless steel 316L	246	[18]

3.5.2 Curve Fitting Results

In order to determine the grain growth curve as a function of temperature, both the pre-exponent factor and the initial grain size must be determined. They were experimentally determined by plotting average grain size as a function of time and temperature. The measurement procedure described earlier in **3.3.5** was used to determine the mean grain size. The curve fitting process was done by a computer code in MATLAB (see Appendix **A.3**). The curve fitting results are shown in Figure **3.16**.

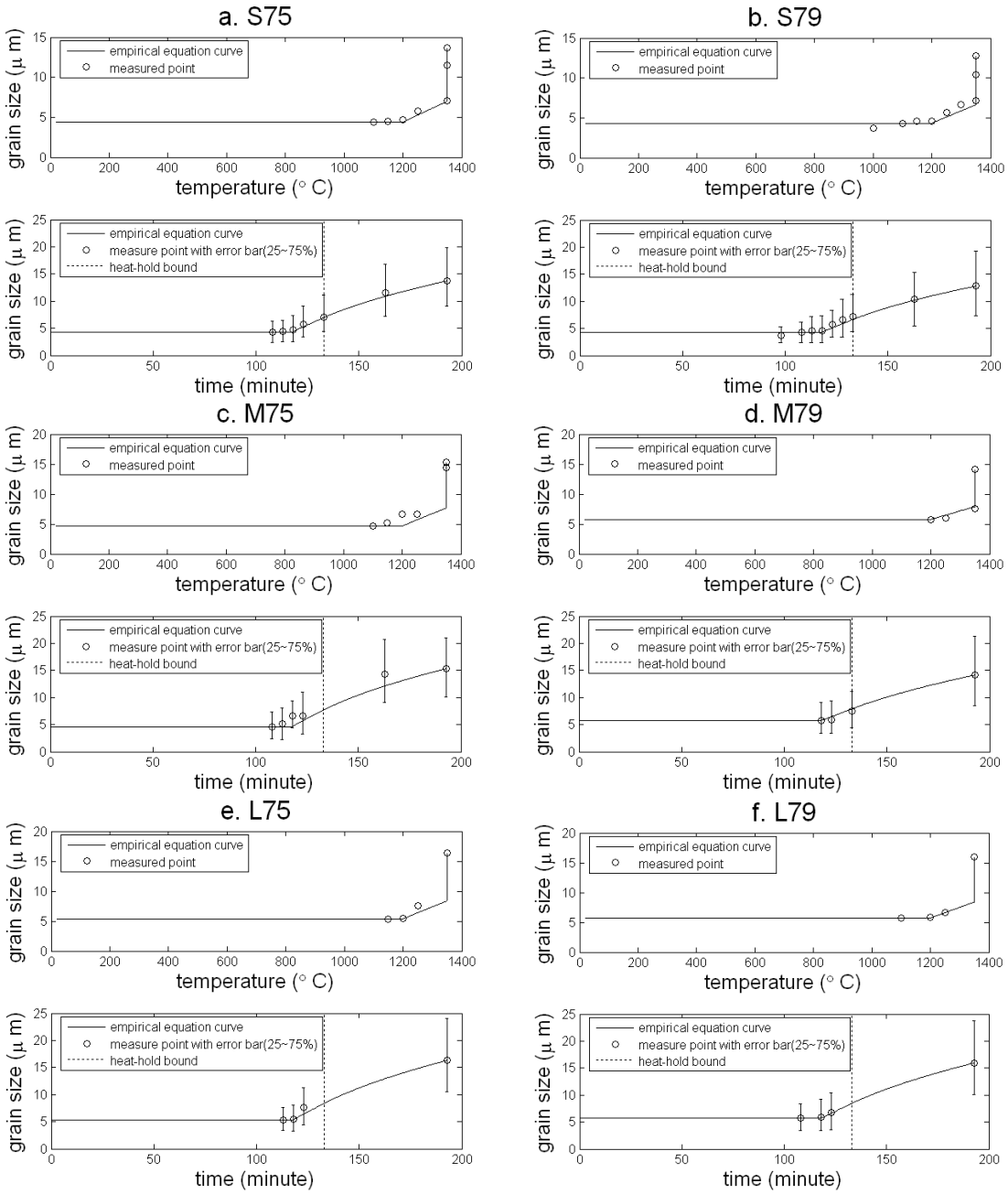

Fig. **3.16**: Curve fitting for Grain Growth Trend of Stainless Steel 316L Free Sintered in Hydrogen at 10°C/min from Room Temperature to 1350°C and Hold for 1 Hour. (Each Group with 2 Plots Showing the Relations between Grain Size and Sintering Temperature and Sintering Time; S75: initial particle size 33.4 μm, green density 75%; S79: initial particle size 33.4 μm, green density 79%; M75: initial particle size 52.5 μm, green density 75%; M79: initial particle size 52.5 μm, green density 79%; L75: initial particle size 72.5 μm, green density 75%; L79: initial particle size 72.5 μm, green density 79%)

All the empirical curves fit well with the experimental results, especially in groups S75 and S79, which have more than 7 measurement points, i.e., quenched samples. Additionally, the assumption of a transition point during grain growth was verified by the measurement points near the transition temperature. The mean grain size values below 1200°C were almost constant, while at points beyond 1200°C, grain size started to increase. Although in at least one case (M75) several mean grain size values were a little off the fitting curves (see Figure **3.16.c**), the whole grain growth trend was described by the curve and always within the 25% and 75% bounds of the experimental results.

The pre-exponential factor and the initial grain size were obtained by averaging measurements of grain size at the initial and final states of the sintering cycle. The results are listed in Table **3.9** and plotted in Figure **3.17**.

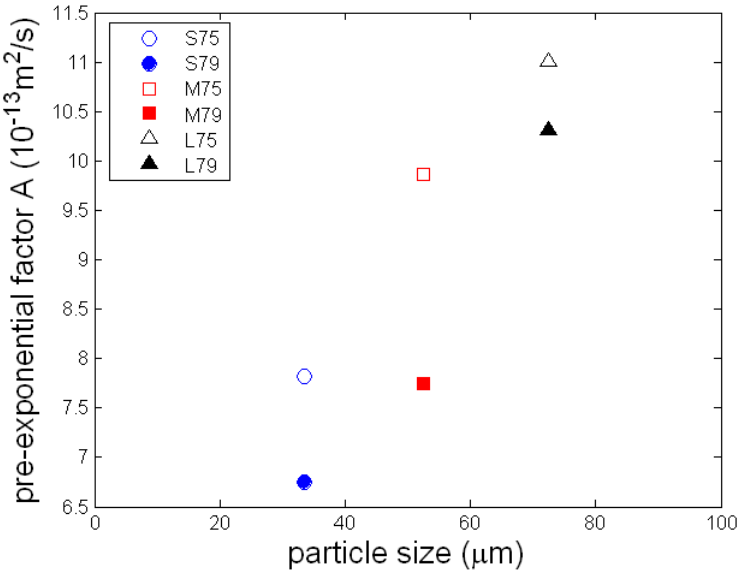

Fig. **3.17**: Particle Size and Green Density Effects on Pre-exponential Factor

Table **3.9**: Comparison of the Results of the Initial Mean Grain Size and Pre-exponential Factor

Curve	L75	L79	M75	M79	S75	S79
A ($\times 10^{-13} m^2/s$)	11.01	10.31	9.86	7.75	7.82	6.75
Initial Mean Grain Size (μm)	5.34	5.68	4.63	5.77	4.36	4.31
Start Pt. (˚C)	1150	1100	1100	1200	1100	1100

3.5.3 Influence of Particle Size and Green Density

The grain size measurement test was designed in such a way that 6 groups of samples with 3 different mean particle sizes and 2 green density levels were tested. The purpose was to study the influence of mean particle size and green density on the grain growth. Figure **3.18** a, b and c show the grain growth curves of 3 groups with mean particle size of 33.5μm, 52.5μm and 72.5μm, respectively. Each of the graphs shows two curves representing a different green density level, 75% and 79%. The curve with a lower green density has a smaller initial grain size, but a higher grain growth rate and a larger final grain size.

Figure **3.19** a and b show the same grain growth curves but organized by density, 75% and 79%, respectively. Each image contains 3 curves of the same green density but with different initial mean particle sizes. All the curves have similar growth trend; however, it is clearly shown that the group with the larger initial particle size also has larger final grain size. The initial and final grain sizes are also plotted in Figure **3.20**, which shows the relation between grain size and particle size.

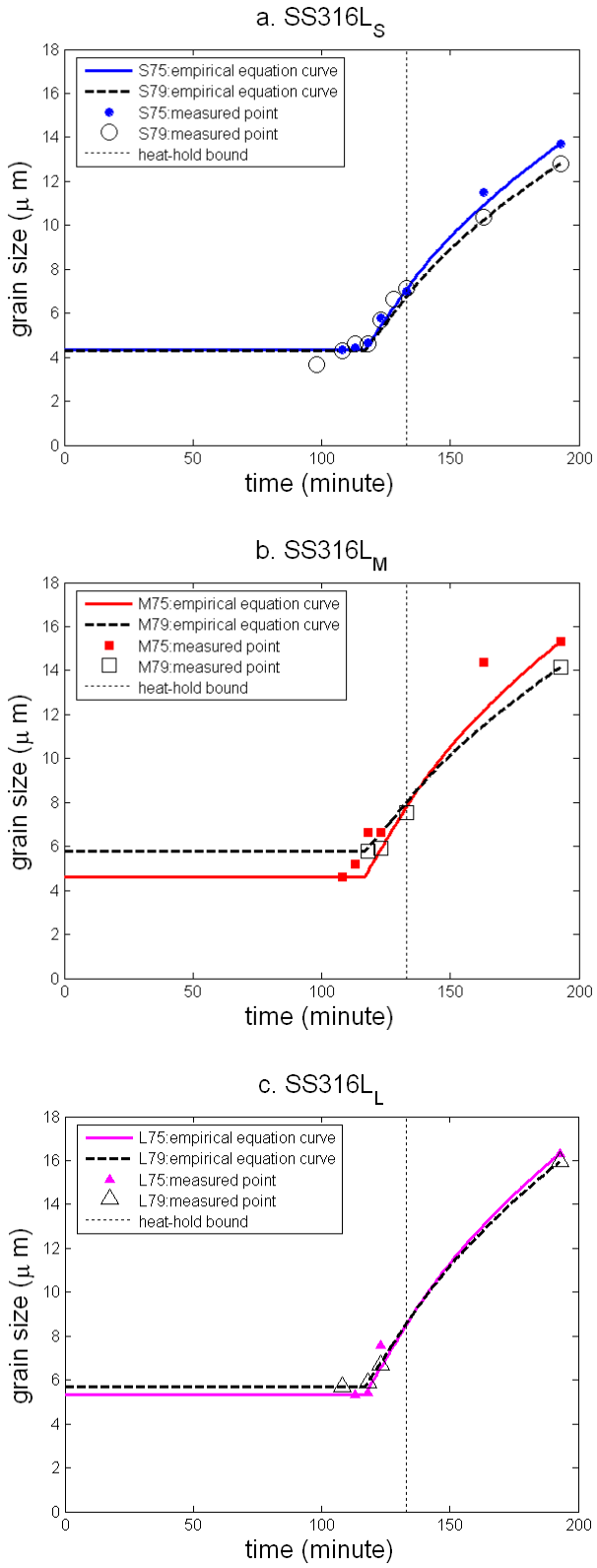

Fig. **3.18**: Comparison of Grain Growth Curves with Different Mean Particle Size

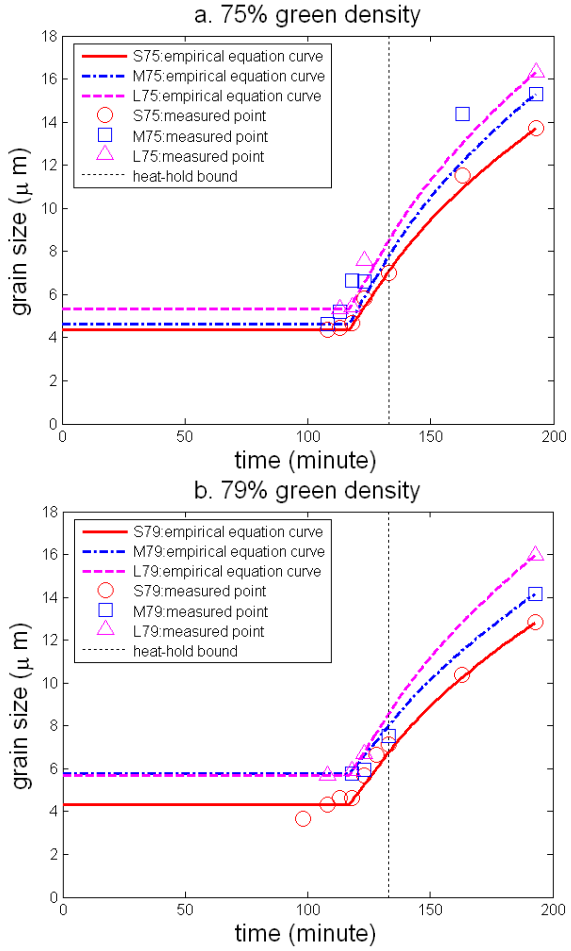

Fig. **3.19**: Comparison of Grain Growth Curves with Different Green Density

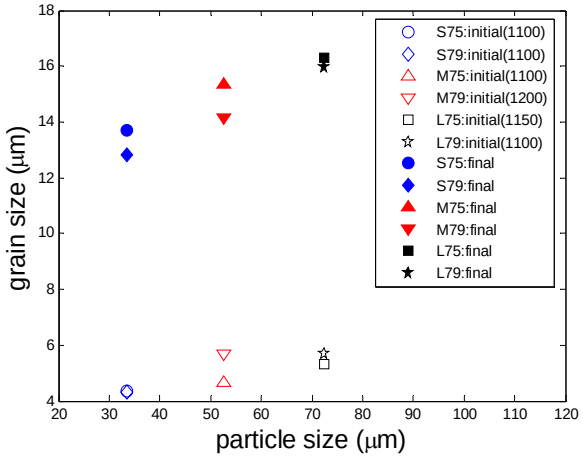

Fig. **3.20**: Particle Size Effect on Initial and Final Grain Sizes for Stainless Steel 316L

3.5.4 Convergence of the Curve Fitting

Using the computer code attached in Appendix **A.3**, the grain growth fitting curve was obtained by numerically integrating the grain growth rate equation. The final grain size equaled the summary of all the grain size increments. This accumulating process was affected by the choice of time increment and thus the total number of time steps. Due to the rounding error in the numerical integration process, large time steps did not produce a converged result for the pre-exponential factor as shown in Figure **3.21**

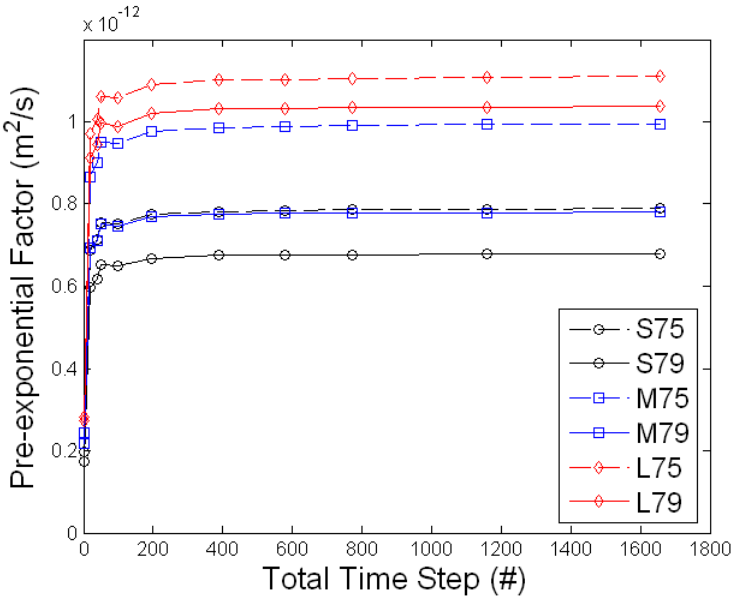

Fig. **3.21**: Comparison of the Convergence for Pre-exponential Factor of Stainless Steel 316L (S75: initial particle size 33.4 µm, green density 75%; S79: initial particle size 33.4 µm, green density 79%; M75: initial particle size 52.5 µm, green density 75%; M79: initial particle size 52.5 µm, green density 79%; L75: initial particle size 72.5 µm, green density 75%; L79: initial particle size 72.5 µm, green density 79%)

Specifically, the data points in the figure correspond to time increment lengths (in seconds) of 6000, 600, 300, 240, 120, 60, 30, 20, 15, 10, and 7, from left to right,

respectively. It is clear that the pre-exponential factor tends to converge to a constant after the time increment decreases to 30 s, which means a total time step number greater or equal to around 650. This limitation of time increment will be applied in the selection of time increment length in the FEM simulation of sintering.

3.6 Conclusions

This chapter studied the grain growth behavior for stainless steel 316L. A circular intercept procedure was developed to capture the grain growth measurement of a porous material. Details on how the procedure was designed to work efficiently, such as etching steps and the intercept counting algorithm, were introduced in this chapter. For the temperatures at which grain growth was measured, the grain size distribution was observed to be a log-normal type (skewed to the right) and the grain size was quanitifed using the mean grain size. The grain growth trend was accurately represented by an Arrhenius type empirical equation.A transition point dividing the abnormal grain growth and normal grain growth, as reported in several previous studies, was quantitatively represented by a shift of activation energy for grain growth. The rate form equation was numerically integrated with a computer code programmed in MATLAB. The influences on particle size and green density levels on the fitting curves were discussed. It was found that the pre-exponential factor is at the magnitude of $1 \mu m^2/s$ and monotonically increases as particle size increases or green density decreases. The time increment limitation in the numerical integral of the grain growth rate equation was also described and will be incorporated in the FEM simulation introduced in next chapter.

Chapter 4

Simulation Process and Results

In general, sintering is a relatively slow process, which may last hours. However, it is still time-dependent and should be treated as a quasi-static problem. Accordingly, there are opportunities to investigate what happens during the long process of sintering. This research presents a study on the simulation of the entire sintering process, not just the final result. The study considers that distinct mechanisms dominate different stages during sintering. Consequently, that information is used to develop a simulation that is valid throughout the sintering process.

4.1 Overview of the Sintering Simulation

With the development of, and improvement in, computer technology, research devoted to sintering simulation has flourished in recent years. For example, Riedel and co-workers [11],[59],[60],[16],[61],[62] have implemented a viscoelasticity model (Equation **2.2**) in several FEM applications on sintering simulation in association with pressing simulation. Their model accounts for grain boundary diffusion, volume diffusion and surface diffusion mechanisms in sintering. It can be applied in commercial FEM software to solve industrial problems. Shinagawa and co-workers [21],[63],[64] have used a viscoplasticity model in association with a microscopic model at the particle level that simulates the neck growth behavior in the intermediate stage of sintering. On the

multiscale simulation level, Mähler and Runesson [65],[66] have presented a mesomechanics approach to sintering simulation that uses a representative volume element on the particle level in association with the viscoplasticity theory. This model accounts for the interaction between a particle level unit cell and the macroscale level continuous model. Most recently, Mori and co-workers [67],[68],[69],[70] have developed a micro-macro method for sintering simulation that employs the Monte Carlo method to obtain the shrinkage strain rate which can be used in the finite element method as a viscoplastic strain rate. The grain growth behavior is successfully simulated by the Monte Carlo method on a two-dimensional level.

In this research, a viscoelasticity model is employed to the sintering simulation. Not only the final shrinkage, but also the densification during the entire sintering process is studied. This refinement helps to advance the understanding of each dominating mechanism, when the mechanism comes into play, and how its role evolves.

4.2 Physical Problem Description

The physical problem to be simulated is the sintering of single-punched green compacts which were made from the 3 powder groups shown in Table **3.1**. Each compact is cylindrical with a 12.58 mm diameter and a 12.08 mm height in the green state. The bulk density is approximately 82% with variation throughout the cross section area. The samples were made with 0.5 wt% Acrowax lubricant debound at 450°C for 2 hours and presintered at 900°C for 30 minutes. The sintering process starts at room temperature, and increases at a rate of 10°C/min up to 1350°C, when the temperature is held for 1

hour. The axial shrinkage curves (Figure 2.2) were recorded using a dilatometer. The final axial shrinkages range from 3.16% for compacts with small particle size distribution to 2.01% for compacts with large particle size distribution. Note that the debinding and presintering processes are not to be considered in this research because there is no major shrinkage due to heating in these periods.

4.3 Determination of the Parameters

Theoretically, metal powder compacts are discontinuous material due to the existence of void space in the porous body. However, the material can be treated as continuous with equivalent parameters that relate to relative density or porosity. Because the sintering process involves high temperature situations, several of the material parameters will be represented as functions of temperature. An introduction on how the material parameters in the FEM model are obtained is presented in this section.

4.3.1 Powder Characterization

The stainless steel 316L water atomized powders were supplied by Hoeganeas, Inc. The source powders were sieved through different meshes to obtain 3 groups of powders with different particle size ranges, as shown in Table **4.1**.

Table **4.1**: Powder Sieving Information

Group #	Mesh size	Opening, (μm)	Powder size range, (μm)
SS316L-L	270	53	53 and upper
SS316L-M	500	25	25~53
SS316L-S			25 and lower

Powder characteristics such as particle size, apparent density, tap density and pycnometer density of each group are shown in Table **3.1**. Mean values for powder sizes of stainless steel 316L-S, 316L-M, and 316L-L are 33.4μm, 52.5μm, and 72.5μm, respectively. The 316L-S group has the highest Hausner ratio (the ratio of the tap to apparent densities). The Hausner ratio provides an indication of the degree of shape irregularity. The higher the Hausner ratio, the more irregular the particles and therefore the higher compressibility. In the die compaction tests, this was confirmed when, for the same green density, the pressure needed by the 316L-S group was smaller than that needed by the other two groups.

4.3.2 Define Elasticity and Viscosity

The elastic modulus is dependent on temperature. The higher the temperature, the smaller the elastic modulus. Additionally, the elastic modulus of a porous material is smaller than that of the bulk solid material. According to investigations of the variation of the elastic modulus with respect to porosity, the average porosity is important and many attempts have been made to relate properties to this parameter. In this research, however, numerical experiments demonstrate that the final result of the sintering simulation is not

sensitive to small changes in elastic modulus. Accordingly, a constant Young's modulus [1] is used such that

$$E = E_0 \rho^Y , \qquad \text{Eq. } \mathbf{4.1}$$

where E_0 is the full density elastic modulus which will decrease as temperature decreases. According to the ASM Handbook [46], E_0 is approximately 140GPa at 500°C, and the exponent Y equals 3.4 for sintered steel. For this work ρ, the bulk relative density equals 82%. Thus, the constant Young's modulus equals 69.3GPa. Additionally, a constant Poisson's ratio, 0.28, is used.

As discussed earlier (section **2.3.4**), an Arrhenius temperature relation (Equation **2.28**) is used to describe the apparent viscosity in a thermally activated viscous flow. According to some numerical experiments, the pre-exponential factor, η_0, usually falls in the range of 790MPa·s and the activation energy is equal to 20.0kJ/mol [58].

4.3.3 Define Sintering Stress & Transition Temperature Parameters

As stated earlier (section **2.4.1**) the sintering stress is treated as a function of relative density, surface tension, and average grain size (Equation **2.34**). The relative density is updated using the volumetric strain components. According to a previous study [3], the surface tension energy of the material, ω, is 2.0 J/m^2. The grain size, G, is updated using the empirical differential equation (Equation **3.3**) obtained from the grain growth measurement introduced in Chapter 3. The activation energy for grain growth is 316kJ/mol for temperatures less than approximately 1200°C and 50.0 kJ/mol when

temperatures are greater than approximately 1200°C. The pre-exponential factor, A, can be found in Table **3.9**. Since the green compacts have relative density of 82%, which is slightly larger than those samples used in the grain size measurement, the results of samples with 79% relative density are used in the sintering simulation. For the 316L-L group, A is $10.31\times10^{-13}m^2/s$; for 316L-M, A is $7.75\times10^{-13}m^2/s$; and for 316L-S, A is $6.75\times10^{-13}m^2/s$.

4.3.4 Apply the Grain Growth Model

In each time increment, the grain size is updated by integrating the empirical differential grain growth equation (Equation **3.3**). It was implemented in the CREEP subroutine in ABAQUS via a solution-dependent state variable. In SinSolver, it is achieved in a subroutine that calculates grain size for every increment. It should be noted that this numerical integration process is sensitive to the selection of the time increment length which was described earlier (Figure **3.21**). The same limitation of time increment is applied in the selection of time increment length in ABAQUS and SinSolver simulations.

4.3.5 Update Porosity/Relative Density

In every time increment, the porosity/relative density is updated with the strain component. In this research, geometric nonlinearity should be accounted for due to large deformation in sintering. In ABAQUS, the logarithmic strain was used for geometrically

nonlinear analysis. Accordingly, the relative density can be described in terms of the logarithmic strain components,

$$\rho = \rho_0 \exp(-\varepsilon_{kk}), \qquad \text{Eq. } \mathbf{4.2}$$

where ρ_0 is the initial density, ρ is the final density, and $\varepsilon_{\mathbf{kk}}$ is the volumetric strain. In the CREEP subroutine of ABAQUS, ε_{kk} is equal to the swelling strain $\bar{\varepsilon}^{sw}$, which is updated at the beginning of each increment.

4.3.6 Define Thermal Strain

The thermal strain, $\boldsymbol{\varepsilon}^{t}$, is caused by thermal expansion/contraction according to $\alpha \Delta T$. Based on the assumption of the transition temperature for sintering stress, the thermal expansion will dominate only when the temperature is lower than the transition temperature. To obtain the temperature dependent behavior of the thermal expansion coefficient α, dilatometry data will be obtained. In this research, the measurement of the thermal expansion coefficient was performed for stainless steel 316L compacts with 4 different levels of green density, ranging from 73% to 96%. The results are shown in Figure **4.1** with a comparison with the thermal expansion coefficient values listed in handbook [29] for fully dense material.

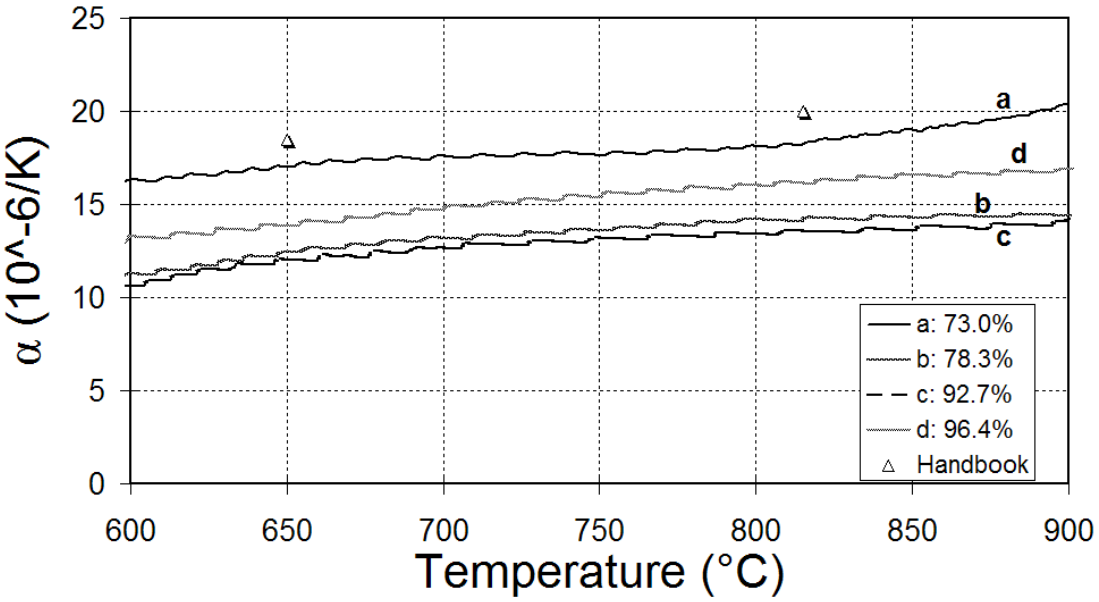

Fig. **4.1**: Average Thermal Expansion Coefficient vs. Temperature for 316L Stainless Steel Powder Compact with Different Green Density

The comparison shows that the thermal expansion coefficient of porous material is in general slightly smaller than that of fully dense material. It monotonically increases with temperature. But no straightforward relation has been found between the thermal expansion coefficient and the green density. Considering the facts that the thermal expansion is not the major concern in this research, and the deformation due to sintering densification is much larger than the thermal expansion, a linear empirical equation is used to describe the thermal expansion coefficient α as a function of temperature,

$$\alpha = c_1 T + c_2, \qquad \text{Eq. } \mathbf{4.3}$$

where c_1 and c_2 are measured material constants. For stainless steel 316L, c_1 is 4.47×10^{-9} K^{-2} and c_2 is 12.1×10^{-6} K^{-1}. According to the experimental results, there is no particle

size effect on the thermal expansion coefficient. Therefore, the same thermal expansion coefficient equation was used for all simulations for each of the 3 groups.

4.4 Application in SinSolver

The one-dimensional version of the sintering simulation program (SinSolver) is programmed to be a supporting tool and a comparison and verification of ABAQUS. The code is implemented in MATLAB using the FEM scheme introduced in Appendix **B.1**. The viscoelasticity model in SinSolver is the same as that in ABAQUS. As mentioned in the previous section, the transition temperature is set as a trigger to determine when the creep deformation starts in SinSolver. The sintering stress is assumed to be zero until the transition temperature is reached. The grain growth equation introduced in the previous section is also employed in the SinSolver. As it was studied in **3.5.4**, the time increment is set at 30s to obtain an accurate and convergent result.

4.4.1 Architecture

The basic structure of SinSolver is shown in Figure **4.2** with a list of the main program and subroutine names in SinSolver shown in Table **4.2**. All the MATLAB codes have been attached in Appendix **B.2**.

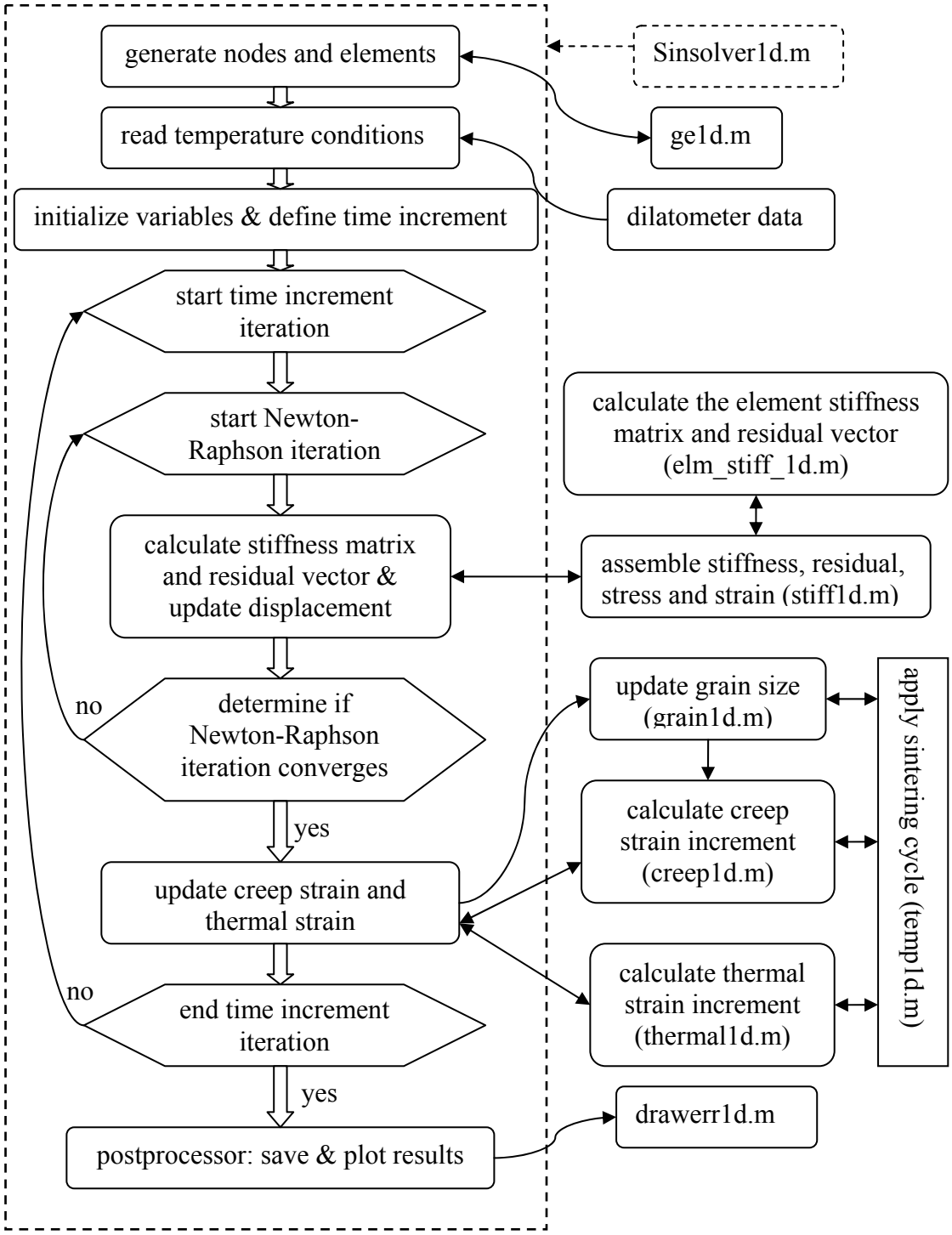

Fig. **4.2**: Flow Chart of SinSolver

Table **4.2**: Components of SinSolver

Name of the Routine	Function
sinsolver1d.m	Main program
ge1d.m	Define the geometric shape, generate nodes and elements.
stiff1d.m	Assemble the stiffness matrix, the residual vector, stress vector and strain vector.
elm_stiff_1d.m	Calculate the element stiffness matrix and residual vector.
grain1d.m	Update grain size.
creep1d.m	Calculate the creep strain increment.
thermal1d.m	Calculate the thermal strain increment
drawerr1d.m	Plot results
temp1d.m	Apply temperature conditions in the sintering cycle

4.4.2 Results

SinSolver yields the result of axial shrinkage of the metal compact. Simulations have been run for three groups of stainless steel 316L powder compact at 82% green density with three different particle sizes: S83, M83 and L83.

Figure **4.3** shows the comparison of the experimental data and simulated results by the one-dimensional solver. During the initial heating the axial shrinkage is negative due to the thermal expansion which dominates the process at low temperatures. Also, note that the final shrinkage is relatively small (3%). This illustrates that the sintering occurs in the initial to intermediate stage, which is dominated by the grain boundary diffusion. For all three groups of powder compacts, the simulation successfully captures the trend of the dilatometry plot, though there is a slight difference at the beginning of the shrinkage curve. The accumulated shrinkage is slightly larger than the measurement. The error might due to nonlinear thermal expansion behavior during the cooling period.

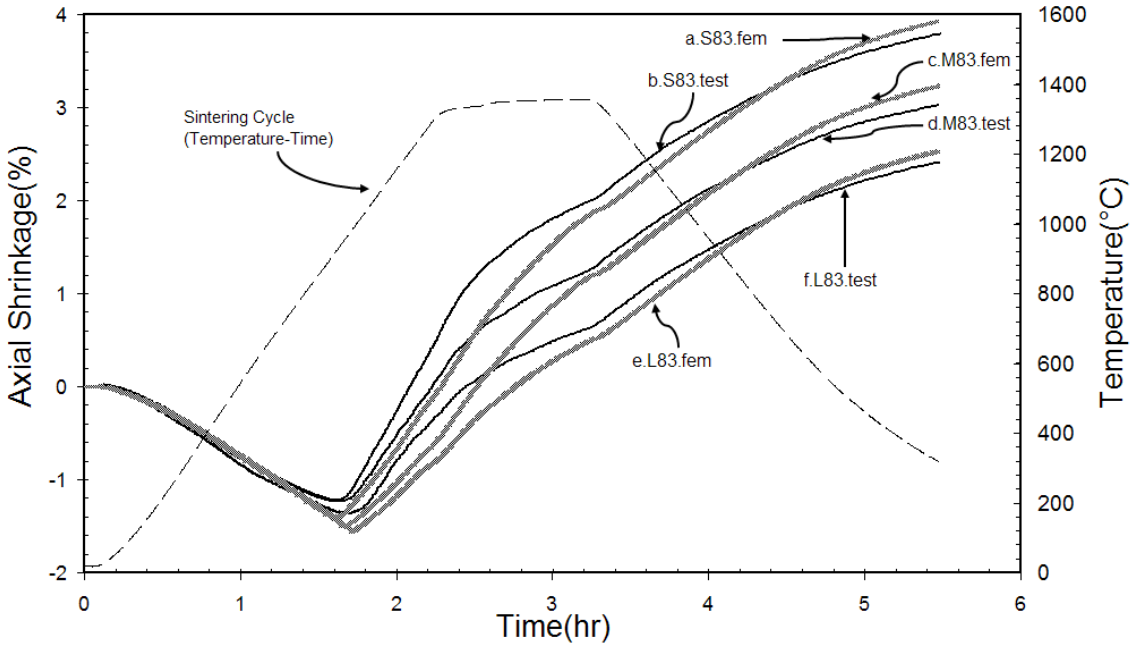

Fig. **4.3**: Comparison of Experiment Data and the SinSolver Results for Dilatometry Plots of Shrinkage vs. Time. (Die Compacted Stainless Steel 316L Compacts Heated at 10 °C/min to 1350°C, Held for One Hour, and Cooled at 10 °C/min to 300°C. Particle Mean Size: S83--33.4μm, M83--52.5μm, and L83--72.5μm)

The results from SinSolver are helpful in understanding how the sintering model works and locating the range of the material parameters that need to be determined in the model. The one-dimensional problem that SinSolver solved does not use the deviatoric stress component. Therefore, the creep strain rate results are only influenced by the ratio between the equivalent hydrostatic pressure and the bulk viscosity modulus. This simplification might be the reason why the simulation does not fit the test perfectly.

4.5 Application in ABAQUS

First, the density distribution and residual stress from the compaction simulation[44] are transferred into the sintering analysis as initial conditions. An axisymmetric finite element model is created in ABAQUS Standard version 6.3 for the cylindrical sample. The cross section used to create the model is shown in Figure **4.4**. Within ABAQUS, the bilinear axisymmetric element (CAX4) is used. The sintering simulation consists of two problems: heat transfer analysis and creep analysis. The history output of the temperature field, i.e., the temperature field as a function of time, is written in the ABAQUS result file and transferred into the sintering analysis as the prescribed thermal conditions. A quasi-static analysis with transient response to time-dependent material behavior is then performed. Each step in the procedure is described in more detail in the following sections.

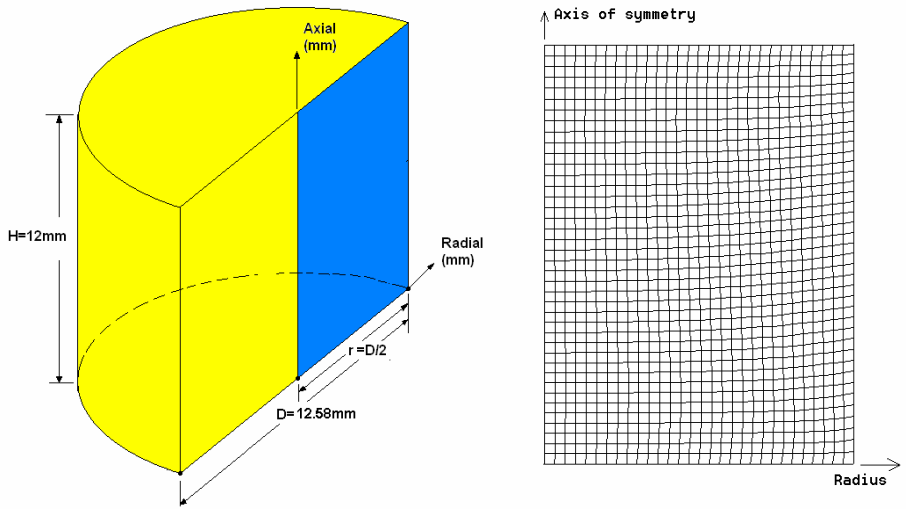

(a) Geometry (b) Mesh

Fig. **4.4**: Geometry and Mesh of the FEM model

4.5.1 Procedure

The ABAQUS code for the sintering simulation is defined in an input file (*.inp) in association with a user-defined subroutine file (*.for), which is programmed in FORTRAN (see Appendix **B.3**). The generation of the geometric model and the finite element mesh is done in the input file, followed by the definition of the material model. The creep model is referred to the user-defined subroutine, in which the creep rate equation is defined, as well as the grain growth equation. Several solution dependent state variables are also employed in the subroutine to update variables, such as sintering stress, grain size, viscosity, etc. These variables are later plotted for further analysis. The initial conditions and boundary conditions are also defined in the input file. The last part in the input file is the definition of control parameters for the quasi-static analysis and output commands. The same time increment (30s) is used as it is in SinSolver. A flowchart detailing the procedure is shown in Figure **4.5**.

4.5.2 Determination of the Initial Conditions—Compaction Simulation

The compaction models can be divided into two categories: phenomenological and micromechanical. The more commonly used phenomenological models are the Cam-clay model, the classic Drucker-Prager model, the modified Drucker-Prager/CAP model, and the Shima-Oyane model. Each model can describe the compaction performance within a certain density range. The micromechanical models are derived from particle-particle interactions. These models are often used to solve dynamic problems, such as impact, using the discrete element method (DEM). This research uses the modified

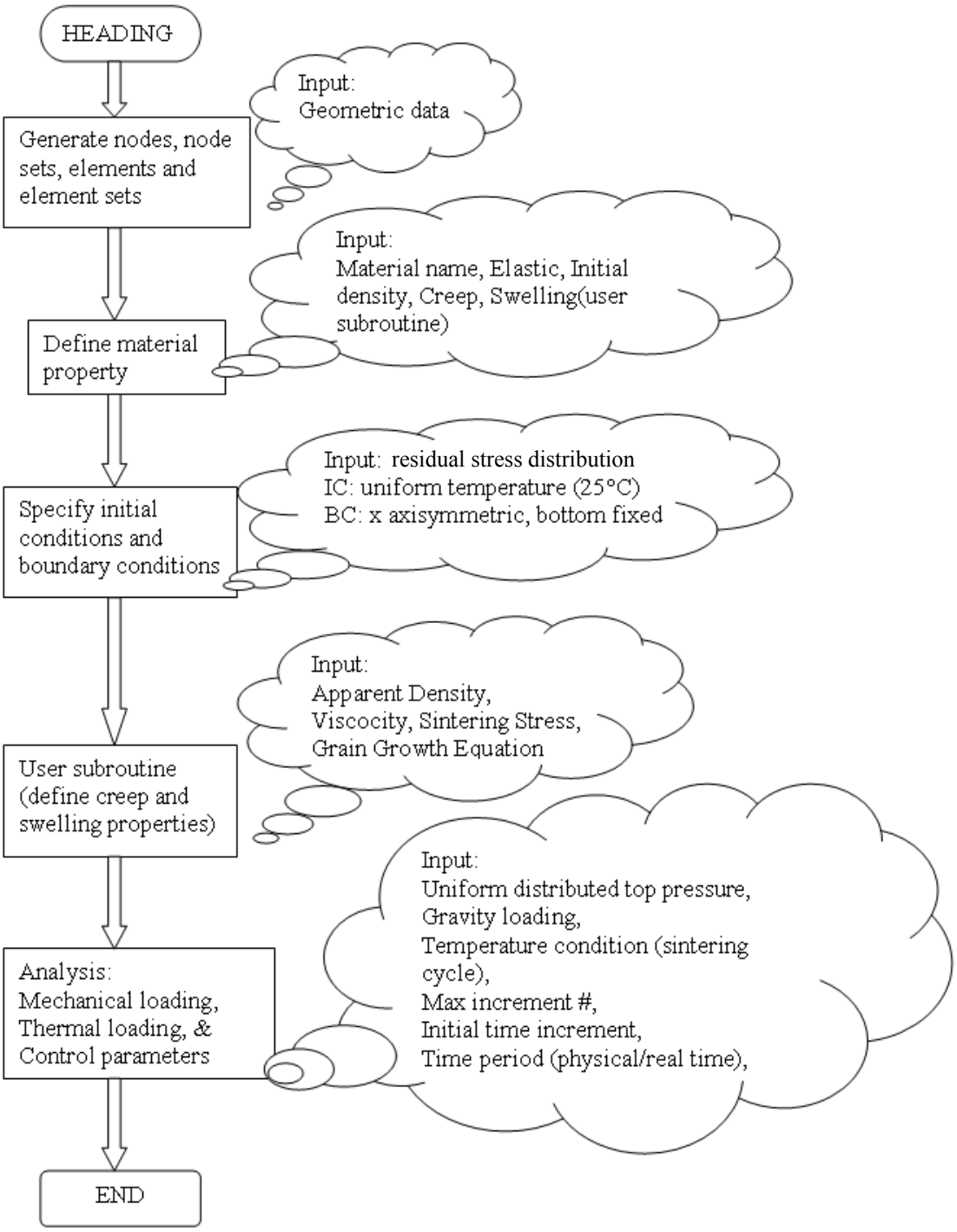

Fig. **4.5**: Flowchart of the Sintering Simulation Procedure in ABAQUS

Drucker-Prager/CAP model to establish the density field and residual stress field after compaction. Details on the compaction model for this specific material can be found in a previous study [44]. The parameters used in the CAP model and compaction simulation are listed in the Appendix D. Figure **4.6**a and Figure **4.6**b show the results of the distribution of relative density and residual stress from the compaction simulation and they are transferred into the sintering simulation as initial conditions.

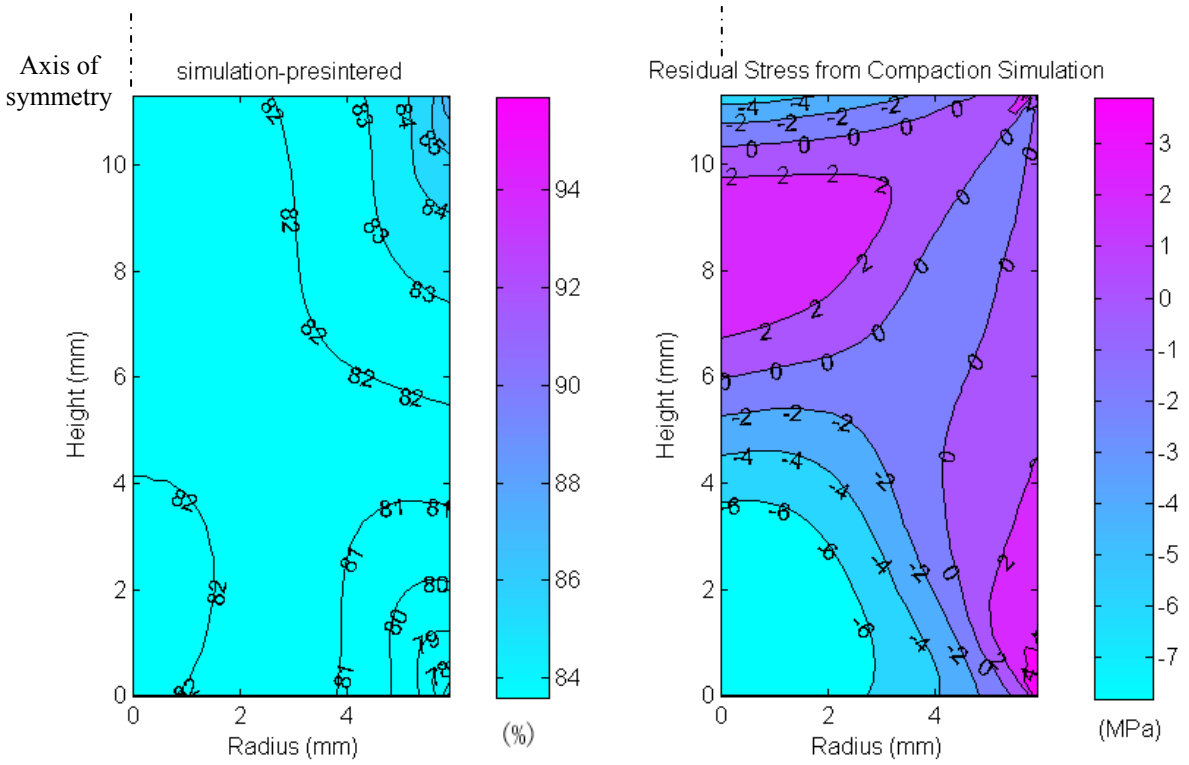

(a) Relative Density Contour (b) Residual Stress Contour

Fig. **4.6**: Initial Condition of Sintering Simulation from Compaction Simulation

The residual stress is applied to each element in the input file using command "*initial conditions, type=stress". Stress components read from the compaction simulation are written into the input file. The relative density is applied to each element in the CREEP subroutine, which is called at all integration points of elements at each

time increment. The density is redistributed to the integration points so as to fit the input format.

4.5.3 Determination of the Temperature Conditions—Heat Transfer Simulation

A quasi-static analysis with transient response is performed in the heat transfer analysis. It uses the same geometric model and element mesh as is used in the creep analysis. The sintering cycle has been applied as boundary conditions. The results of temperature field as a function of time and coordinates have been saved as history output data in the ABAQUS result file. They are subsequently transferred into the sintering analysis as prescribed thermal conditions. The parameters used in the heat transfer simulation are listed in the Appendix D.

4.5.4 Define the Creep Strain Rate in Creep Subroutine

In order to employ the constitutive law described in Chapter 2, the ABAQUS subroutine CREEP is used. For metals, this incremental creep strain routine allows swelling and creep as defined

$$\Delta\boldsymbol{\varepsilon}^{\mathrm{cr}} = \frac{1}{3}\Delta\bar{\varepsilon}^{\mathrm{sw}}\mathbf{R} + \Delta\bar{\varepsilon}^{\mathrm{cr}}\mathbf{n}, \qquad \text{Eq. } \mathbf{4.4}$$

where $\Delta\bar{\varepsilon}^{\mathrm{sw}}$ and $\Delta\bar{\varepsilon}^{\mathrm{cr}}$ are the incremental volumetric swelling strain and the uniaxial equivalent “creep” strain, respectively. They are defined by the user in the subroutine based on the creep model. For isotropic swelling **R** becomes the unit matrix **I.** The gradient of the deviatoric stress potential **n** is defined as

$$\mathbf{n} = \frac{\partial \tilde{q}}{\partial \boldsymbol{\sigma}} = \frac{3\boldsymbol{\sigma}'}{2\tilde{q}}, \qquad \text{Eq. } \mathbf{4.5}$$

where the deviatoric stress

$$\boldsymbol{\sigma}' = \boldsymbol{\sigma} + p\mathbf{I}, \qquad \text{Eq. } \mathbf{4.6}$$

and $p = -\frac{1}{3}\mathrm{tr}(\boldsymbol{\sigma})$ is the equivalent pressure stress (see Appendix C). The Mises equivalent deviatoric stress $\tilde{q}$ is given by

$$\tilde{q} = \sqrt{\frac{3}{2}\boldsymbol{\sigma}'\boldsymbol{\sigma}'}\ . \qquad \text{Eq. } \mathbf{4.7}$$

In this research, the creep rate equation (Equation **2.26**) is expressed as the incremental form of the creep strain rate

$$\Delta\boldsymbol{\varepsilon}^{cr} = \frac{tr(\boldsymbol{\sigma})\Delta t - 3\sigma_s \Delta t}{9\eta_b}\mathbf{I} + \frac{\boldsymbol{\sigma}'\Delta t}{2\eta_s}. \qquad \text{Eq. } \mathbf{4.8}$$

A comparison on Equation **4.4** and Equation **4.8** leads to the following relationships:

$$\frac{tr(\boldsymbol{\sigma})\Delta t - 3\sigma_s \Delta t}{9\eta_b}\mathbf{I} = \frac{1}{3}\Delta\bar{\varepsilon}^{sw}\mathbf{R}, \qquad \text{Eq. } \mathbf{4.9}$$

and

$$\frac{\boldsymbol{\sigma}'\Delta t}{2\eta_s} = \Delta\bar{\varepsilon}^{cr}\mathbf{n} = \Delta\bar{\varepsilon}^{cr}\frac{3\boldsymbol{\sigma}'}{2\tilde{q}}. \qquad \text{Eq. } \mathbf{4.10}$$

Therefore, the incremental volumetric swelling strain $\Delta\bar{\varepsilon}^{\mathrm{sw}}$ and the uniaxial equivalent "creep" strain $\Delta\bar{\varepsilon}^{\mathrm{cr}}$ can be written as

$$\Delta\bar{\varepsilon}^{sw} = \frac{tr(\boldsymbol{\sigma}) - 3\sigma_s}{3\eta_b}\Delta t = -\frac{p + \sigma_s}{\eta_b}\Delta t, \qquad \text{Eq. } \mathbf{4.11}$$

and

$$\Delta\bar{\varepsilon}^{cr} = \frac{\tilde{q}}{3\eta_s}\Delta t \,. \qquad \text{Eq. } \mathbf{4.12}$$

Note that the equivalent pressure stress p and the Mises equivalent deviatoric stress $\tilde{q}$ are internal variables in the CREEP subroutine. They are passed into the subroutine from the main program in every increment. The shear viscosity modulus η_s, the bulk viscosity modulus η_b, and the sintering stress σ_s are also defined in subroutines and all based on Equation **2.28** , Equation **2.29**, and Equation **2.34**, respectively. The sintering stress is applied in the CREEP subroutine, which is called at all integration points of elements at each time increment.

4.5.5 Usage of the Solution-Dependent State Variables

Sintering models are complex and it is beneficial to monitor certain variables throughout the simulation. Unlike other software, ABAQUS gives users the freedom to define solution-dependent state variables (SDV) in certain subroutines. In this research, several SDVs have been employed to help update the variables. For example, the grain size is stored in one of the SDVs so that it can be passed in every time the subroutine is called, thereby updating the current value. Other variables such as sintering stress, viscosity, and relative density are also stored as SDVs. At the end of the simulation, they can be used to analyze the model's behavior over time.

4.5.6 Results and Analysis

Results of axial shrinkage curves and relative density change during the sintering process are shown in this section, as well as some of the monitored variables.

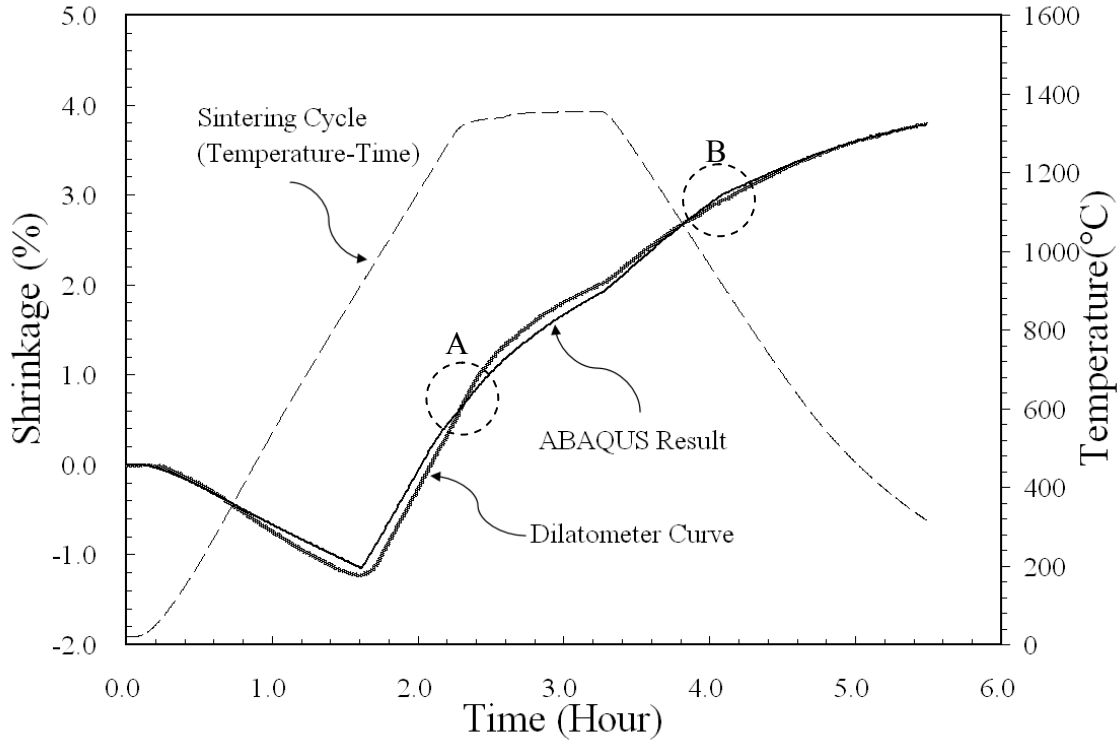

Fig. **4.7**: Comparison of the Axial Shrinkage Curves Measured in Dilatometer and Predicted by FEM model for Stainless Steel 316L Powder Compacts (83% dense) with Mean Particle Size of 33.4μm Sintered in Hydrogen at 10°C/min to 1350°C with 60-min Holding.

Figure **4.7** shows a very good match between the predicted and measured curves of axial shrinkage of 316L-S83 during sintering. Specifically the simulation curve shows the transition point when sintering stress (around 918°C) begins to dominate and thermal expansion effects are less pronounced. Subtle slope changes on the dilatometer curve are present in the simulation. For instance, the simulation captures the characteristics that in

region A (around 1200°C) the shrinkage rate starts to decrease with time, and in region B (around 900°C) another decrease of shrinkage rate. For example, region A is the place where the sintering stress starts to decrease because the activation energy for grain growth shifts to a lower level and the grain growth rate starts to increase. In region B, when the temperature falls below the transition temperature, the shrinkage stops and the thermal expansion is the only mechanism in the numerical model.

Figure **4.8** shows the predicted relative density change during sintering. It is clear that there is no density change when the process is only dominated by thermal expansion/contraction. The final density level reaches 94%.

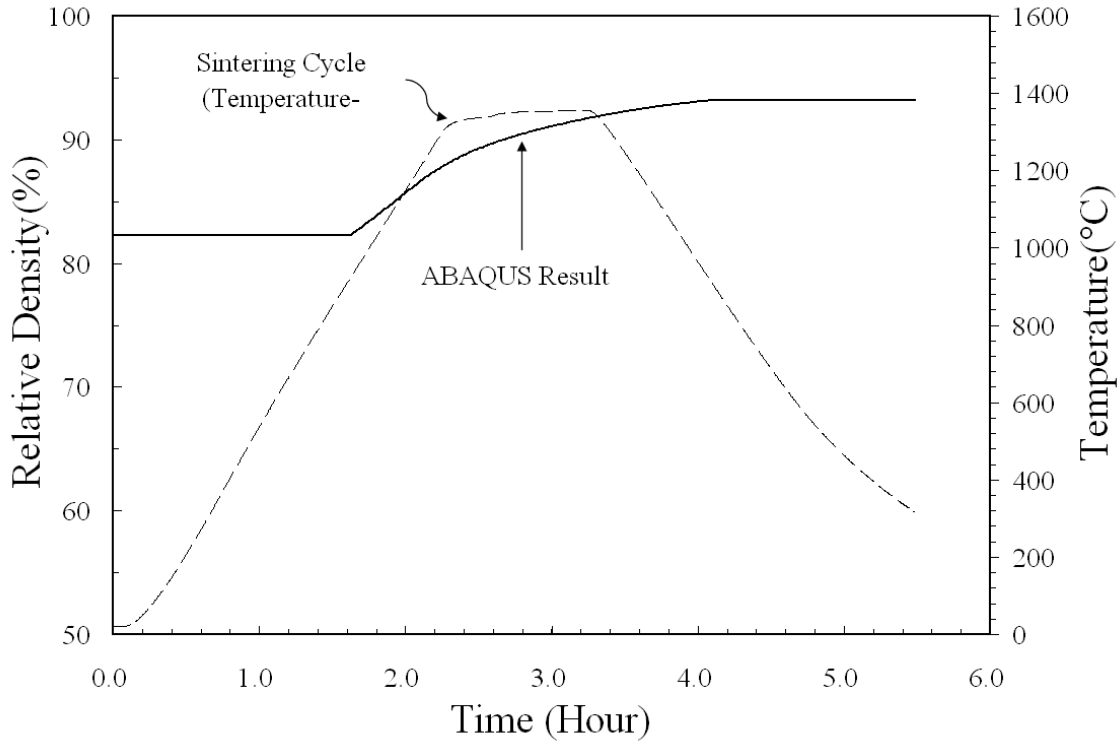

Fig. **4.8**: Relative Density Curves Predicted by FEM model for Stainless Steel 316L Powder Compacts (83% dense) with Mean Particle Size of 33.4μm Sintered in Hydrogen at 10°C/min to 1350°C with 60-min Holding.

Figure **4.9** shows the changes of the sintering driving force (sintering stress) and the material resistance (viscosity) in the sintering model. The sintering stress is zero when temperature is below the transition point (918°C for S83). In region A, the sintering stress rate increases with the increase of relative density until the transition temperature (1200°C) for grain growth is reached. It can be seen that the sintering stress is very sensitive to the change of grain size. Recall from the model that the sintering stress is proportional to the reciprocal of the grain size. Region B is in the cooling period, where the grain growth is assumed to be stopped. Therefore, the sintering stress is only affected by the slow increase of relative density until the temperature drops down to the transition point. Figure **4.9** also shows the viscosity curve in sintering. It can be seen that the Arrhenius type viscosity equation predicts a sudden and large decrease of viscosity when temperature increases as the material starts to behave like a viscous fluid.

As a comparison, similar simulations have been run for the other two groups of samples made from the powders with larger particle size: M83 and L83. The material parameters that are used for these models are listed in Appendix D. Figure **4.10** shows the comparison of axial shrinkage curves for all three groups. Samples made with powders with larger particle distributions exhibit smaller shrinkage. For each group, the predicted curves and the dilatometer test results are consistently good.

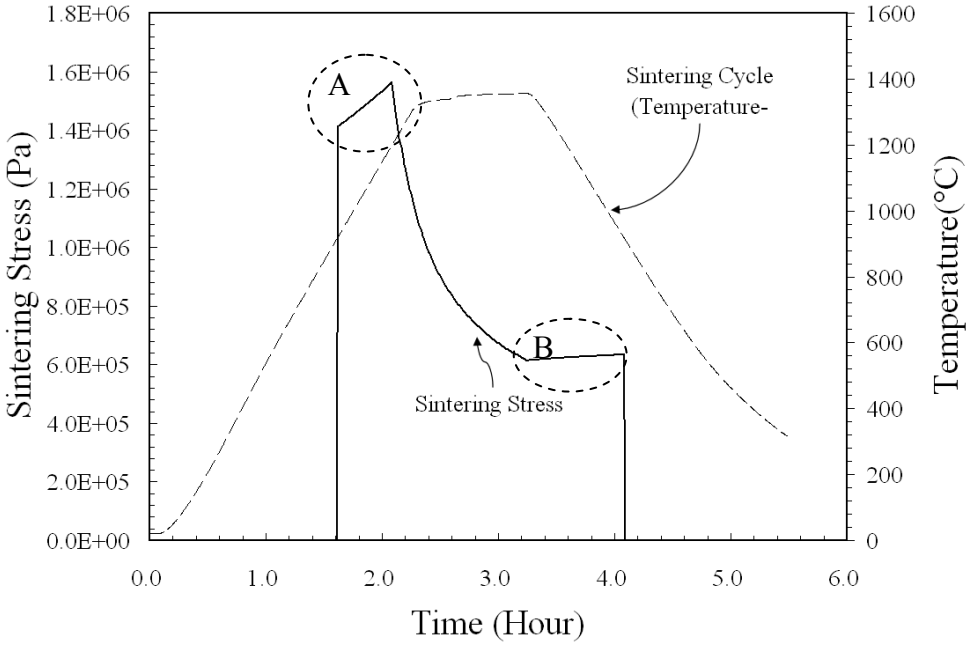

a. Sintering Stress

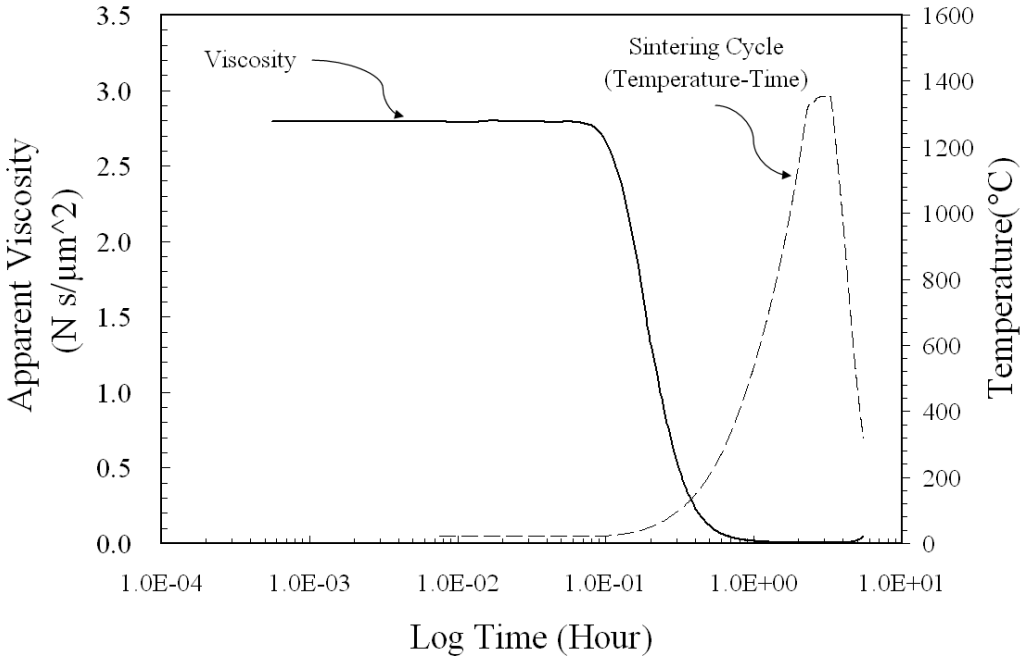

b. Apparent Viscosity

Fig. **4.9**: Sintering Stress and Apparent Viscosity Changes in the Sintering Model for Stainless Steel 316L Powder Compacts (83% dense) with Mean Particle Size of 33.4µm Sintered in Hydrogen at 10°C/min to 1350°C with 60-min Holding.

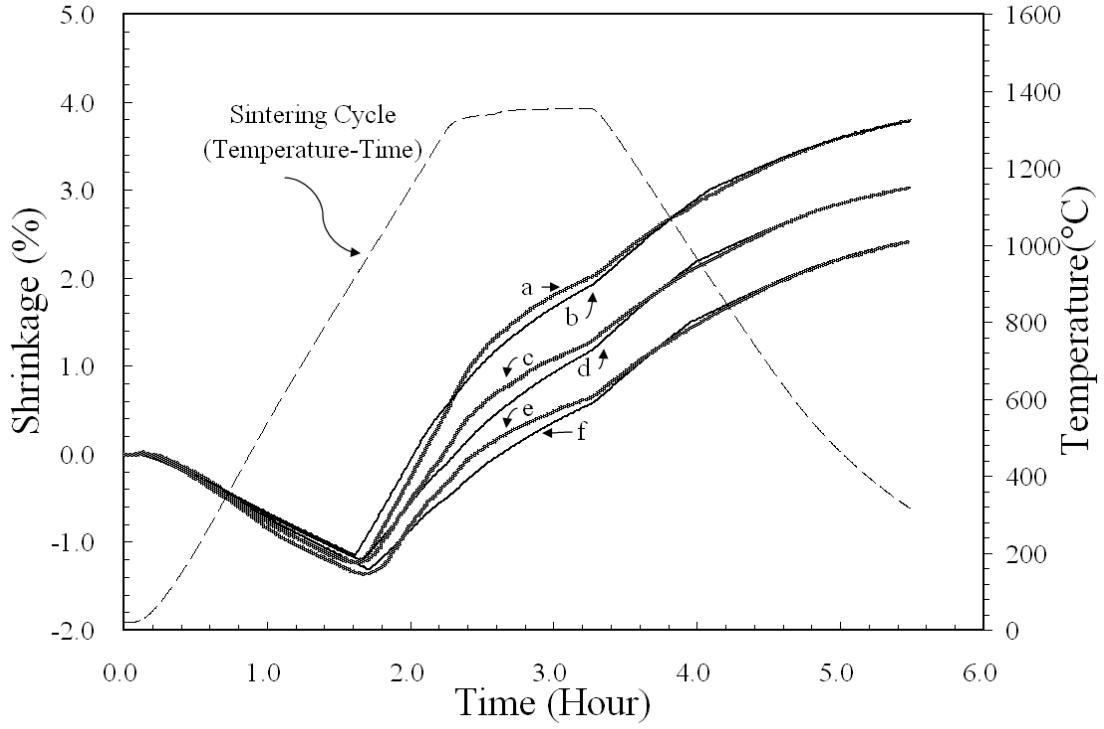

Fig. **4.10**: Comparison of Experiment Data and the ABAQUS Results for Dilatometry Plots of Shrinkage vs. Time: a. Measured Curve for S83; b. Predicted Curve for S83; c. Measured Curve for M83; d. Predicted Curve for M83; e. Measured Curve for L83; f. Predicted Curve for L83. (83% Compacted Stainless Steel 316L Compacts Heated at 10 °C/min to 1350°C, Held for One Hour, and Cooled at 10 °C/min to 300°C. Particle Mean Size: S83--33.4μm, M83--52.5μm, and L83--72.5μm)

It has been shown in **3.5.4** that the pre-exponential factor in the grain growth equation tends to converge to a constant after the time increment dt decreases to 30s. This conclusion helps determine the time increment in ABAQUS. Several trials have been run to check the effect of dt on the final result. It has been found that when dt is equal to or smaller than 30s, the results are almost the same. Figure **4.11** shows the difference of axial shrinkage curves when dt equals 30s, 300s, and 600s. The final grain size and the final shrinkage are almost the same. However, for the larger time increment, there is a

larger discrepancy during the heating period when the temperature is higher than the transition temperature and lower than the maximum (hold) temperature. Therefore, 30s is used as a suitable time increment length.

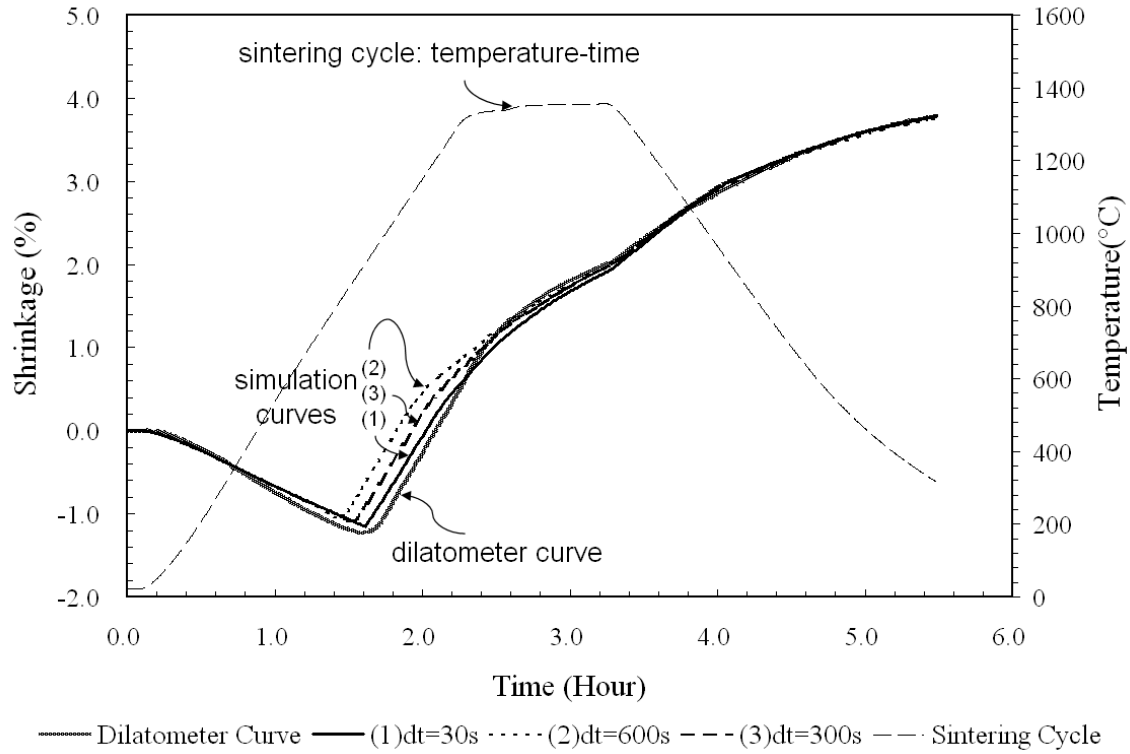

Fig. **4.11**: Effect of Time Increment dt on the Axial Shrinkage Curves (M83)

The density distribution of presintered and sintered 316L stainless steel compacts is measured by digital image analysis on the optical microscopes on a section of the cylindrical specimens. The final contour of density distribution is shown in Figure **4.12a**. Figure **4.12b** shows the contours of simulation results on density distribution by ABAQUS. Because the compaction was for a one-punch press, both contours show the maximum density at the up corner and the minimum at the lower corner. The sintered sample has higher bulk density.

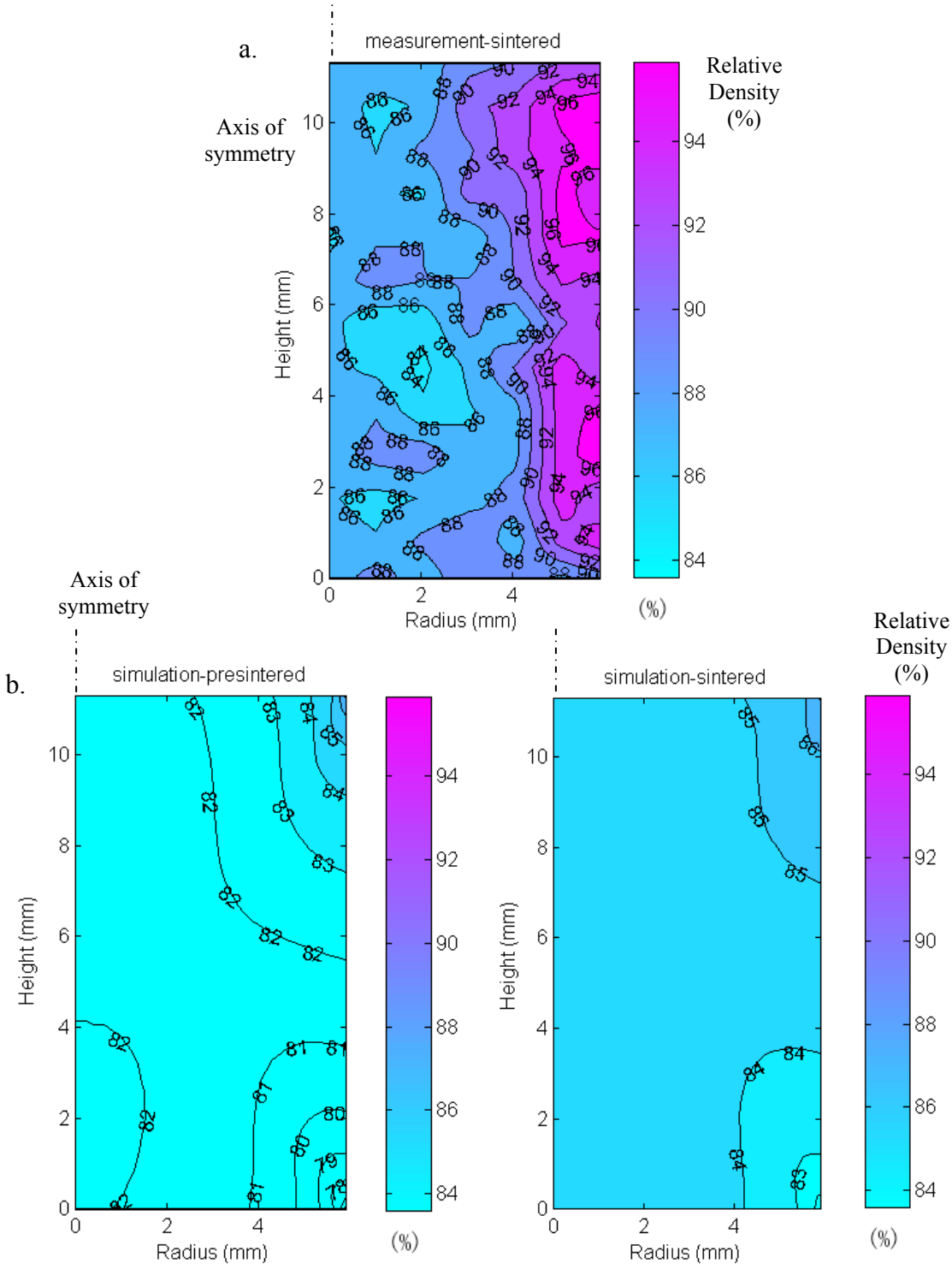

Fig. **4.12**: Comparison of the Measurement (a) and Simulation (b) of Density Distributions of Stainless Steel 316L Compact (M83, Heated at 10°C/min to 1350°C and Held for 1 Hour in Hydrogen)

The comparison of the simulation and the measurement shows that both patterns have large gradients near the edge and small gradient close to the center. According to the simulation results, a small amount of distortion has occurred at the up corner and the lower corner. This is because the density gradients are larger at the corners than at the center, and the low density area shrinks more than the high density area.

The model is dependent on the initial conditions and the level of refinement of the mesh. In order to determine the level of sensitivity to the initial density and residual stress variation, a study was conducted whereby the initial density was enforced to be uniformed distributed (82%) and the initial stress was enforced to be zero. For the case with uniform density distribution, the total axial shrinkage is about 20% smaller and the density distribution pattern is more uniform than the one with initial variations, though both shrinkage curves show similar trends. It is obvious to see that the initial density variation plays an important role in the simulation, especially the shape distortion prediction. The reason why the initial density variation is so important is because the sintering stress is directly related to the density.

For the case with zero initial stress, not much difference has been found between the one with and without initial stress variation. The residual stress calculated from the compaction simulation varies from -7.0 to 4.0 MPa, as shown in Fig. 4.6b; the sintering stress ranges from 0.0 to 1.6 MPa, as shown in Fig. 4.9a. Although they are at the same magnitude, it is found that the residual stress does not have a significant impact on the final shrinkage result due to the time-dependent nature of this problem. In other words, the shrinkage curves with and without the consideration of the initial residual stress look similar except the latter one has a little more expansion at the beginning when the

temperature is below the transition point. This is because over a five-hour long heat treatment the initial impact of the residual stress is insignificant for this material.

In addition, the refinement of finite element mesh has also been considered because it will affect the precision of the initial density distribution. A mesh with around 3000 elements has been used with the mesh size gradually decreasing as it gets closer to the corners. A coarser mesh tends to yield smaller shrinkage values. A finer mesh offered no significant change to the overall shrinkage results.

4.6 Summary

The viscoelasticity model developed in Chapter 2 is implemented in FEM software ABAQUS and an in-house code SinSolver. The empirical grain growth equation obtained in Chapter 3 is applied in association with the sintering stress model. The residual stress and density distribution results from the compaction simulation are transferred in the sintering simulation as initial conditions. An uncoupled heat transfer analysis yields temperature fields over time, which are used as temperature conditions in the sintering simulation.

The simulation results have good consistency with the measurement. An analysis on the plots of sintering stress and grain growth curve over time shows that the transition point for sintering stress and the transition temperature for grain growth have a critical influence on the simulation results. The model captures the overall trend of the axial shrinkage curve and several detail changes related to the shrinkage rate. The study on the particle size effect is performed by comparing the shrinkage curves of all the three

groups: S83, M83 and L83. All of the predicted curves match well with the dilatometer recorded data. It is found that the smaller particle size group has larger shrinkage. Density distribution results have also been compared with the measured density contours. Together, they provide the evidence to support where the distortion occurs.

SinSolver is proven to be a good supporting tool in the sintering simulation. It provides in depth understanding on the material model and helps check the parameters that are used in ABAQUS. However, due to its one-dimensional simplification, SinSolver shows less accuracy than ABAQUS.

Chapter 5

Conclusions and Suggestions

It has been shown in Chapter 4 that the sintering simulation model developed to include and employ the dominant mechanisms during sintering has a remarkable consistency with the experiment results for stainless steel 316L. The viscoelasticity model in association with the grain growth model shows great advantages in the prediction of the shrinkage in sintering dominated by grain boundary diffusion. Not only can the simulation predict the final shrinkage value, but it can describe the shrinkage behavior throughout the whole process. Based on the performance of the model, conclusions on this research are given and some suggestions on the future work are also included.

5.1 Conclusions

A viscoelasticity model that accounts for the microstructural level grain growth has been developed for the simulation of the thermal induced creep behavior in sintering. The model is based on the Maxwell model and considers thermal deformation as well. It has been implemented with the finite element method in ABAQUS and an in-house one-dimensional program named SinSolver. Both applications show accurate predictions for the axial shrinkage due to densification in sintering.

This research links the microscale evolution and the macroscale deformation via a phenomenological model of sintering stress, which accounts for the effects of grain size and porosity. A new concept of a transition temperature for the onset of sintering stress as a dominant factor has been proposed and successfully applied in the model. Material resistance to the creep deformation is deemed as a thermally activated process and an Arrhenius temperature relation has been employed to represent the apparent viscosity. Consistent with the other models, the inhomogeneous factors such as the initial density distribution and the residual stresses resulting from die compaction have been considered in the simulation.

Stainless steel 316L has been chosen as the primary material in this research due to its wide industrial application and representative sintering mechanism -- grain boundary diffusion. Metallographic study of the material's grain growth behavior yields insights about the simulation of grain growth for porous materials, and an intercept counting procedure based on the ASTM standard E112-96 has been developed for grain growth measurement. The resulting analysis quantifies the evolution of grain structures during a sintering cycle and verifies that a shift of the activation energy for grain growth occurs when the grain growth pattern changes from a faceted to a nonfaceted structure. The mean value has been used to represent the log-normal distribution of grain size and a curve fitting equation that can precisely describe the growth path is used to quantitatively represent the grain growth result. As a side benefit, the intercept counting procedure and the resulting analysis method, which account for the existence of pore area, have been an efficient tool that can provide more accurate results of grain size measurement of porous material than the other methods.

The predicted axial shrinkage curve shows a remarkable consistency with the dilatometer results. Comparisons between the simulation and experimental results in association with detailed analysis on the variables in the model helps to advance the understanding of the mechanisms that affect dimensional changes during sintering. Finally, simulation results of density distribution help predict the distorted shape.

5.2 Suggestions for Future Work

The viscoelasticity model has been shown to be effective for simulating the thermally induced creep analysis in sintering. The measurement of grain growth during sintering adds to the understanding of how grains evolve during sintering and how grain boundary diffusion can be implemented in a continuous model. However more research is needed to make the model more capable and applicable to a wider range of problems. Specifically, these efforts include

1. The viscosity moduli in this research are functions of porosity and apparent viscosity, which are functions of temperature. Viscosity represents the material resistance to deformation. It is commonly known that the material strength is related to the microstructure of the material. Therefore, it is possible that the viscosity change in sintering could be related to reasons other than thermal factors such as microstructure evolution. Further research work is suggested on the study of the relation between viscosity and the microstructure change.

2. The transition temperature for sintering stress is one of the ways to represent the sudden increase of the shrinkage rate. Other approaches should be tested in the future. For example, the phenomenon can be explained by an activation energy change and incorporated via the viscosity model.
3. Both materials studied in this research have only one recommended sintering cycle. It is suggested that different sintering recipes should be tried so as to study the influence of heating rate on the densification in sintering.
4. A greater variety of tests can be conducted for model characterization. In particular, material with relatively large densification should be used so as to study the model's performance on predicting distortion.
5. Based on the one-dimensional problem solved in SinSolver and the two-dimensional ABAQUS analysis, three-dimensional applications with complex geometric shapes should be studied using the same viscoelasticity model with grain growth evolution. SinSolver is proven to be an efficient supporting tool for ABAQUS in this research. It has more flexibility and efficiency when solving sintering problems. Future work is suggested to expand its capability to two or three dimensions.
6. The intercept counting method developed for grain size measurement in the porous body is proven to be efficient and accurate. In this research, the in-house programs developed for the measurement procedure can be applied to other metallographic work. Efforts are suggested to make the program more applicable.

Bibliography

1. German, R. M. (1994). *Powder Metallurgy Science*, (2nd ed.). Metal Powder Industries Federation, Princeton, New Jersey.

2. Ashby, M. F. (1974). A First Report on Sintering Diagrams. *Acta Metallurgica,* 22: 275-289.

3. German, R. M. (1996). *Sintering Theory and Practice*. John Wiley & Sons, Inc., New York, NY.

4. Keller, J. M., French, J. D., et al.(1998). Industry, Goverment Team to Improve Ceramic Manufacturing. *The American Ceramic Society Bulletin*. October 1998, pp.52-56.

5. Frenkel, J. (1945). Viscous flow of Crystalline Bodies under the Action of Surface Tension. *Journal of Physics,* 9(5): 385-91.

6. Herring, C. (1951). Surface Tension as a Motivation for Sintering. *The Physics of Powder Metallurgy*. W. E. Kingston. New York, McGraw-Hill, pp.143-79.

7. Swinkels, F. B. and Ashby, M. F. (1981). A Second Report on Sintering Diagrams. *Acta Metallurgica,* 29: 259-281.

8. Hsueh, C. H., Evans, A. G., and Coble, R. L. (1982). Microstructure Development during Final/Intermediate Stage Sintering-I. Pore/Grain Boundary Separation. *Acta Metallurgica,* 30: 1269-1279.

9. Spears, M. A., Evans, A. G. (1982). Microstructure Development during Final/Intermediate Stage Sintering-II. Grain and Pore Coarsening. *Acta Metallurgica,* 30: 1281-1289.

10. Olevsky, E. A. (2002). Modeling of Sintering: Challenges and Further Development. *International Conference on Process Modeling in Powder Metallurgy & Particulate Materials*, Metal Powder Industries Federation, Princeton, New Jersey.

11. Riedel, H. (1990). A Constitutive Model for the Finite-element Simulation of Sintering-Distortions and Stresses. *Ceramic Powder Science* III. pp.619-630.

12. Skorohod, V. V., Olevsky, E. A., Shtern, M. B. (1991). Continuum Theory for Sintering of Porous Bodies: Model and Application. *Science of Sintering* 23(2): 79-91.

13. Hansen, J. D., Rusin, R. P., Teng, M.-H., and Johnson, D. L. (1992). Combined-Stage Sintering Model. *Journal of the American Ceramic Society,* 75(5): 1129-1135.

14. Cocks, A. C. F. (1994). The Structure of Constitutive Laws for the Sintering of Fine Grained Materials. *Acta Metallurgica*, 42: 2191-2210.

15. Kwon, Y. S., Kim, K. T. (1996). High Temperature Densification Forming of Alumina Powder-Constitutive Model and Experiments. *Journal of Engineering Materials and Technology,* 118: 448-455.

16. Sun, D. - Z., Riedel, H. (1995). Prediction of Shape Distortions of Hard Metal Parts by Numerical Simulation of Pressing and Sintering. *Simulation of Materials Processing: Theory, Methods and Applications*, Shen & Dawson (eds). pp. 881-886.

17. Dehoff, R. T. (1984). A Cell Model for Microstructural Evolution during Sintering. *The Sixth International Conference on Sintering and Related Phenomena*, University of Notre Dame, Plenum Press, NewYork.

18. Kwon, Y. S., Chung, S. H., Ahn, H. K., Chung, S. T., Park, S. J., and Yoon, D. T.-S. (2001). CAE Analysis for Sintering Stage of Powder Injection Molding. *Proceedings for 2001 International Conference on Powder Metallurgy & Particulate Materials*, Metal Powder Industries Federation, Princeton, New Jersey.

19. Lame, O., Bouvard, D., Wiedemann, H. (2001). Anisotropic Shrinkage and Gravity-Induced Creep during Sintering. *Powder Metallurgy*, 45(2):181-185.

20. Olevsky, E. A. (1998). Reports: A Review Journal, Theory of Sintering: From Discrete to Continuum. *Materials Science and Engineering,* R23: 41-100.

21. Shinagawa, K. (1996). Finite Element Simulation of Sintering Process (Microscopic Modelling of Powder Compacts and Constitutive Equation for Sintering). *JSME International Journal*, Series A, 39(4):565-572.

22. Kellett, B. J., Lange, F. F. (1989). Thermodynamics of Densification: I, Sintering of Simple Particle Arrays, Equilibrium Configurations, Pore Stability, and Shrinkage. *Journal of the American Ceramic Society,* 72(5): 725-734.

23. Du, Z. - Z., Cocks, A. C. F. (1992). Constitutive Models for the Sintering of Ceramic Components-I. Material Models. *Acta Metallurgica,* 40(8): 1969-1979.

24. Svoboda, J., Riedel, H., Zipse, H. (1994). Equilibrium Pore Surfaces, Sintering Stresses and Constitutive Equations for the Intermediate and Late Stages of

Sintering-I. Computation of Equilibrium Surfaces. *Acta Metallurgica,* 42(2): 435-443.

25. Lam, D. C. C. (1999). Densification Model for Powder Compacts. *Journal of Materials Science,* 34: 5879-5884.

26. Jonghe, L. C. De, Rahaman, M.N. (1988). Sintering Stress of Homogeneous and Heterogeneous Powder Compacts, *Acta Metallurgica*, 36(1):223-229.

27. Gillia, O. and Bouvard, D. (2000). Phenomenological Analysis of Densification Kinetics during Sintering: Application to WC-Co Mixture. *Materials Science & Engineering,* A279: 185-191.

28. Gillia, O., Josserond, C., and Bouvard, D. (2001). Viscosity of WC-Co Compacts during Sintering. *Acta Metallurgica*, 49: 1413-1420.

29. ASM, (1982) Stainless Steel AISI Type 316, *Engineering Properties of Steel*, ASM, pp. 292-293.

30. Bocchini, G. F., Rivolta, B., Silva, G. (2002). Thermal expansion of P/M Ferrous Materials. *The International Journal of Powder Metallurgy,* 38(7): 54-61.

31. Choi, J. S. and Yoon, D. Y. (2001). The Temperature Dependence of Abnormal Grain Growth and Grain Boundary Faceting in 316L Stainless Steel. *ISIJ International*, 41(5): 478-483.

32. Lee, S. B., Hwang, N. M., Yoon, D. Y., and Fenry, M. F. (2000). Grain Boundary Faceting and Abnormal Grain Growth in Nickel. *Metallurgical and Materials Transactions A*, 31A(3A): 985-994.

33. Lee, S.-H., Choi, J. S., and Yoon, D. Y. (2001). The Dependence of Abnormal Grain Growth on Initial Grain Size in 316L Stainless Steel. *Z. Metallkd.*, 92(7): 655-662.

34. Kashyap, B. P. and Tangri, K. (1992). Grain Growth Behaviour of Type 316L Stainless Steel. *Materials Science & Engineering A: Structural Materials: Properties, Microstructure and Processing,* A149(2): L13-L16.

35. German, R. M. (1978). Grain Growth in Austenitic Stainless Steels. *Metallography,* 11:235-239.

36. Cho, J. R., Jeong, H. S., Cha, D.J., Bae, W.B., Hartley, P., Pillinger, I. (2001) Prediction of Microstructural Evolution and Recrystallization Behaviors of Die Steel. *Simulation of Materials Processing: Theory, Methods and Applications*, Mori Ed., Swets & Zeitlinger, Lisse.

37. Liu, X.-L., He, J.-P., Dong, Q.-F., and Zhou, S.-Z. (2001). A Study of Grain Growth Kinetics in Sintered NdFeB Magnets. *Journal of Rare Earths,* 19(3): 209-214.

38. Ashby, M. F. and Easterling, K. E. (1982). A First Report on Diagrams for Grain Growth in Welds. *Acta Metallurgica,* 30(11-a): 1969-1978.

39. Chidiac, S. E., Wilkinson, D. S., and Mirza, F. A. (1992). Finite-element Modeling of Transient Heat-transfer and Microstructural Evolution in Welds: Part II. Modeling of Grain-growth in Austenitic Stainless-steels. *Metallurgical Transactions B-Process Metallurgy,* 23b(6): 841-845.

40. Smolej, V. (2001). Image Analysis for Materials Testing. *Industrial Heating,* June 2001, LXVIII: 55-57.

41. Tewari, A. and Gokhale, A. M. (2000). Application of Three-Dimensional Digital Image Processing for Reconstruction of Microstructural Volume from Serial Sections. *Materials Characterization*, 44: 259-269.

42. Tewari, A. and Gokhale, A. M. (2001). Estimation of Three-Dimensional Grain Size Distribution from Microstructural Serial Sections. *Materials Characterization*, 46: 329-335.

43. ASTM (2000). ASTM Standard E112-96: Standard Test Methods for Determining Average Grain Size. *Annual Book of ASTM Standards 2000*. ASTM International. 03.01: 267-292.

44. He, Y., Engel, R. S., Salamon, N. J., and Zhang, R. (2002). Sensitivity Study and Parameter Determination for 316L Stainless Steel Powder Die Compaction. *Proceedings of the 2002 International Conference on Process Modeling in Powder Metallurgy & Particulate Materials*, Lawley, Smugeresky and L. Smith (eds.), Metal Powder Industries Federation, Princeton, New Jersey.

45. Voort, G. V. (1991). Committee E-4 and Grain Size Measurements: 75 years of progress. *ASTM Standardization News*, May, 1991.

46. ASM (1990). Metallography and Microstructures. ASM Handbook.

47. Voort, G. F. V. (1984). *Metallography Principles and Practice*. McGraw-Hill, Inc., New York, NY.

48. Mistler,R. E., Coble, R. L. (1974). Grain-Boundary Diffusion and Boundary Widths in Metals and Ceramics. *Journal of Applied Physics,* 45(4): 1507-1509.

49. Hassold, G. N., Chen, I.-W., Srolovitz, D. J. (1990). Computer Simulation of Final-Stage Sintering: I, Model, Kinetics, and Microstructure. *Journal of the American Ceramic Society,* 73(10): 2857-2864.

50. Chen, I.-W., Hassold, G. N., Srolovitz, D. J. (1990). Computer Simulation of Final-Stage Sintering: II, Influence of Initial Pore Size. *Journal of the American Ceramic Society,* 73(10): 2865-2872.

51. Matsubara, H. (1999). Computer Simulations for the Design of Microstructural Developments in Ceramics. *Computational Materials Science*, 14:125-128.

52. Mizera, J., Wyrzykowski J. W., and Kurzydlowski, K. J. (1988). Description of the Kinetics of Normal and Abnormal Grain Growth in Austenitic Stainless Steel. *Materials Science & Engineering A: Structural Materials: Properties, Microstructure and Processing,* A104: 157-162.

53. Wilkinson, D. S., Cáceres, C. H. (1984). On the Mechanism of Strain-Enhanced Grain Growth During Superplastic Deformation. *Acta Metallurgica*, 32: 1335-1345.

54. Bennison, S. J., Harmer, M. P. (1985). Grain-Growth Kinetics for Alumina in the Absence of a Liquid Phase. *Journal of the American Ceramic Society,* 68(1): C-22-C24.

55. Chokshi, A. H., Porter, J. R. (1986). Analysis of Concurrent Grain Growth during Creep of Polycrystalline Alumina. *Journal of the American Ceramic Society,* 69(2): C37-C39.

56. Atkinson, H. V. (1988). Theories of Normal Grain Growth in Pure Single Phase Systems. *Acta Metallurgica*, 36(3): 469-491.

57. Rödel, J., Glaeser, A. M. (1990). Anisotropy of Grain Growth in Alumina. *Journal of the American Ceramic Society,* 73(11): 3292-3301.

58. German, R. M. (1997). Supersolidus Liquid-Phase Sintering of Prealloyed Powders. *Metallurgical and Materials Transactions A,* 28A: 1553-1567.

59. Riedel, H., and Sun, D.-Z. (1992). Simulation of die pressing and sintering of powder metals, hard metals. *Numerical Methods in Industrial Forming Processes*. Chenot, Wood & Zienkiewicz (eds), pp.883-886.

60. Riedel, H., Kozak, V., Svoboda, J. (1994). Densification and Creep in the Final Stage of Sintering. *Acta Metallurgica,* 42(9):3093-3103.

61. Riedel, H. (1997). Pressing and Sintering in Powder Technology. *Plansee Proceedings-14th International Plansee Seminar '97*, Reutte/Tirol/Austria, 4: 233-244.

62. Kraft, T., Riedel, H. (2002). Numerical Simulation of Die Compaction and Sintering. *Powder Metallurgy*, 45(3): 227-231.

63. Shinagawa, K. (1999). Micromechanical Modelling of Viscous Sintering and a Constitutive Equation with Sintering Stress. *Computational Materials Science*, 13:276-285.

64. Darcovich, K., Shinagawa, K., Walkowiak, F. (2004). A Three-dimensional Dual-Mechanism Model of Pore Stability in a Sintering Alumina Structure. *Materials Science and Engineering*, A 373:107-114.

65. Mähler, L., Runesson, K. (2000). Modelling of Solid-phase Sintering of Hardmetal Using a Mesomechanics Approach. *Mechanics of Cohensive-Frictional Materials*. 5:653-671.

66. Mähler, L., Ekh, M., Runesson, K. (2001). A Class of Thermo-hyperelastic-viscoplastic Models for Porous Materials: Theory and Numerics. *International Journal of Plasticity*. 17:943-969.

67. Mori, K., Osakada, K., Miyazaki, M. (1997). Predication of Fracture in Sintering of Ceramic Powder Compact. *International Journal of Machine Tools & Manufacture*, 37(9):1327-1336.

68. Mori, K., Matsubara, H., Umeda, M. (2001). Finite Element Simulation of Sintering of Powder Compact Using Shrinkage Curve Obtained by Monte Carlo Method, *Simulation of Materials Processing: Theory, Methods and Applications*, A. A. Balkema, Exton, PA.

69. Shimizu, M., Nomura, H., Matsubara, H., Mori, K. (2001). 3D Simulations of Sintering and Grain Growth by the Monte Carlo Method, *Simulation of Materials Processing: Theory, Methods and Applications*, A. A. Balkema, Exton, PA.

70. Mori, K., Matsubara, H., Noguchi, N. (2004). Micro-Macro Simulation of Sintering Process by Coupling Monte Carlo and Finite Element Methods. *International Journal of Mechanical Sciences*, 46:841-854.

71. Brandes, E. A. (1983). *Smithells Metals Reference Book*, 6th ed., Butterworth and Co., London.

Appendix A

MATLAB Codes for Intercept Count Procedure

A.1 Generation of Test Pattern with 3 Concentric Circles

```
%%%[c3maker.m] start%%%
%--------------------------------------------------------------------------
%Copyright Rui Zhang @ PennState
%contact:<zruier@gmail.com>
%   November, 2004
%--------------------------------------------------------------------------

clear all; close all;
ver=1024; hor=1280;
center=[ver/2 hor/2];
radius1=.93*ver/2;radius2=2/3*radius1;radius3=1/3*radius1;
background=ones(1024, 1280, 3);
thick=1;
%thick is the parameter to control the width of the circle
%it equals to 1 for measurement; set it to 3 for images used in thesis

% plot 3 concentrated circles
[beta1,c1]=circle3(center,radius1,thick);
[beta2,c2]=circle3(center,radius2,thick);
[beta3,c3]=circle3(center,radius3,thick);

[M1 N1]=size(c1);[M2 N2]=size(c2);[M3 N3]=size(c3);
for i=1:M1
   background(c1(i,1),c1(i,2),:)=0;
   background(c1(i,1),c1(i,2),3)=1;
end
for i=1:M2
   background(c2(i,1),c2(i,2),:)=0;
   background(c2(i,1),c2(i,2),3)=1;
end
for i=1:M3
   background(c3(i,1),c3(i,2),:)=0;
   background(c3(i,1),c3(i,2),3)=1;
end

% set the center as a locator
background(ver/2,hor/2,:)=0;
background(ver/2,hor/2,3)=1;

imwrite(background, '3concircles.tif','tif');
save cc3 beta1 c1 beta2 c2 beta3 c3;
```

```
%%%[c3maker.m] end%%%

%%%[circle3.m] start%%%
function [beta, rcir]=circle3(center,radius,thick)
%--------------------------------------------------------------------------
% This subroutine output a matrix RCIR, which contains
% the sorted coordinates of all the points on a circle with
% center defined as a vector CENTER, radius as a
% scaler RADIS.
%
%   Usage Example,
%   H=circle3([1,3],3,1);
%
%   Rui Zhang <zruier@gmail.com>
%   November, 2004
%--------------------------------------------------------------------------

Dis=zeros(2*center(1),2*center(2));k=0;
er=thick*sqrt(2)/2;
%find out all the pts on the circle
for i=1:2*center(1)
   for j=1:2*center(2)
      Dis(i,j)=sqrt((i-center(1))^2+(j-center(2))^2);
      d=abs(Dis(i,j)-radius);
      if (d<=er)
         k=k+1;cir(k,1)=i;cir(k,2)=j;
      end
   end
end
%sort the pts by angle
[K L]=size(cir);
for i=1:K
   theta(i)=atan2((cir(i,2)-center(2)),(cir(i,1)-center(1)));
end
[beta,IX]=sort(theta);
%re-order the circle pts
for i=1:K
   rcir(i,:)=cir(IX(i),:);
end
%%%[circle3.m] end%%%
```

A.2 Intercept Counting

```
%%%[main.m] start%%%
%--------------------------------------------------------------------------
% This is the main code for intercept count procedure.
% It calls subroutines: analyst.m, histogram.m
%   Rui Zhang <zruier@gmail.com>
%   Version 1.00
%   December, 2004
%--------------------------------------------------------------------------
```

```
clear all; close all;clc
ver=1024; hor=1280;center=[ver/2 hor/2];
%read the modified pattern file
img=imread('..\results\pattern\M79\M79_1350_1_500x_12_pattern.tif');
load cc3 beta1 c1 beta2 c2 beta3 c3;%c3->coarse
radius1=.93*ver/2;radius2=2/3*radius1;radius3=1/3*radius1;
%scale unit:micron/pixel
ratio1000x10=.08547;
ratio1000x20=.08547;
ratio500x50=.1748;
ratio200x100=.4329;
%ratio=ratio1000x10;
%ratio=ratio1000x20;
ratio=ratio500x50;
%ratio=ratio200x100;

% counting
[grainlen1,porelen1,porelenraw1]=analyst(img,beta1,c1,radius1,ratio);
[grainlen2,porelen2,porelenraw2]=analyst(img,beta2,c2,radius2,ratio);
[grainlen3,porelen3,porelenraw3]=analyst(img,beta3,c3,radius3,ratio);

% summing up data from 3 circles
[m1 n1]=size(grainlen1);grainlen(1:m1)=grainlen1;
[m2 n2]=size(grainlen2);grainlen(m1+1:m1+m2)=grainlen2;
[m3 n3]=size(grainlen3);grainlen(m1+m2+1:m1+m2+m3)=grainlen3;

[m1 n1]=size(porelen1);porelen(1:m1)=porelen1;
[m2 n2]=size(porelen2);porelen(m1+1:m1+m2)=porelen2;
[m3 n3]=size(porelen3);porelen(m1+m2+1:m1+m2+m3)=porelen3;

[m1 n1]=size(porelenraw1);porelenraw(1:m1)=porelenraw1;
[m2 n2]=size(porelenraw2);porelenraw(m1+1:m1+m2)=porelenraw2;
[m3 n3]=size(porelenraw3);porelenraw(m1+m2+1:m1+m2+m3)=porelenraw3;

% postprocess
[gmean gmode gtrimean g25 g50 g75 ggray gculper ginper]=histogram(grainlen);
[pmean pmode ptrimean p25 p50 p75 pgray pculper pinper]=histogram(porelen);
grainlen=grainlen';porelen=porelen';

%export
save ..\results\data\M79\M79_1350_1_500x_12_grain.txt grainlen -ASCII
save ..\results\data\M79\M79_1350_1_500x_12_pore.txt porelen -ASCII

disp('arithmetic average grain intercept length (mean):');disp(gmean);
disp('most frequent grain intercept length (mode):');disp(gmode);
disp('trimean of grain intercept length (trimean):');disp(gtrimean);
disp('arithmetic average pore intercept length (mean):');disp(pmean);
disp('most frequent pore intercept length (mode):');disp(pmode);
disp('trimean of pore intercept length (trimean):');disp(ptrimean);
disp('number of intercepts in grain area:');
[m n]=size(grainlen);disp(m);
disp('number of intercepts in pore area:');
[m n]=size(porelen);disp(m);
disp('25% 50% 75% of grain size');disp(g25);disp(g50);disp(g75);
```

```
%checking
%difference between the circum counted and the real sum of 3 circles
tc=(radius1+radius2+radius3)*2*pi*ratio;%total circum
cc=sum(grainlen1)+sum(porelen1)+...
   sum(grainlen2)+sum(porelen2)+...
   sum(grainlen3)+sum(porelen3);%counted circum
disp('difference between counted circum and real circum(%):')
dif=100*abs(tc-cc)/tc;disp(dif);

%percentage of total GB width in total length of intercepts
a=sum(porelenraw1)-sum(porelen1)+...
   sum(porelenraw2)-sum(porelen2)+...
   sum(porelenraw3)-sum(porelen3);%total GBwidth
b=sum(grainlen1)+sum(grainlen2)+sum(grainlen3);%total Grain
disp('max error=GBwidth/(GBwidth+Grain) (%):');
c=100*a/(a+b);
disp(c);
%%%[main.m] end%%%

%%%[analyst.m] start%%%
function [grainlen,porelen,porelenraw]=...
   analyst(img,beta,coarse,radius,ratio);
%--------------------------------------------------------------------------
% This subroutine count the intercepts and pores.
% include subrountines: intercept.m
% *plotting gray intensity disable
%
%   Rui Zhang <zruier@gmail.com>
%   Version 1.00
%   December, 2004
%--------------------------------------------------------------------------
[M N]=size(coarse);
% convert the gray intensity to either 106 or 255
for i=1:M
   gray(i)=img(coarse(i,1),coarse(i,2));%106,60,255
   if (gray(i) ~= 255)
      gray(i)=106;
   end
end

% count the intercepts by using 2 filters:[106 255]&[255 106]
[grainlenraw,porelenraw]=intercept(beta,gray,radius);
%reduce the error due to 3-pixel eraser(see log.txt)
grainlen=grainlenraw+3.0;
%determine how many pores in porelen
[m1 n1]=size(porelenraw');pmax=3.0*sqrt(2);c=0;
for i=1:m1
   if (porelenraw(i) >= pmax)
      c=c+1;porelen(c)=porelenraw(i);
   end
end

% convert pixel to micron
```

```
grainlen=ratio*grainlen';
porelen=ratio*porelen';
porelenraw=ratio*porelenraw';
%%%[analyst.m] end%%%

%%%[histogram.m] start%%%
function [avg mode trimean t25 t50 t75 gray culper inper]=histogram(grainlen)
%--------------------------------------------------------------------------
% This subroutine draws the intercept length histogram.
% output 'gray' is the sorted grayintensity groups
%
%   Rui Zhang <zruier@gmail.com>
%   Version 1.00
%   December, 2004
%--------------------------------------------------------------------------
avg=mean(grainlen);[m,n]=size(grainlen');
gmax=max(grainlen);gmin=min(grainlen);
N=ceil(gmax);
s=(gmax-gmin)/N;
culmulate=zeros(N+1,1);individual=zeros(N+1,1);
percent1=culmulate;percent2=individual;
gray(1)=gmin;culmulate(1)=0;individual(1)=0;
for n=2:N+1
   gray(n)=gmin+(n-1)*s;
   for i=1:m
      if (grainlen(i)<=gray(n))
         culmulate(n)=culmulate(n)+1;
         if (grainlen(i)>=gray(n-1))
            individual(n)=individual(n)+1;
         end
      end
   end
end
percent1(:)=100*culmulate/m;
percent2(:)=100*individual/m;
%search for most frequent gray level
for m=1:N+1
   if (percent2(m)==max(percent2))
      mode=gray(m);break;
   end
end

%calculate trimean
for m=1:N+1
   if (percent1(m)>= 25)
      t25=gray(m);
      a=percent1(m)-25;b=25-percent1(m-1);
      if (a>=b)
         t25=gray(m-1);
      end
      break;
   end
end
for m=1:N+1
```

```
   if (percent1(m)>= 50)
      t50=gray(m);
      a=percent1(m)-50;b=50-percent1(m-1);
      if (a>=b)
         t50=gray(m-1);
      end
      break;
   end
end
for m=1:N+1
   if (percent1(m)>= 75)
      t75=gray(m);
      a=percent1(m)-75;b=75-percent1(m-1);
      if (a>=b)
         t75=gray(m-1);
      end
      break;
   end
end
trimean=(t25+2*t50+t75)/4;

culper=percent1;inper=percent2;
%draw the curves in the same figure using different y axis
%figure;hold on;
%line(gray,percent1,'Color','b','LineStyle','-.');%xlim([0 255]);
%ylabel('culmulated percent of indicated length','FontSize',16);
%legend('culmulated');
%ax1=gca;set(ax1,'YColor','b');
%ax2 = axes('Position',get(ax1,'Position'),...
%          'YAxisLocation','right',...
%          'Color','none',...
%          'YColor','r');
%line(gray,percent2,'Color','r','LineStyle','-');%xlim([0 255]);
%ylabel('individual percent of indicated length','FontSize',16);
%xlabel('intercept length (\mu m)','FontSize',20);
%legend('individual');
figure;
bar(gray,percent2);hold on;
b=round(max(percent2)+1);B=[0 b];
A1=[avg avg];A2=[mode mode];A3=[trimean trimean];
plot(A1,B,'r--',A2,B,'g:',A3,B,'b-');ylim([0 b]);xlim([0 round(max(gray)+1)]);
%dashed,dotted,solid
ylabel('frequency (%)','FontSize',20);
xlabel('intercept length (\mu m)','FontSize',20);
legend('histogram','mean','mode','trimean');
%title('fig.09 histogram of grain size distribution in ss316L sintered at 1350 \circ C no hold(M79-
1350_1)','FontSize',16)

%normal-normal plot
%figure;
%plotyy(gray,percent1,gray,percent2);
%title('arithmetic frequency histogram of the intercept measurments of the grain structure');

%log-normal plot
```

```
%figure;semilogx(gray,percent1,'-');
%xlabel('intercept length (\mu m)','FontSize',20);
%ylabel('frequency');
figure;semilogx(gray,percent2,'k-');hold on;
b=round(max(percent2)+1);B=[0 b];
%A1=log(avg)*[1 1];A2=log(mode)*[1 1];A3=log(trimean)*[1 1];
A1=avg*[1 1];A2=mode*[1 1];A3=trimean*[1 1];
plot(A1,B,'r--',A2,B,'g:',A3,B,'b-');ylim([0 b]);xlim([0 round(max(gray)+1)]);
xlabel('intercept length (\mu m)','FontSize',20);
ylabel('frequency (%)','FontSize',20);
legend('log freq','mean','mode','trimean');
%title('fig.10 logarithmic frequency curve of grain size distribution in ss316L sintered at 1350 \circ C no
hold(M79-1350_1)','FontSize',16);
%%%[histogram.m] end%%%

%%%[intercept.m] start%%%
function [grainlen,porelen]=intercept(beta,gray,radius)
%--------------------------------------------------------------------------
% Subrountine of analyst.m
% This subroutine counts:
%       -- number of intercepts
%       -- length of each intercept in grain
%       -- length of each intercept in pore
%
%   Rui Zhang <zruier@gmail.com>
%   Version 1.00
%   November, 2004
%--------------------------------------------------------------------------
[m n]=size(gray');
%if the first pt is in grain area
if (gray(1)==106)
   c=1;graincoord(1,1)=1;
   for i=1:m-1
      if ((gray(i)==106)&(gray(i+1)==255))
         graincoord(c,2)=i;
      end
      if ((gray(i)==255)&(gray(i+1)==106))
         c=c+1;graincoord(c,1)=i;
      end
   end
   graincoord(c,2)=m;
   [s1 s2]=size(graincoord);
   grainlen(1)=radius*(...
      abs(beta(graincoord(1,2))-beta(graincoord(1,1)))+...
      abs(beta(graincoord(c,2))-beta(graincoord(c,1))));
   for i=2:s1-1
      grainlen(i)=radius*abs...
         (beta(graincoord(i,2))-beta(graincoord(i,1)));
   end

   if (s1>=1) %in case of zero pore
      for i=1:s1-1
         porelen(i)=radius*...
            abs(beta(graincoord(i+1,1))-beta(graincoord(i,2)));
```

```
      end
   else
      porelen=0;
   end
end

%if the first pt is in pore/boundary area
if (gray(1)==255)
   c=1;porecoord(1,1)=1;
   for i=1:m-1
      if ((gray(i)==255)&(gray(i+1)==106))
         porecoord(c,2)=i;
      end
      if ((gray(i)==106)&(gray(i+1)==255))
         c=c+1;porecoord(c,1)=i;
      end
   end
   porecoord(c,2)=m;
   [s1 s2]=size(porecoord);
   porelen(1)=radius*(...
      abs(beta(porecoord(1,2))-beta(porecoord(1,1)))+...
      abs(beta(porecoord(c,2))-beta(porecoord(c,1))));
   for i=2:s1-1
      porelen(i)=radius*abs...
         (beta(porecoord(i,2))-beta(porecoord(i,1)));
   end

   for i=1:s1-1
      grainlen(i)=radius*...
         abs(beta(porecoord(i+1,1))-beta(porecoord(i,2)));
   end
end
%%%[intercept.m] end%%%

%%%[sumup.m] start%%%
%--------------------------------------------------------------------------
% This program reads all the data and plot the histogram
% It calls subroutine: histogram.m
%   Rui Zhang <zruier@gmail.com>
%   Version 1.00
%   November, 2004
%--------------------------------------------------------------------------
clear all; close all;clc

%import grain intercept data
load ..\results\data\S75\S75_1350_3_200x_01_grain.txt -ASCII
load ..\results\data\S75\S75_1350_3_200x_02_grain.txt -ASCII
load ..\results\data\S75\S75_1350_3_200x_03_grain.txt -ASCII
load ..\results\data\S75\S75_1350_3_200x_04_grain.txt -ASCII
load ..\results\data\S75\S75_1350_3_200x_05_grain.txt -ASCII
load ..\results\data\S75\S75_1350_3_200x_06_grain.txt -ASCII
load ..\results\data\S75\S75_1350_3_200x_07_grain.txt -ASCII
%load ..\results\data\S75\S75_1350_3_200x_08_grain.txt -ASCII
%load ..\results\data\S75\S75_1350_3_200x_09_grain.txt -ASCII
```

```
%load ..\results\data\S75\S75_1350_3_200x_10_grain.txt -ASCII
%load ..\results\data\S75\S75_1350_3_200x_11_grain.txt -ASCII
%load ..\results\data\S75\S75_1350_3_200x_12_grain.txt -ASCII
%load ..\results\data\S75\S75_1350_3_200x_00_grain.txt -ASCII
%import pore intercept data
load ..\results\data\S75\S75_1350_3_200x_01_pore.txt -ASCII
load ..\results\data\S75\S75_1350_3_200x_02_pore.txt -ASCII
load ..\results\data\S75\S75_1350_3_200x_03_pore.txt -ASCII
load ..\results\data\S75\S75_1350_3_200x_04_pore.txt -ASCII
load ..\results\data\S75\S75_1350_3_200x_05_pore.txt -ASCII
load ..\results\data\S75\S75_1350_3_200x_06_pore.txt -ASCII
load ..\results\data\S75\S75_1350_3_200x_07_pore.txt -ASCII
%load ..\results\data\S75\S75_1350_3_200x_08_pore.txt -ASCII
%load ..\results\data\S75\S75_1350_3_200x_09_pore.txt -ASCII
%load ..\results\data\S75\S75_1350_3_200x_10_pore.txt -ASCII
%load ..\results\data\S75\S75_1350_3_200x_11_pore.txt -ASCII
%load ..\results\data\S75\S75_1350_3_200x_12_pore.txt -ASCII
%load ..\results\data\S75\S75_1350_3_200x_00_pore.txt -ASCII
%merge data
[gm(1) a]=size(S75_1350_3_200x_01_grain);
[gm(2) a]=size(S75_1350_3_200x_02_grain);
[gm(3) a]=size(S75_1350_3_200x_03_grain);
[gm(4) a]=size(S75_1350_3_200x_04_grain);
[gm(5) a]=size(S75_1350_3_200x_05_grain);
[gm(6) a]=size(S75_1350_3_200x_06_grain);
[gm(7) a]=size(S75_1350_3_200x_07_grain);
%[gm(8) a]=size(S75_1350_3_200x_08_grain);
%[gm(9) a]=size(S75_1350_3_200x_09_grain);
%[gm(10) a]=size(S75_1350_3_200x_10_grain);
%[gm(9) a]=size(S75_1350_3_200x_11_grain);
%[gm(12) a]=size(S75_1350_3_200x_12_grain);
%[gm(13) a]=size(S75_1350_3_200x_00_grain);

[pm(1) a]=size(S75_1350_3_200x_01_pore);
[pm(2) a]=size(S75_1350_3_200x_02_pore);
[pm(3) a]=size(S75_1350_3_200x_03_pore);
[pm(4) a]=size(S75_1350_3_200x_04_pore);
[pm(5) a]=size(S75_1350_3_200x_05_pore);
[pm(6) a]=size(S75_1350_3_200x_06_pore);
[pm(7) a]=size(S75_1350_3_200x_07_pore);
%[pm(8) a]=size(S75_1350_3_200x_08_pore);
%[pm(9) a]=size(S75_1350_3_200x_09_pore);
%[pm(10) a]=size(S75_1350_3_200x_10_pore);
%[pm(9) a]=size(S75_1350_3_200x_11_pore);
%[pm(12) a]=size(S75_1350_3_200x_12_pore);
%[pm(13) a]=size(S75_1350_3_200x_00_pore);

grainlen(1:gm(1))=S75_1350_3_200x_01_grain;
grainlen(gm(1)+1:gm(1)+gm(2))=S75_1350_3_200x_02_grain;
grainlen(gm(1)+gm(2)+1:gm(1)+gm(2)+gm(3))=S75_1350_3_200x_03_grain;
a=gm(1)+gm(2)+gm(3);
grainlen(a+1:a+gm(4))=S75_1350_3_200x_04_grain;
grainlen(a+gm(4)+1:a+gm(4)+gm(5))=S75_1350_3_200x_05_grain;
grainlen(a+gm(4)+gm(5)+1:a+gm(4)+gm(5)+gm(6))=S75_1350_3_200x_06_grain;
```

```
a=a+gm(4)+gm(5)+gm(6);
grainlen(a+1:a+gm(7))=S75_1350_3_200x_07_grain;
%grainlen(a+gm(7)+1:a+gm(7)+gm(8))=S75_1350_3_200x_08_grain;
%grainlen(a+gm(7)+gm(8)+1:a+gm(7)+gm(8)+gm(9))=S75_1350_3_200x_09_grain;
%a=a+gm(7)+gm(8)+gm(9);
%grainlen(a+1:a+gm(10))=S75_1350_3_200x_10_grain;
%grainlen(a+gm(10)+1:a+gm(10)+gm(11))=S75_1350_3_200x_11_grain;
%grainlen(a+gm(10)+gm(11)+1:a+gm(10)+gm(11)+gm(12))=S75_1350_3_200x_12_grain;
%a=a+gm(10)+gm(11)+gm(12);
%grainlen(a+1:a+gm(13))=S75_1350_3_200x_00_grain;

porelen(1:pm(1))=S75_1350_3_200x_01_pore;
porelen(pm(1)+1:pm(1)+pm(2))=S75_1350_3_200x_02_pore;
porelen(pm(1)+pm(2)+1:pm(1)+pm(2)+pm(3))=S75_1350_3_200x_03_pore;
a=pm(1)+pm(2)+pm(3);
porelen(a+1:a+pm(4))=S75_1350_3_200x_04_pore;
porelen(a+pm(4)+1:a+pm(4)+pm(5))=S75_1350_3_200x_05_pore;
porelen(a+pm(4)+pm(5)+1:a+pm(4)+pm(5)+pm(6))=S75_1350_3_200x_06_pore;
a=a+pm(4)+pm(5)+pm(6);
porelen(a+1:a+pm(7))=S75_1350_3_200x_07_pore;
%porelen(a+pm(7)+1:a+pm(7)+pm(8))=S75_1350_3_200x_08_pore;
%porelen(a+pm(7)+pm(8)+1:a+pm(7)+pm(8)+pm(9))=S75_1350_3_200x_09_pore;
%a=a+pm(7)+pm(8)+pm(9);
%porelen(a+1:a+pm(10))=S75_1350_3_200x_10_pore;
%porelen(a+pm(10)+1:a+pm(10)+pm(11))=S75_1350_3_200x_11_pore;
%porelen(a+pm(10)+pm(11)+1:a+pm(10)+pm(11)+pm(12))=S75_1350_3_200x_12_pore;
%a=a+pm(10)+pm(11)+pm(12);
%porelen(a+1:a+pm(13))=S75_1350_3_200x_00_pore;

%plot & display
[gmean gmode gtrimean g25 g75 ggray gculper ginper]=histogram(grainlen);%grainlen should be 1xn
[pmean pmode ptrimean p25 p75 pgray pculper pinper]=histogram(porelen);%porelen should be 1xn
grainlen=grainlen';
porelen=porelen';
gmsum=sum(gm);pmsum=sum(pm);
disp('arithmetic average grain intercept length (mean):');disp(gmean);
disp('most frequent grain intercept length (mode):');disp(gmode);
disp('trimean of grain intercept length (trimean):');disp(gtrimean);
disp('arithmetic average pore intercept length (mean):');disp(pmean);
disp('most frequent pore intercept length (mode):');disp(pmode);
disp('trimean of pore intercept length (trimean):');disp(ptrimean);
disp('number of intercepts in grain area:');[m n]=size(grainlen);disp(m);
disp('number of intercepts in pore area:');[m n]=size(porelen);disp(m);
disp('25% of grain size');disp(g25);
disp('75% of grain size');disp(g75);

%export
save ..\results\data\S75\S75_1350_3_200x_grain.txt grainlen -ASCII
save ..\results\data\S75\S75_1350_3_200x_pore.txt porelen -ASCII
%%%[sumup.m] end%%%
```

A.3 Statistical Analysis

```
%%%[preexfacor.m] start%%%
%-------------------------------------------------------------------------
% This is the main code that find the pre-exponental factor for gg equation
%
%subroutines:
%curvefit1.m, sinteringcycle.m
%
%copyright Rui Zhang @ PennState
%July 2005
%-------------------------------------------------------------------------
close all; clear all;

L75e=[1150 5.34e-6; 1200 5.42e-6; 1250 7.59e-6; 1350 16.32e-6];
L79e=[1100 5.68e-6; 1200 5.89e-6; 1250 6.69e-6; 1350 15.96e-6];
M75e=[1100 4.63e-6; 1150 5.19e-6; 1200 6.64e-6; 1250 6.62e-6; ...
      1350 14.37e-6; 1350 15.32e-6];
M79e=[1200 5.77e-6; 1250 5.94e-6; 1350 7.54e-6; 1350 14.16e-6];
S75e=[1100 4.36e-6; 1150 4.45e-6; 1200 4.68e-6; 1250 5.80e-6; ...
      1350 7.01e-6; 1350 11.52e-6; 1350 13.71e-6];
S79e=[1100 4.31e-6; 1150 4.62e-6; 1200 4.63e-6; ...
   1250 5.69e-6; 1300 6.66e-6; 1350 7.14e-6; 1350 10.38e-6; ...
   1350 12.82e-6];

trialdt=[6000 600 300 240 120 60 30 20 15 10 7];
[m1 m2]=size(trialdt);

for i=1:m2
   AS75(i)=curvefit1(trialdt(i),S75e);
   AS79(i)=curvefit1(trialdt(i),S79e);
   AM75(i)=curvefit1(trialdt(i),M75e);
   AM79(i)=curvefit1(trialdt(i),M79e);
   AL75(i)=curvefit1(trialdt(i),L75e);
   AL79(i)=curvefit1(trialdt(i),L79e);
   [T t m(i)]=sinteringcycle(trialdt(i));
end

plot(m,AS75,'ko--',m,AS79,'ko-',...
   m,AM75,'bs--',m,AM79,'bs-',...
   m,AL75,'rd--',m,AL79,'rd-',...
   'LineWidth',1);hold on;
ylim([0,12e-13]);
legend('S75','S79','M75','M79','L75','L79',4);
%title('Convergence Curves','FontSize',20);
ylabel('Pre-exponential Factor (m^2/s)','FontSize',16);
xlabel('Total Time Step (#)','FontSize',16);
%%%[preexfacor.m] end%%%

%%%[curvefit1.m] start%%%
%-------------------------------------------------------------------------
% This is a subroutine that will be called by preexfactor.m
%
```

```
%subroutines:
%curvefit.m, sinteringcycle.m
%
%copyright Rui Zhang @ PennState
%July 2005
%-------------------------------------------------------------------------

function A=curvefit1(dt,eresult)
[T t m]=sinteringcycle(dt);
[A D]=curvefit(eresult,dt,T,t,m);
%%%[curvefit1.m] end%%%

%%%[sinteringcycle.m] start%%%
function [T t m]=sinteringcycle(dt)
%-------------------------------------------------------------------------
%this is a subroutine for curvefit.m
%input: dt--time step length(sec)
%output: T--temperature array(unit:C)
%       t--time array(unit:sec)
%       m--# of total time steps
%apply sintering cycle:
%heating rate 10C/min from 20 to 1350
%holding period 60 mins
%negelect--cooling rate 10C/min from 1350 to 18
%
%copyright Rui Zhang @ PennState
%July 2005
%-------------------------------------------------------------------------

totaltime=((1350-20)/10+60)*60;m=round(totaltime/dt)+1;t(1)=0;
for i=2:m-1
   t(i)=(i-1)*dt;
end
t(m)=totaltime;
T(1)=20;t1=(1350-20)/10*60;n=round(t1/dt)+1;
for i=2:n-1
   T(i)=20+t(i)/60*10;
end
T(n)=1350;t(n)=t1;
for i=n+1:m
   T(i)=1350;
end
%%%[sinteringcycle.m] end%%%

%%%[curvefit.m] start%%%
function [A D]=curvefit(measurepoints,dt,T,t,m)
%-------------------------------------------------------------------------
%this is a function that finds the fit pre-exponental factor for gg equation
%input: measurepoints--nx2 array contains temperature/grain size data
%output: A--the fit value for pre-exponantial factor
%       D--data array of predicted gg curve
%other parameters used:
%      D0--initial grain size
%      Df--final grain size
```

```
%       t--an array of data representing the sintering time (minute)
%       T--an array of data representing the sintering temp (C)
%
%algorithm of fitting the data point:
% 1. give a guest at A0=1e-10 level, find the lower bound A1 and
% upper bound A2 so that Df is between the values predicted by these two
% boundaries. (usage of subroutine Gcurve(A,T,m,D0))
% 2. use the mid point searching method to locate the fit A
% 3. output
%
%subroutines:
%Gcurve.m, sinteringcycle.m
%
%copyright Rui Zhang @ PennState
%July 2005
%--------------------------------------------------------------------------

%read the initial and final grain size from the measured data
[n1 n2]=size(measurepoints);
D0=measurepoints(1,2);Df=measurepoints(n1,2);

%step 1: find the lower bound (A1) and upper bound (A2)
%note: the larger the A, the bigger the final grain size
A1=1e-10;A2=A1*10;%inital guess of A
count=0;limit=10;
while ((count<=limit) & (max(Gcurve(A1,D0,dt,T,t,m))>Df))
   A2=A1;A1=A1/10;count=count+1;
end
while ((count<limit) & (max(Gcurve(A2,D0,dt,T,t,m))<Df))
   A1=A2;A2=A2*10;count=count+1;
end

%step 2: refine the search for fitting point
count=0;limit=50;err=1e-8;
while ((count<=limit) & ...
      (min(abs(max(Gcurve(A1,D0,dt,T,t,m))-Df),...
      abs(max(Gcurve(A2,D0,dt,T,t,m))-Df))>=err))
   Am=(A1+A2)/2;count=count+1;
   if (max(Gcurve(Am,D0,dt,T,t,m))>Df)
      A2=Am;
   end
   if (max(Gcurve(Am,D0,dt,T,t,m))<Df)
      A1=Am;
   end
end

%step 3: output the result
if (abs(max(Gcurve(A1,D0,dt,T,t,m))-Df) >= ...
      abs(max(Gcurve(A2,D0,dt,T,t,m))-Df))
   A=A2;
else
   A=A1;
end
D=Gcurve(A,D0,dt,T,t,m);
```

```
%%%[curvefit.m] end%%%

%%%[Gcurve.m] start%%%
function D=Gcurve(A,D0,dt,T,t,m)
%--------------------------------------------------------------------------
%this is a subroutine for curvefit.m
%input: A--pre-exponential factor
%       D0--initial gain size(unit:m)
%output: Df--final grain size(unit:m)
%
%copyright Rui Zhang @ PennState
%July 2005
%--------------------------------------------------------------------------

Qg1=315.8e3;Qg2=50.0e3;R=8.314;D(1)=D0;
for i=2:m
   if T(i)<1200
      Qg=Qg1;
   else
      Qg=Qg2;
   end
   dD=A*exp(-Qg/(R*(T(i)+273)))/D(i-1)*dt;
   D(i)=D(i-1)+dD;
end
%%%[Gcurve.m] end%%%
```

Appendix B

FEM Scheme, SinSolver and ABAQUS Codes

B.1 Finite Element Method

Metal powders under high temperature sintering exhibit time-dependent response to applied loads. The sintering simulation is treated as a quasi static problem. Within each time increment, the Newton-Raphson algorithm is used for iteration. In addition, since the deformation in sintering could be up to 3% or more, it is reasonable to use large deformation formulation in the FEM scheme.

B.1.1 Weak Formulation (Total Lagrange Form)

A weak formulation of the momentum balance is shown in Equation **B.1**

$$\int_{V_0} \{\nabla_X \hat{\mathbf{u}} : \mathbf{P} - \hat{\mathbf{u}} \cdot \mathbf{b}_X\} dV_0 - \int_{A_0} \hat{\mathbf{u}} \cdot \mathbf{t}^P_X dA_0 = \mathbf{0}, \qquad \text{Eq. B.1}$$

where $\hat{\mathbf{u}}$ is a kinematic admissible function (the weight function in the Galerkin method), satisfying all geometric boundary conditions, $\mathbf{P}$ is the first Piola-Kirchhoff stress, b_X is the body force vector, $\mathbf{t}^P_X$ is the external force on the boundary, $\mathbf{V_0}$ is the initial body volume, $\mathbf{A_0}$ is the boundary surface of $\mathbf{V_0}$. Equation **B.1** can be rewritten to Equation **B.2** using the second Piola-Kirchhoff stress, $\mathbf{S}$. The relation between $\mathbf{P}$ and $\mathbf{S}$ is $\mathbf{P} = \mathbf{F} \cdot \mathbf{S}$, where $\mathbf{F}$ is the deformation gradient.

$$\int_{V_0} \{\nabla_X \hat{\mathbf{u}} : (\mathbf{F} \cdot \mathbf{S}) - \hat{\mathbf{u}} \cdot \mathbf{b}_X\} dV_0 - \int_{A_0} \hat{\mathbf{u}} \cdot \mathbf{t}^P_X dA_0 = \mathbf{0}. \qquad \text{Eq. B.2}$$

Because the second Piola-Kirchhoff stress is symmetric, Equation **B.2** can be rewritten as

$$\int_{V_0} \left\{ \mathbf{sym}(\mathbf{F}^{\mathbf{T}} \cdot \nabla_{\mathbf{X}} \hat{\mathbf{u}}) : \mathbf{S} - \hat{\mathbf{u}} \cdot \mathbf{b}_{\mathbf{X}} \right\} \mathbf{dV_0} - \int_{A_0} \hat{\mathbf{u}} \cdot \mathbf{t}_{\mathbf{X}}^{\mathbf{p}} \mathbf{dA_0} = \mathbf{0}, \qquad \text{Eq. } \mathbf{B.3}$$

where sym() represents the symmetric part of the product.

B.1.2 Residual and Stiffness in Quasi Static Problem

Let $\{{}^0\mathcal{U}, {}^1\mathcal{U}, \ldots, {}^{n-1}\mathcal{U}, {}^n\mathcal{U}, \ldots\}$ be the solution for the incremental scheme for times $\{{}^0t, {}^1t, \ldots, {}^{n-1}t, {}^nt, \ldots\}$.Finite element discretization is applied to the variational equation (Equation **B.3**) to obtain the expressions for the global residual.

$$\mathcal{R}({}^{n-1}\mathcal{U}, {}^n\mathcal{U}) = \sum_{elements} [\mathbf{R}({}^{n-1}\mathbf{U}, {}^n\mathbf{U})] = \mathbf{0} \quad \text{on } V_0 \text{ and } A_{0t} \qquad \text{Eq. } \mathbf{B.4}$$

where $\mathcal{R}$ is the global residual, $\mathcal{U}$ is the global displacement, **R** is the element residual, and **U** the element displacement. The element residual is evaluated as

$$\mathbf{R}({}^{n-1}\mathbf{U}, {}^n\mathbf{U}) = \sum_{V_{0GaussPoint}} [\mathbf{B_{nl}}^{\mathbf{T}} {}^n\overline{\mathbf{S}} - \mathbf{N}^{\mathbf{T}} \mathbf{b}_{\mathbf{X}}] w J_X - \sum_{A_{0tGaussPoint}} \mathbf{N}^{\mathbf{T}} \mathbf{t}_{\mathbf{X}}^{\mathbf{p}} w j_X \,, \qquad \text{Eq. } \mathbf{B.5}$$

where matrices **N** and $\mathbf{B_{nl}}$ are the shape function matrix and strain operator defined in the next section, respectively, w is the weight factor of the Gauss integral, J_x and j_x are the Jacobians of the reference mapping, ${}^n\overline{\mathbf{S}}$ is the second Piola-Kirchhoff stress at time ${}^nt$ written in vector form:

$${}^n\overline{\mathbf{S}} = \begin{pmatrix} {}^n\sigma_1 \\ {}^n\sigma_2 \\ {}^n\tau_{12} \end{pmatrix}. \qquad \text{Eq. } \mathbf{B.6}$$

The stress at time ${}^nt$ is computed as follows:

$$ {}^{n}\bar{\mathbf{S}} = {}^{n-1}\bar{\mathbf{S}} + \Delta\bar{\mathbf{S}} , \qquad \text{Eq. } \mathbf{B.7} $$

where $\Delta\bar{\mathbf{S}}$ equals the product of the elastic modulus matrix and the increment of strain vector. Because the elastic deformation in the free sintering problem is so small that it can be ignored, it is reasonable to assume a constant elastic modulus matrix in the simulation.

The residual of Equation **B.4** is minimized by solving for the global displacement vector ${}^{n}\mathcal{U}$ iteratively. An initial starting solution ${}^{n}\mathcal{U}^{1}$ is assumed and the Newton-Raphson method is applied to determine a corrected displacement field. Usually the initial solution can be assumed as the solution of the previous increment ${}^{n}\mathcal{U}^{1} = {}^{n-1}\mathcal{U}$. Application of the Newton-Raphson linearization yields the following iterative scheme for the computation of displacement field:

$$ \delta\mathcal{U} = -\left[\mathbf{d}\mathcal{R}/\mathbf{d}^{n}\mathcal{U}\,|^{n}\mathcal{U}^{I}\right]^{-1} \mathcal{R}({}^{n-1}\mathcal{U}, {}^{n}\mathcal{U})|^{n}\mathcal{U}^{I}, \qquad \text{Eq. } \mathbf{B.8} $$

and

$$ {}^{n}\mathcal{U}^{I+1} = {}^{n}\mathcal{U}^{I} + {}^{n}\delta\mathcal{U}.. \qquad \text{Eq. } \mathbf{B.9} $$

In the iteration, the displacement field is updated with Equation **B.8** and Equation **B.9**, until the residual becomes small enough and the solution converges. The tangent stiffness $\mathbf{d}\mathcal{R}/\mathbf{d}^{n}\mathcal{U}$ in Equation **B.8** is calculated by differentiating the residual with respect to the nodal displacement vector $\mathcal{U}$:

$$ \mathbf{d}\mathcal{R}/\mathbf{d}^{n}\mathcal{U} = \sum_{elements} \left[\frac{d\mathbf{R}}{d\,{}^{n}\mathbf{U}}\right] , \qquad \text{Eq. } \mathbf{B.10} $$

where the element stiffness is derived by differentiating Equation **B.5** with respect to the element displacement vector:

$$\frac{\mathbf{dR}}{\mathbf{d}^{n}\mathbf{U}} = \sum_{\mathbf{V_{oGaussPoint}}} [\mathbf{B}_{nl}^{T} \frac{\mathbf{d}^{n}\overline{\mathbf{S}}}{\mathbf{d}^{n}\overline{\boldsymbol{\varepsilon}}} \mathbf{B}_{nl} + \mathbf{G}_{N}{}^{T\,n}\widetilde{\mathbf{S}}\mathbf{G} - \mathbf{N}^{T} \frac{\mathbf{db}_{X}}{\mathbf{d}^{n}\mathbf{U}}]\mathbf{wJ}_{X} - \sum_{\mathbf{A_{otGaussPoint}}} [\mathbf{N}^{T} \frac{\mathbf{dt}^{p}_{x}}{\mathbf{d}^{n}\mathbf{U}}]\mathbf{wj}_{X} . \quad \text{Eq. } \mathbf{B.11}$$

Equation **B.11** shows that the element stiffness matrix consists of three components: the material stiffness, the geometric of stress stiffness and the load stiffness. The material stiffness is defined as

$$\frac{\mathbf{dR}}{\mathbf{d}^{n}\mathbf{U}}\Big|_{\mathbf{mat}} = \sum_{\mathbf{V_{oGaussPoint}}} [\mathbf{B}_{nl}^{T} \frac{\mathbf{d}^{n}\overline{\mathbf{S}}}{\mathbf{d}^{n}\overline{\boldsymbol{\varepsilon}}} \mathbf{B}_{nl}]\mathbf{wJ}_{X} \ , \qquad \text{Eq. } \mathbf{B.12}$$

where $\frac{\mathbf{d}^{n}\overline{\mathbf{S}}}{\mathbf{d}^{n}\overline{\varepsilon}}$ is actually the elastic modulus matrix **C**. The geometric of stress stiffness is

$$\frac{\mathbf{d}^{n}\mathbf{R}}{\mathbf{d}^{n}\mathbf{U}}\Big|_{\mathbf{geom}} = \sum_{\mathbf{V_{oGaussPoint}}} [\mathbf{G}_{N}{}^{T\,n}\widetilde{\mathbf{S}}\mathbf{G}]\mathbf{wJ}_{X} \ , \qquad \text{Eq. } \mathbf{B.13}$$

where ${}^{n}\widetilde{\mathbf{S}}$ is the expanded stress matrix

$${}^{n}\widetilde{\mathbf{S}} = \begin{pmatrix} {}^{n}\sigma_1 & {}^{n}\tau_{12} & 0 & 0 \\ {}^{n}\tau_{12} & {}^{n}\sigma_2 & 0 & 0 \\ 0 & 0 & {}^{n}\sigma_1 & {}^{n}\tau_{12} \\ 0 & 0 & {}^{n}\tau_{12} & {}^{n}\sigma_2 \end{pmatrix}, \qquad \text{Eq. } \mathbf{B.14}$$

and $\mathbf{G_N}$ is the geometric operator that defines gradient of the shape function in the initial configuration,

$$\mathbf{G}_{N} = \begin{pmatrix} \frac{\partial N1}{\partial r1} & 0 & \frac{\partial N2}{\partial r1} & 0 & \frac{\partial N3}{\partial r1} & 0 & \frac{\partial N4}{\partial r1} & 0 \\ 0 & \frac{\partial N1}{\partial r1} & 0 & \frac{\partial N2}{\partial r1} & 0 & \frac{\partial N3}{\partial r1} & 0 & \frac{\partial N4}{\partial r1} \\ \frac{\partial N1}{\partial r2} & 0 & \frac{\partial N2}{\partial r2} & 0 & \frac{\partial N3}{\partial r2} & 0 & \frac{\partial N4}{\partial r2} & 0 \\ 0 & \frac{\partial N1}{\partial r2} & 0 & \frac{\partial N2}{\partial r2} & 0 & \frac{\partial N3}{\partial r2} & 0 & \frac{\partial N4}{\partial r2} \end{pmatrix}. \qquad \text{Eq. } \mathbf{B.15}$$

The load stiffness is

$$\frac{\mathbf{dR}}{\mathbf{d^n U}}\Big|_{\mathbf{load}} = -\sum_{\mathbf{V_{oGaussPoint}}} [\mathbf{N^T}\frac{\mathbf{db_X}}{\mathbf{d^n U}}]\mathbf{wJ_X} - \sum_{\mathbf{A_{otGaussPoint}}} [\mathbf{N^T}\frac{\mathbf{dt^p_x}}{\mathbf{d^n U}}]\mathbf{wj_X}\,. \qquad \text{Eq. } \mathbf{B.16}$$

B.1.3 Mapping

For a two-dimensional problem, a reference map (Figure **B.1**) is defined between the local reference configuration r and the global reference configuration x:

$$\begin{aligned} x1 &= xc1 + r1 \times a\,, \\ x2 &= xc2 + r2 \times b\,. \end{aligned} \qquad \text{Eq. } \mathbf{B.17}$$

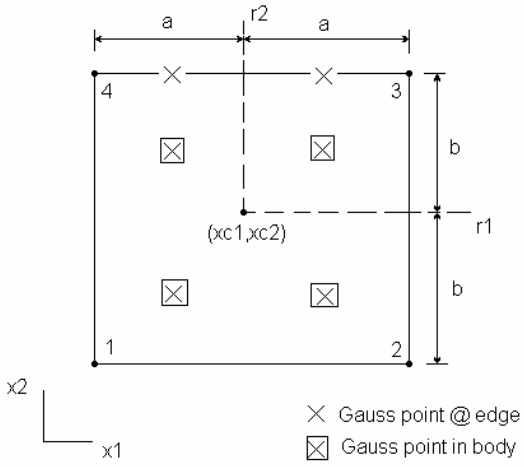

Fig. **B.1**: Mapping between the Local Reference Configuration and the Global Reference Configuration

The shape functions are defined as

$$\begin{aligned} N1 &= (1-r1)(1-r2)/4\,, \\ N2 &= (1+r1)(1-r2)/4\,, \\ N3 &= (1+r1)(1+r2)/4\,, \\ N4 &= (1-r1)(1+r2)/4\,, \end{aligned} \qquad \text{Eq. } \mathbf{B.18}$$

and the shape function matrix is defined as

$$\mathbf{N} = \begin{pmatrix} N1 & 0 & N2 & 0 & N3 & 0 & N4 & 0 \\ 0 & N1 & 0 & N2 & 0 & N3 & 0 & N4 \end{pmatrix}. \qquad \text{Eq. } \mathbf{B.19}$$

For isoparametric elements, interpolation of coordinate x and displacement u are the same, as shown below:

$$\underline{\mathbf{x}} = \begin{pmatrix} \mathbf{x}1 \\ \mathbf{x}2 \end{pmatrix} = \mathbf{N} \cdot \mathbf{X} \qquad \text{Eq. } \mathbf{B.20}$$

and

$$\underline{\mathbf{u}} = \begin{pmatrix} u1 \\ u2 \end{pmatrix} = \mathbf{N} \cdot \mathbf{U} \qquad \text{Eq. } \mathbf{B.21}$$

where **X** and **U** are in vector form and defined as

$$\mathbf{X} = \begin{pmatrix} X1_1 \\ X2_1 \\ X1_2 \\ X2_2 \\ X1_3 \\ X2_3 \\ X1_4 \\ X2_4 \end{pmatrix}, \qquad \text{Eq. } \mathbf{B.22}$$

and

$$\mathbf{U} = \begin{pmatrix} U1_1 \\ U2_1 \\ U1_2 \\ U2_2 \\ U1_3 \\ U2_3 \\ U1_4 \\ U2_4 \end{pmatrix}. \qquad \text{Eq. } \mathbf{B.23}$$

Note that the subscript denotes the node number in these two equations. The deformation gradient and displacement gradient are defined as

$$\mathbf{F} = \frac{\partial \mathbf{x}}{\partial \mathbf{X}} = \begin{pmatrix} \frac{\partial x1}{\partial X1} & \frac{\partial x1}{\partial X2} \\ \frac{\partial x2}{\partial X1} & \frac{\partial x2}{\partial X2} \end{pmatrix}, \qquad \text{Eq. } \mathbf{B.24}$$

and

$$\mathbf{D} = \frac{\partial \mathbf{u}}{\partial \mathbf{X}} = \begin{pmatrix} \frac{\partial u1}{\partial X1} & \frac{\partial u1}{\partial X2} \\ \frac{\partial u2}{\partial X1} & \frac{\partial u2}{\partial X2} \end{pmatrix}, \qquad \text{Eq. } \mathbf{B.25}$$

where the X1-X2 is the reference frame, and x1-x2 is the current frame. In this problem, r1-r2 is the reference frame. It can be derived from the definitions that the relation between the deformation gradient and displacement gradient is

$$\mathbf{F=I+D}\ , \qquad \text{Eq. } \mathbf{B.26}$$

where **I** is the identity matrix.

For large deformation analysis, the strain operator $\mathbf{B_{nl}}$ is defined as

$$\mathbf{B_{nl}U} = \mathbf{L} \cdot [\mathrm{sym}(\mathbf{F}^{\mathbf{T}} \cdot \nabla_X \hat{\mathbf{u}})]_{\mathrm{vectorform}}\ , \qquad \text{Eq. } \mathbf{B.27}$$

where **L** is a transformation matrix that transforms the Green strain matrix to the engineering strain vector, $\nabla_X \hat{u}$ .is actually the deformation gradient **D**. The engineering strain vector **ε** can be derived by Substituting Equation **B.26** and replacing $\nabla_X \hat{u}$ with **D** in Equation **B.27:**

$$\begin{aligned} \mathbf{B_{nl}U} &= \mathbf{L} \cdot [\mathrm{sym}(\mathbf{F}^{\mathbf{T}} \cdot \mathbf{D})]_{\mathrm{vectorform}} \\ &= \mathbf{L} \cdot [\mathrm{sym}((\mathbf{D}+\mathbf{I})^{\mathbf{T}} \cdot \mathbf{D})]_{\mathrm{vectorform}} \\ &= \mathbf{L} \cdot [\mathrm{sym}(\mathbf{D}^{\mathbf{T}} \cdot \mathbf{D} + \mathbf{D})]_{\mathrm{vectorform}} \\ &= \mathbf{L} \cdot [\frac{1}{2}(\mathbf{D} + \mathbf{D}^{\mathbf{T}} + \mathbf{D}^{\mathrm{T}} \cdot \mathbf{D})]_{\mathrm{vectorform}} \\ &= \mathbf{L} \cdot \overline{\mathbf{E}} = \boldsymbol{\varepsilon}\ , \end{aligned} \qquad \text{Eq. } \mathbf{B.28}$$

where the green strain in engineering form is interpolated as

$$\boldsymbol{\varepsilon} = \begin{pmatrix} \varepsilon 1 \\ \varepsilon 2 \\ \gamma 12 \end{pmatrix} = \mathbf{B} \cdot \mathbf{U}, \qquad \text{Eq. } \mathbf{B.29}$$

and the green strain in vector form is $\overline{\mathbf{E}} = \begin{pmatrix} \varepsilon 1 \\ \varepsilon 2 \\ \varepsilon 12 \end{pmatrix}$ and $\mathbf{L} = \begin{pmatrix} 1 & 0 & 0 \\ 0 & 1 & 0 \\ 0 & 0 & 2 \end{pmatrix}$.

The green strain matrix is

$$\mathbf{E} = \frac{1}{2}(\mathbf{D} + \mathbf{D}^{\mathbf{T}} + \mathbf{D}^{\mathrm{T}} \cdot \mathbf{D})$$

$$= \frac{1}{2}\begin{pmatrix} 2\frac{\partial u1}{\partial r1} + \left(\frac{\partial u1}{\partial r1}\right)^2 + \left(\frac{\partial u2}{\partial r1}\right)^2 & \frac{\partial u2}{\partial r1} + \frac{\partial u1}{\partial r2} + \frac{\partial u1}{\partial r2}\frac{\partial u1}{\partial r1} + \frac{\partial u2}{\partial r2}\frac{\partial u2}{\partial r1} \\ \frac{\partial u2}{\partial r1} + \frac{\partial u1}{\partial r2} + \frac{\partial u1}{\partial r2}\frac{\partial u1}{\partial r1} + \frac{\partial u2}{\partial r2}\frac{\partial u2}{\partial r1} & 2\frac{\partial u2}{\partial r2} + \left(\frac{\partial u1}{\partial r2}\right)^2 + \left(\frac{\partial u2}{\partial r2}\right)^2 \end{pmatrix}, \qquad \text{Eq. } \mathbf{B.30}$$

and the green strain in engineering form is

$$\boldsymbol{\varepsilon} = \begin{pmatrix} \varepsilon 1 \\ \varepsilon 2 \\ \gamma 12 \end{pmatrix} = \begin{pmatrix} \frac{\partial u1}{\partial r1} \\ \frac{\partial u2}{\partial r2} \\ \frac{\partial u2}{\partial r1} + \frac{\partial u1}{\partial r2} \end{pmatrix} + \begin{pmatrix} \frac{1}{2}\left(\left(\frac{\partial u1}{\partial r1}\right)^2 + \left(\frac{\partial u2}{\partial r1}\right)^2\right) \\ \frac{1}{2}\left(\left(\frac{\partial u1}{\partial r2}\right)^2 + \left(\frac{\partial u2}{\partial r2}\right)^2\right) \\ \frac{\partial u1}{\partial r2}\frac{\partial u1}{\partial r1} + \frac{\partial u2}{\partial r2}\frac{\partial u2}{\partial r1} \end{pmatrix}. \qquad \text{Eq. } \mathbf{B.31}$$

In Equation **B.28**, the strain operators corresponding to $\boldsymbol{\varepsilon}$ is defined as

$$\mathbf{B_{nl}} = \begin{pmatrix} \frac{\partial N1}{\partial r1} & 0 & \frac{\partial N2}{\partial r1} & 0 & \frac{\partial N3}{\partial r1} & 0 & \frac{\partial N4}{\partial r1} & 0 \\ 0 & \frac{\partial N1}{\partial r2} & 0 & \frac{\partial N2}{\partial r2} & 0 & \frac{\partial N3}{\partial r2} & 0 & \frac{\partial N4}{\partial r2} \\ \frac{\partial N1}{\partial r2} & \frac{\partial N1}{\partial r1} & \frac{\partial N2}{\partial r2} & \frac{\partial N2}{\partial r1} & \frac{\partial N3}{\partial r2} & \frac{\partial N3}{\partial r1} & \frac{\partial N4}{\partial r2} & \frac{\partial N4}{\partial r1} \end{pmatrix} + \begin{pmatrix} \frac{1}{2}\left(\frac{\partial N1}{\partial r1}\right)^2 & \frac{1}{2}\left(\frac{\partial N1}{\partial r1}\right)^2 & \frac{1}{2}\left(\frac{\partial N2}{\partial r1}\right)^2 & \frac{1}{2}\left(\frac{\partial N2}{\partial r1}\right)^2 & \frac{1}{2}\left(\frac{\partial N3}{\partial r1}\right)^2 & \frac{1}{2}\left(\frac{\partial N3}{\partial r1}\right)^2 & \frac{1}{2}\left(\frac{\partial N4}{\partial r1}\right)^2 & \frac{1}{2}\left(\frac{\partial N4}{\partial r1}\right)^2 \\ \frac{1}{2}\left(\frac{\partial N1}{\partial r2}\right)^2 & \frac{1}{2}\left(\frac{\partial N1}{\partial r2}\right)^2 & \frac{1}{2}\left(\frac{\partial N2}{\partial r2}\right)^2 & \frac{1}{2}\left(\frac{\partial N2}{\partial r2}\right)^2 & \frac{1}{2}\left(\frac{\partial N3}{\partial r2}\right)^2 & \frac{1}{2}\left(\frac{\partial N3}{\partial r2}\right)^2 & \frac{1}{2}\left(\frac{\partial N4}{\partial r2}\right)^2 & \frac{1}{2}\left(\frac{\partial N4}{\partial r2}\right)^2 \\ \frac{\partial N1}{\partial r1}\frac{\partial N1}{\partial r2} & \frac{\partial N1}{\partial r1}\frac{\partial N1}{\partial r2} & \frac{\partial N2}{\partial r1}\frac{\partial N2}{\partial r2} & \frac{\partial N2}{\partial r1}\frac{\partial N2}{\partial r2} & \frac{\partial N3}{\partial r1}\frac{\partial N3}{\partial r2} & \frac{\partial N3}{\partial r1}\frac{\partial N3}{\partial r2} & \frac{\partial N4}{\partial r1}\frac{\partial N4}{\partial r2} & \frac{\partial N4}{\partial r1}\frac{\partial N4}{\partial r2} \end{pmatrix}. \qquad \text{Eq. } \mathbf{B.32}$$

The determinant of F is called the Jacobian of the deformation gradient and denoted by

$$J = \mathrm{Det}(\mathbf{F}) = \mathrm{Det}\begin{pmatrix} \frac{\partial x1}{\partial r1} & \frac{\partial x1}{\partial r2} \\ \frac{\partial x2}{\partial r1} & \frac{\partial x2}{\partial r2} \end{pmatrix}. \qquad \text{Eq. } \mathbf{B.33}$$

The derivatives of x with respect to r can be derived from Equation **B.17**. Substitution of them into Equation **B.33** yields,

$$J = \mathrm{Det}\begin{pmatrix} a & 0 \\ 0 & b \end{pmatrix} = a \cdot b\,. \qquad \text{Eq. } \mathbf{B.34}$$

The geometric operator can be derived by substituting Equation **B.18** into Equation **B.15**,

$$\mathbf{G}_N = \begin{pmatrix} \frac{-1+r2}{4} & 0 & \frac{1-r2}{4} & 0 & \frac{1+r2}{4} & 0 & \frac{-1-r2}{4} & 0 \\ 0 & \frac{-1+r2}{4} & 0 & \frac{1-r2}{4} & 0 & \frac{1+r2}{4} & 0 & \frac{-1-r2}{4} \\ \frac{-1+r1}{4} & 0 & \frac{-1-r1}{4} & 0 & \frac{1+r1}{4} & 0 & \frac{1-r1}{4} & 0 \\ 0 & \frac{-1+r1}{4} & 0 & \frac{-1-r1}{4} & 0 & \frac{1+r1}{4} & 0 & \frac{1-r1}{4} \end{pmatrix}. \qquad \text{Eq. } \mathbf{B.35}$$

And the strain operator can also be derived by substituting Equation **B.18** into Equation **B.32** ,

$$\mathbf{B_{nl}} = \begin{pmatrix} \frac{-1+r2}{4} & 0 & \frac{1-r2}{4} & 0 & \frac{1+r2}{4} & 0 & \frac{-1-r2}{4} & 0 \\ 0 & \frac{-1+r1}{4} & 0 & \frac{-1-r1}{4} & 0 & \frac{1+r1}{4} & 0 & \frac{1-r1}{4} \\ \frac{-1+r1}{4} & \frac{-1+r2}{4} & \frac{-1-r1}{4} & \frac{1-r2}{4} & \frac{1+r1}{4} & \frac{1+r2}{4} & \frac{1-r1}{4} & \frac{-1-r2}{4} \end{pmatrix}$$
$$+ \begin{pmatrix} \frac{1}{2}\left(\frac{-1+r2}{4}\right)^2 & \frac{1}{2}\left(\frac{-1+r2}{4}\right)^2 & \frac{1}{2}\left(\frac{1-r2}{4}\right)^2 & \frac{1}{2}\left(\frac{1-r2}{4}\right)^2 & \frac{1}{2}\left(\frac{1+r2}{4}\right)^2 & \frac{1}{2}\left(\frac{1+r2}{4}\right)^2 & \frac{1}{2}\left(\frac{-1-r2}{4}\right)^2 & \frac{1}{2}\left(\frac{-1-r2}{4}\right)^2 \\ \frac{1}{2}\left(\frac{-1+r1}{4}\right)^2 & \frac{1}{2}\left(\frac{-1+r1}{4}\right)^2 & \frac{1}{2}\left(\frac{-1-r1}{4}\right)^2 & \frac{1}{2}\left(\frac{-1-r1}{4}\right)^2 & \frac{1}{2}\left(\frac{1+r1}{4}\right)^2 & \frac{1}{2}\left(\frac{1+r1}{4}\right)^2 & \frac{1}{2}\left(\frac{1-r1}{4}\right)^2 & \frac{1}{2}\left(\frac{1-r1}{4}\right)^2 \\ \frac{-1+r2}{4}\frac{-1+r1}{4} & \frac{-1+r2}{4}\frac{-1+r1}{4} & \frac{1-r2}{4}\frac{-1-r1}{4} & \frac{1-r2}{4}\frac{-1-r1}{4} & \frac{1+r2}{4}\frac{1+r1}{4} & \frac{1+r2}{4}\frac{1+r1}{4} & \frac{-1-r2}{4}\frac{1-r1}{4} & \frac{-1-r2}{4}\frac{1-r1}{4} \end{pmatrix}. \qquad \text{Eq. } \mathbf{B.36}$$

B.2 SinSolver Code

```
%%%[sinsolver1d.m] start%%%
function sinsolver1d(x)
%--------------------------------------------------------------------------
% finite element code for sintering simulation
% linear visco-elasticity law
% using Newton-Raphson iterative scheme
% with measured grain growth curve
% 1D version
% subroutines:
```

```
% ge1d.m, stiff1d.m, grain1d.m, creep1d.m, thermal1d.m, drawerr1d.m
%
%Copyright Rui Zhang @ PennState 2005
%contact:<rzhang@psu.edu>
%-------------------------------------------------------------------------
clear all;format short e;close all;
global xy NT IB time dt tmax time_s temp_s

%--------------geometry---------------------------------
%generate nodes and elements
hi=12.03e-3; rad=6.0e-3; sh=3; sr=6;
%hi:   initial height of cylinder (m);
%rad:  initial radius of cylinder (m);
%sh:   number of elements along the height;
%sr:   number of elements along the radius;
[xy, NT, bount, int, IB, nn, ne]=ge1d(hi, sh);
%coordinates for nodes:   xy(nn, 1:2)
%element index:          NT(ne,1:3)
%define boundary nodes:   bound
%define interior nodes:   int
%mark the boundary nodes: IB

%-------Newton-Raphson interative scheme----------------
%read dilatometry data S83
load diladata_S83_M83_L83 time_s temp_s;[a b]=size(time_s);
time=60*time_s(a);  %total time
dt=30;tmax=ceil(time/dt);

%initialization
U0=zeros(nn,1);dU=zeros(nn,1);maxinc=10;err=1.0e-15;
UT=zeros(tmax,nn);ET=zeros(tmax,ne);ST=ET;ECT=ET;PRT=ET;ETHT=ET;
VIST=ET;KCT=ET;SST=ET;alphaT=ET;EC=zeros(ne,1);dEC=0;EC0=0;ETH=EC;
GT=ones(tmax,ne)*4.31e-6;
%initial grain size
%L83:5.68e-6;M83:5.77e-6;S83:4.31e-6

for tin=1:tmax
   tin,
   if tin==tmax
      dt=time-dt*(tmax-1);
   end
   er=1;tr=0;
   for it=1:maxinc
      [A,R,E,S,PR]=stiff1d(U0,EC,ETH,tin);
      AA=A(2:nn,2:nn);RR=R(2:nn);
      dUU=-inv(AA)*RR;
      dU(2:nn)=dUU(1:nn-1);
      U=U0+dU;
      if er<norm(U-U0)
         display('!!!error:divergence!!!');
         tr=1;
         break
      end
      er=norm(U-U0);U0=U;
```

```
        if er<err
            %calculate the CREEP strain
            for k=1:ne
                dG=grain1d(tin,GT(tin,k));
                if tin~=1
                    GT(tin,k)=GT(tin-1,k)+dG;
                else
                    GT(tin,k)=GT(tin,k)+dG;
                end
                G=GT(tin,k);
                [dEC,VIS0,KC0,SS0]=creep1d(S(k),PR(k),G,tin);
                EC0=EC0+dEC;EC(k)=EC0;
                VIST(tin,k)=VIS0;
                KCT(tin,k)=KC0;
                SST(tin,k)=SS0;
            end
            %calculate the thermal strain
            for k=1:ne
                [ETHt,alpha]=thermal1d(PR(k),tin);
                ETH(k)=ETHt;
                alphaT(tin,k)=alpha;
            end
            break
        end
    end
    if tr==1
        break
    end
    IT(tin)=it;UT(tin,:)=U0';
    ET(tin,:)=E';ST(tin,:)=S';
    ECT(tin,:)=EC';PRT(tin,:)=PR';
    ETHT(tin,:)=ETH';
end

%--------------------postprocessor-----------------------
%compare the FEM solution uh and exact solution ue
save S83-2005 UT ET ST ECT ETHT PRT VIST KCT SST GT alphaT hi;
drawerr1d(IT,UT,ET,ST,ECT,ETHT,PRT,VIST,KCT,SST,GT,alphaT,hi);
disp(GT(tmax,ne))
%--------------subroutines-----------------------------
%%%[sinsolver1d.m] end%%%

%%%[ge1d.m] start%%%
function [xy, NT, bount, int, IB, nn, ne]=ge1d(hi, sh)
%---------------------------------------------------------------------------
%generate nodes and elements in 1-D
%coordinates for nodes:   xy(nn, 1)
%element index:           NT(ne,1:2)
%define boundary nodes:   bound(1:nb)
%define interior nodes:   int(1:ni)
%mark the boundary nodes: IB(1:nn) 0->not boundary;1->displacement;2->force
%total node number:     nn;
%total element number:  ne;
%boundary nodes number: nb;
```

```
%interior nodes number: ni;
%initial height of cylinder (m):        hi;
%number of elements along the height:   sh;
%
%Copyright Rui Zhang @ PennState 2005
%contact:<rzhang@psu.edu>
%-------------------------------------------------------------------------

global xy NT IB time dt tmax

ne=sh; le=hi/ne; nn=ne+1;
for i=1:nn
   xy(i,1)=i*le-le;
end
for i=1:ne
   NT(i,1)=i; NT(i,2)=i+1;
end
bount(1)=1; bount(2)=nn; nb=2; ni=nn-nb;
for i=1:ni
   int(i)=i+1;
end
IB(1:nn)=0;IB(1)=1;IB(nn)=2;
%%%[ge1d.m] end%%%

%%%[stiff1d.m] start%%%
function [A,R,E,S,PR]=stiff1d(U0,EC,ETH,tin)
%-------------------------------------------------------------------------
%calculate the stiffness matrix 'A' and load vector 'b' for 1-D
%
% subroutines:
% elm_stiff_1d.m
%
%Copyright Rui Zhang @ PennState 2005
%contact:<rzhang@psu.edu>
%-------------------------------------------------------------------------
global xy NT IB time dt tmax
[nn, trash]=size(xy); [ne, trash]=size(NT);
%total node number:     nn;
%total element number:  ne;

%initialization
A(1:nn,1:nn)=0;R(1:nn)=0;R=R';E(1:ne)=0;E=E';
S=E;PR=E;

for k=1:ne
  n1=NT(k,1);n2=NT(k,2);
  x1=xy(n1,1);x2=xy(n2,1);
  UE0=[U0(n1) U0(n2)]';
  %calculate the element stiffness matrix
  [AE,RE,EE,SE,PRE]=elm_stiff_1d(k,x1,x2,UE0,EC(k),ETH(k),ne,tin);
  %assemble stiffness
  m1=NT(k,1:2);m2=NT(k,1:2);
  A(m1,m2)=A(m1,m2)+AE(1:2,1:2);
  %assemble residual
```

```
  m1=NT(k,1:2);
  R(m1)=R(m1)+RE(1:2);
  %assemble strain & stress
  E(k)=E(k)+EE;
  S(k)=S(k)+SE;
  PR(k)=PR(k)+PRE;
end
%%%[stiff1d.m] end%%%

%%%[elm_stiff_1d.m] start%%%
function [AE,RE,E0,S0,PRE]=elm_stiff_1d(k,x1,x2,UE0,EC0,ETH0,ne,tin)
%--------------------------------------------------------------------------
%calculate the element residual and stiffness matrix in 1-D
%
%Copyright Rui Zhang @ PennState 2005
%contact:<rzhang@psu.edu>
%--------------------------------------------------------------------------

global xy NT IB time dt tmax

%initialization
AE=zeros(2);RE=zeros(2,1);

EM=200e9;           %elastic modulus, Pa
NU=.28;             %Poisson's ratio
PR0=1-.8169;            %intial porosity
DENT=7.82e3;        %theoretical density, kg/m^3
g=-9.8;             %gravity acceleration, N/kg

%length of linear element
le0=x2-x1;
J=le0/2;%Jacobi: determinant of deformation gradient F=dx/dr
%Gauss integral
GSN=2;r1(1)=-1/sqrt(3);w(1)=1;r1(2)=1/sqrt(3);w(2)=1;
rr1=1;ww=1;jx=1;

%shape function
%N1=(1-r1(i))/2.0; N2=(1+r1(i))/2.0;N=[N1 N2];
dN1=-.5;dN2=.5;%dN/dr
NN1=(1-rr1)/2.0; NN2=(1+rr1)/2.0;NN=[NN1 NN2];
%nonlinear stress vector
BI=[dN1 dN2]/J;
%BII=.5*[dN1^2 dN2^2]/J;
%BNL=BI+BII;
BNL=BI;%linear
%geometric vector
G=[dN1*2/le0 0;0 dN2*2/le0];%dN/dX
%G=[dN1 0;0 dN2];

%strain and stress from previous increment
E0=BNL*UE0; S0=(E0-EC0-ETH0)*EM;
%element stress matrix
SM=[S0 0;0 S0];
```

```
%update porosity and relative density
PRE=(PR0+E0)/(1+E0);RD=1-PRE;
dRD=-(1-PR0)*BNL/(1+E0)^2;

%body force -- checked with the analytical solution ul=2.7589e-11 -- passed
bx=RD*DENT*g;dbx=dRD*DENT*g;
%rod pressure -- checked -- passed
tp=-2E1;

for i=1:GSN
   N1=(1-r1(i))/2.0; N2=(1+r1(i))/2.0;N=[N1 N2];
   %calculate the residual
   RE=RE+(BNL'*S0-N'*bx)*w(i)*J;
   %calculate the stiffness
   AE1=BNL'*EM*BNL*w(i)*J;
   AE2=G'*SM*G*w(i)*J;
   AE3=-N'*dbx*w(i)*J;
   AE=AE+AE1+AE2+AE3;
   %AE=AE+AE1+AE3;%linear
end

if k==ne
   RE=RE-NN'*tp*ww*jx;
end
%%%[elm_stiff_1d.m] end%%%

%%%[grain1d.m] start%%%
function dG=grain1d(tin,G)
%--------------------------------------------------------------------------
%calculate the grain size for 1-D
%
%Copyright Rui Zhang @ PennState 2005
%contact:<rzhang@psu.edu>
%--------------------------------------------------------------------------

global xy NT IB time dt tmax

TEMP=temp1d(tin);
TEMP0=temp1d(tin-1);
%grain growth activation energy
Qg=315.8e3;
if TEMP>=1200
   Qg=50e3;
end
A=3.75e-13;%pre-exponential factor
m=1;%index
R=8.314;%gas constant
dG=dt*A*exp(-Qg/R/(TEMP+273))/G^m;

%no grain growth in cooling period
if TEMP < TEMP0
   dG=0;
end
%%%[grain1d.m] end%%%
```

```
%%%[creep1d.m] start%%%
function [dEC,VIS,KC,SS]=creep1d(S0,PR,G,tin)
%--------------------------------------------------------------------------
%calculate the creep strain increment
%subroutine: temp1d.m
%
%Copyright Rui Zhang @ PennState 2005
%contact:<rzhang@psu.edu>
%--------------------------------------------------------------------------

global xy NT IB time dt tmax

%define parameters
pre=6.4e9;          %pre-exponential factor of viscosity, Pa*s
Q=20.0e3;           %viscous activation envergy, N*m
R=8.314;            %gas constant,
SET=1.5;            %surface tension energy, J/m^2
Gr=G/2;             %grain/particle radius, m

%apply sintering cycle
TEMP=temp1d(tin);    %Celsius degree, C
TEMP0=temp1d(tin-1);

%calculate viscosity
VIS=pre*exp(Q/R/(TEMP+273)); %viscosity at TEMP
KC=4/3*(1-PR)^3*VIS/PR; %bulk viscosity modulus
%GC=(1-PR)^2*VIS; %shear viscosity modulus

%define sintering stress and transition temperature
%transition temperature S83:918; M83:958; L83:983
if TEMP>=918 %transition temperature for S83
   SS=3*SET*(1-PR)^2/Gr; %sintering stress
else
   SS=0;
end

%zero sintering stress in cooling period
if TEMP < TEMP0
   SS=0;
end
dEC=dt*(S0-3*SS)/9/KC;
%%%[creep1d.m] end%%%

%%%[thermal1d.m] start%%%
function [ETHt,alpha]=thermal1d(PR,tin)
%--------------------------------------------------------------------------
%calculate the thermal strain
%
%Copyright Rui Zhang @ PennState 2005
%contact:<rzhang@psu.edu>
%--------------------------------------------------------------------------

global xy NT IB time dt tmax time_s temp_s
```

```
%thermal expansion coefficient
T0=18;            %reference temperature
TEMP=temp1d(tin);  %current temperature

%empirical equation for TEC(from M83)
A=4.47e-9/0.8184;B=1.21e-5/0.8184;
alpha0=A*TEMP+B;
alpha=alpha0*(1-PR);
ETHt=alpha*(TEMP-T0);
%%%[thermal1d.m] end%%%

%%%[temp1d.m] start%%%
function TEMP=temp1d(tin)
%--------------------------------------------------------------------------
%apply sintering cycle:
%heating rate 10C/min from 18 to 1350
%holding period 60 mins
%cooling rate 10C/min from 1350 to 18
%
%Copyright Rui Zhang @ PennState 2005
%contact:<rzhang@psu.edu>
%--------------------------------------------------------------------------

global xy NT IB time dt tmax time_s temp_s

%apply sintering cycle of medium group sample
[n1,n2]=size(time_s);

if tin~=tmax
   ct=dt*tin;
else
   ct=time;
end

for i=1:n1
   t1=time_s(i)*60;t2=time_s(i+1)*60;
   if ct <= t2
      TEMP=temp_s(i)+(ct-t1)*(temp_s(i+1)-temp_s(i))/(t2-t1);
      break
   end
end
%%%[temp1d.m] end%%%

%%%[drawerr1d.m] start%%%
function drawerr1d(IT,UT,ET,ST,ECT,ETHT,PRT,VIST,KCT,SST,GT,alphaT,hi)
%--------------------------------------------------------------------------
%draw the error between FEM solution
%subroutine: temp1d.m
%
%Copyright Rui Zhang @ PennState 2005
%contact:<rzhang@psu.edu>
%--------------------------------------------------------------------------
```

```
global xy NT IB time dt tmax

[nn, trash]=size(xy); [ne, trash]=size(NT);
dt=(time-dt)/(tmax-1);

%draw the sintering cycle
t=zeros(1,tmax);t(1:tmax-1)=dt*(1:tmax-1);t(tmax)=time;
TEMP=zeros(1,tmax);
for i=1:tmax
   TEMP(i)=temp1d(i);
end
subplot(4,5,1);plot(t,TEMP,'b-');
grid on;axis on;
xlabel('time (s)');ylabel('temperature(C)');

%draw the shrinkage solution
u(1:tmax)=0;
u(:)=UT(:,nn);
sk=-100*u/hi;
subplot(4,5,2);load diladata_S83_M83_L83;
plot(t,sk,'b-',time_s*60,shrink_s,'r-');
grid on;axis on;
xlabel('time (s)');ylabel('vertical shrinkage route (%)');
femt=t'/3600;TEMPfem=TEMP';skfem=sk';
save S83-time-fem.txt femt -ASCII
save S83-temp-fem.txt TEMPfem -ASCII
save S83-shrink-fem.txt skfem -ASCII
dilatime=time_m/60;
save S83-time-dila.txt dilatime -ASCII
save S83-temp-dila.txt temp_s -ASCII
save S83-shrink-dila.txt shrink_s -ASCII

%draw the convergent route
a=1:tmax;
subplot(4,5,3);plot(a,IT,'.-');
xlabel iterations, ylabel residua, grid on;

%----------function of time----------%
%draw the total strain
u(1:tmax)=0;u(:)=ET(:,ne);
subplot(4,5,6);plot(t,u,'.-');
grid on;
ylabel('total strain');xlabel('time(s)');

%draw the creep strain
u(:)=ECT(:,ne);
subplot(4,5,7);plot(t,u,'.-');
grid on;
ylabel('creep strain');xlabel('time(s)');

%draw the thermal strain
u(:)=ETHT(:,ne);
subplot(4,5,8);plot(t,u,'.-');
grid on;
```

```
ylabel('thermal strain');xlabel('time(s)');

%draw the stress
u(:)=ST(:,ne);
subplot(4,5,9);plot(t,u,'.-');
grid on;
ylabel('stress (Pa)');xlabel('time(s)');

%draw the density
RD=zeros(1,tmax);RD(:)=1-PRT(:,ne);
subplot(4,5,10);plot(t,RD,'.-');
grid on;
ylabel('relative density');xlabel('time(s)');

%----------function of temp----------%
%draw the total strain
u(1:tmax)=0;u(:)=ET(:,ne);
subplot(4,5,11);plot(TEMP,u,'.-');
grid on;
ylabel('total strain');xlabel('temp(C)');

%draw the creep strain
u(:)=ECT(:,ne);
subplot(4,5,12);plot(TEMP,u,'.-');
grid on;
ylabel('creep strain');xlabel('temp(C)');

%draw the thermal strain
u(:)=ETHT(:,ne);
subplot(4,5,13);plot(TEMP,u,'.-');
grid on;
ylabel('thermal strain');xlabel('temp(C)');

%draw the stress
u(:)=ST(:,ne);
subplot(4,5,14);plot(TEMP,u,'.-');
grid on;
ylabel('stress (Pa)');xlabel('temp(C)');

%draw the density
RD=zeros(1,tmax);RD(:)=1-PRT(:,ne);
subplot(4,5,15);plot(TEMP,RD,'.-');
grid on;
ylabel('relative density');xlabel('temp(C)');

%----------creep related parameters----------%
%draw the viscosity
subplot(4,5,4);plot(t,VIST(:,ne),'.-');
grid on;
ylabel('viscosity');xlabel('time(s)');

%draw the viscosity
subplot(4,5,5);plot(TEMP,VIST(:,ne),'.-');
grid on;
```

```
ylabel('viscosity');xlabel('temp(C)');

%draw the bulk viscosity modulus
subplot(4,5,16);plot(t,KCT(:,ne),'.-');
grid on;
ylabel('bulk viscosity modulus');xlabel('time(s)');

%draw the bulk viscosity modulus
subplot(4,5,17);plot(TEMP,KCT(:,ne),'.-');
grid on;
ylabel('bulk viscosity modulus');xlabel('temp(C)');

%draw the sintering stress
subplot(4,5,18);plot(t,SST(:,ne),'.-');
grid on;
ylabel('sintering stress(Pa)');xlabel('time(s)');

%draw the sintering stress
subplot(4,5,19);plot(TEMP,SST(:,ne),'.-');
grid on;
ylabel('sintering stress (Pa)');xlabel('temp(C)');

%draw the grain/particle size
subplot(4,5,20);plot(TEMP,GT(:,ne),'.-');
grid on;
ylabel('grain/particle size (m)');xlabel('temp(C)');

%----------------comparison on the grain size----------------%
figure(2)
SST0=SST;GT0=GT;sk0=sk;
load S83-2005;
u1(1:tmax)=0;u1(:)=UT(:,nn);
sk2=-100*u1/hi;SST2=SST;GT2=GT;

subplot(4,1,1);
plot(time_s*60,shrink_s,'r-',t,sk2,'k.--',t,sk0,'b.-')
grid on;axis on;hold on;
xlabel('time (s)','FontSize',12);
ylabel('vertical shrinkage route (%)','FontSize',12);
legend('experiment:grain=53e-6m','solu-1d-04-01','current',-1)

subplot(4,1,2);
plot(t,SST2(:,ne),'k.-',t,SST0(:,ne),'b.-');
grid on;ylabel('sintering stress(Pa)');
legend('originalsi:grain=53e-6m','solu-1d-04-01','current',-1)

subplot(4,1,3);
%plot(t,GT1(:,ne),'b.-',t,GT2(:,ne),'k.-',t,GT0(:,ne),'m.-');
plot(t,GT2(:,ne),'k.-',t,GT0(:,ne),'b.-');
grid on;
ylabel('grain/particle size (m)');
%legend('originalsi:grain=53e-6m','solu-1d-03-02','current',-1)
legend('solu-1d-04:grain=53e-6m','current',-1)
```

```
subplot(4,1,4);plot(t,TEMP,'b.-');
grid on;axis on;hold on;
ylabel('temperature(C)');xlabel('time(s)')
legend('sintercycl:grain=53e-6m',-1)
%---------------shrinkage comparison----------------------%
figure(3)
subplot(2,1,1);
plot(time_s*60,shrink_s,'r-',t,sk2,'k.--',t,sk,'b.-');
grid on;axis on;
xlabel('time (s)','FontSize',12);
ylabel('vertical shrinkage route (%)','FontSize',12);
legend('experiment:grain=33e-6m','solu-1d-04','current',-1)

subplot(2,1,2);
plot(temp_s,shrink_s,'r-',TEMP,sk2,'k.--',TEMP,sk,'b.-');
grid on;axis on;box off
xlabel('temperature (C)','FontSize',12);
ylabel('vertical shrinkage route (%)','FontSize',12);
legend('experiment:grain=33e-6m','solu-1d-04','Modifed',-1)
%----------------------S83--------------------------%
figure(4)
subplot(1,2,1);plot(t/3600,GT0(:,ne)*1e6,'b-');
grid on;axis on;box off;ylim([0 30]);
xlabel('time (hour)','FontSize',24);
ylabel('grain size (micron)','FontSize',24);

subplot(1,2,2);plot(TEMP,GT0(:,ne)*1e6,'b-');
grid on;axis on;box off;ylim([0 30]);
xlabel('temperature (C)','FontSize',24);
ylabel('grain size (micron)','FontSize',24);
%%%[drawerr1d.m] end%%%
```

B.3 ABAQUS Input File and Subroutine

B.3.1 Sintering Simulation

```
***input_file_start***
*HEADING
--------------------------------------------------------------------------
SHRINKAGE MODEL FOR SINTERING of S83(2-D with Thermal Expansion, element CAX4T)
Copyright Rui Zhang @ PennState 2005
contact:<rzhang@psu.edu>
--------------------------------------------------------------------------
**--------------------
**to generate nodes for cylindrical sample
**--------------------
**
*NODE
```

```
101,0.0,0.0,0.0
121,0.006,0.0,0.0
3101,0.0,0.01198,0.0
3121,0.006,0.01198,0.0
**
*NGEN,NSET=BOTTOM
101,121,10
*NGEN,NSET=TOP
3101,3121,10
*NFILL,NSET=ALL
BOTTOM,TOP,3,1000
**
**-----------------------------------------
**to generate node sets to identify axis,etc.
**-----------------------------------------
**
*NSET,NSET=AXIS,GENERATE
101,3101,1000
*NSET,NSET=EDGE,GENERATE
121,3121,1000
**
**---------------------------------------------------
**to generate 8-node biquadratic, axisymmetric elements
**---------------------------------------------------
**
*ELEMENT,TYPE=CAX4T
101,101,111,1111,1101
*ELGEN,ELSET=ALL
101,2,10,1,3,1000,1000
**
**---------------------------------------------------
**to generate element sets to identify boundary conditions
**---------------------------------------------------
**
*ELSET,ELSET=OUTEDGE,GENERATE
102,2102,1000
*ELSET,ELSET=BOT,GENERATE
101,102,1
*ELSET,ELSET=TOP,GENERATE
2101,2102,1
**----------------------------
**to define material property
**----------------------------
**
*SOLID SECTION,ELSET=ALL,MATERIAL=SS316
*MATERIAL,NAME=SS316
*ELASTIC
196E9,0.28
*EXPANSION, ZERO=21.4
12.55E-6,121.4
12.99E-6,221.4
*CONDUCTIVITY
14.6,20
*DENSITY
```

```
6.0E3,18
*CREEP, LAW=USER
*SWELLING, LAW=USER
*DEPVAR
8
**------------------------------
**to define initial conditions
**------------------------------
*INITIAL CONDITIONS, TYPE=TEMPERATURE
ALL,21.4
*INITIAL CONDITIONS, TYPE=STRESS
   1, -10.4681E+06,      -61.09E+03,    -10.4695E+06,     190.894E+03
   2, -6.76407E+06,     25.8974E+03,     -6.7791E+06,     260.134E+03
   3, -3.75675E+06,     254.834E+03,    -3.76645E+06,     222.629E+03
…… (continue adding data in the same pattern)
**
**-------------------------------
**specifying boundary conditions
**-------------------------------
**
*BOUNDARY
AXIS,XSYMM
BOTTOM, 2
**
**------------------------
**analysis of the model
**------------------------
**
*RESTART,WRITE,FREQUENCY=100
**
*STEP,INC=7000
**     STEP 1 ------- SINTERING (CREEP)
*COUPLED TEMPERATURE-DISPLACEMENT, CETOL=5.E-6, DELTMX=20.0
2,19753., 1.E-15, 30
*AMPLITUDE,NAME=TEMP,INPUT=realt.dat,TIME=TOTAL TIME
*BOUNDARY,AMPLITUDE=TEMP
ALL,11,,1
*DLOAD
TOP, P3, -0.05
ALL, GRAV, 9.8, 0, -9.8, 0
**-------------------------------------
**output the selected result into *.dat
**-------------------------------------
*ELSET, ELSET=OTE
2101
*NSET, NSET=OTN
3111
*EL PRINT, ELSET=ALL, FREQUENCY=7000
E
EE
CE
EP
*NODE PRINT, NSET=TOP, FREQUENCY=1
U1,U2
```

```
*NODE PRINT, NSET=ALL, FREQUENCY=7000
COORD
*EL PRINT, ELSET=OTE, FREQUENCY=7000
SDV2,SDV6,SDV7,SDV8
**----------------------------------
*OUTPUT,HISTORY
*NODE OUTPUT, NSET=OTN
U2
*ELEMENT OUTPUT, ELSET=OTE
SDV1,SDV2,SDV3,SDV4,SDV5,SDV6,SDV7,SDV8,TEMP
*END STEP
**------------------------
***input_file_end***

***subroutine_start***
C  ************************************************************
C  FOR CREEP LAW
C  ************************************************************
      SUBROUTINE CREEP(DECRA,DESWA,STATEV,SERD,EC0,ESW0,P,QTILD,
     1 TEMP,DTEMP,PREDEF,DPRED,TIME,DTIME,CMNAME,LEXIMP,LEND,
     2 COORDS,NSTATV,NOEL,NPT,LAYER,KSPT,KSTEP,KINC)
C
      INCLUDE 'ABA_PARAM.INC'
C
C     FIND REFERENCE IN USER MANUAL VOLUME III PAGE25.2.1-1
C
      CHARACTER*80 CMNAME
C
      DIMENSION DECRA(5),DESWA(5),STATEV(*),PREDEF(*),DPRED(*),TIME(2),
     1 COORDS(*)
C
      DO 3 KK=1,5
       DECRA(KK)=0.D0
3           DESWA(KK)=0.D0
C
C  INITIALIZE THE PARAMETER
C
       G0=4.31D-6
            GAMMA=6.75D-13
       R=8.314
       M=1.0
            IF (TEMP .GE. 1200) THEN
              QG=50D+3
            ELSE
              QG=315.8D+3
            ENDIF
       G=STATEV(2)
C INITIAL GRAIN SIZE FOR L83
       IF (KINC .EQ. 1) G=G0
C UPDATE GRAIN SIZE G PER INCREMENT
       IF (KINC .NE. STATEV(3)) THEN
         DG=DTIME*GAMMA*EXP(-QG/(R*(TEMP+273)))/G**M
         IF (TEMP .LT. STATEV(5)) THEN
                      DG=0
```

```
                ENDIF
                G=G+DG
          ENDIF

C APPLIED THE TRANSITION TEMPERATURE
     IF (TEMP .GE. 918) THEN
          SURFACE=1.5
     ELSE
       SURFACE=0
     ENDIF
C          IF (TEMP .LT. STATEV(5)) THEN
C            SURFACE=0
C          ENDIF
C
          VISO0=7.9D08
          Q=20.0D+3
          GRAIN=G
C
C  UPDATE PARAMETER
C  STATEV(7)=EPII
C
          IF (KSTEP .EQ. 1 .AND. KINC .EQ. 1) THEN
C  INITIALIZE THE RELATIVE DENSITY
       IF (NOEL.EQ.   1.AND.NPT.EQ. 1) THEN
       DENSITY=0.8151
      ELSE IF (NOEL.EQ.   1.AND.NPT.EQ. 2) THEN
       DENSITY=0.8151
      ELSE IF (NOEL.EQ.   1.AND.NPT.EQ. 3) THEN
       DENSITY=0.8151
      ELSE IF (NOEL.EQ.   1.AND.NPT.EQ. 4) THEN
       DENSITY=0.8151
      ELSE IF (NOEL.EQ.   2.AND.NPT.EQ. 1) THEN
       DENSITY=0.8147
      ELSE IF (NOEL.EQ.   2.AND.NPT.EQ. 2) THEN
       DENSITY=0.8147
      ELSE IF (NOEL.EQ.   2.AND.NPT.EQ. 3) THEN
       DENSITY=0.8147
      ELSE IF (NOEL.EQ.   2.AND.NPT.EQ. 4) THEN
       DENSITY=0.8147
        ……(add data in the same pattern)
       ENDIF
           ELSE
       IF (NOEL.EQ.   1.AND.NPT.EQ. 1) THEN
       DENSITY0=0.8151
            DENSITY=DENSITY0*EXP(-ESW0)
           ……(add data in the same pattern)
        ENDIF
           ENDIF
           PORE=1-DENSITY
           VISO=VISO0*EXP(Q/(R*(TEMP+273)))
C
C  CREEP
C
    DECRA(1)=QTILD*DTIME/(3.*VISO*(1-PORE)**2)
```

```
      IF(QTILD.EQ.0) QTILD=1.E-6
      DECRA(5)=DECRA(1)/QTILD
C
C  SWELLING
C
      TERM1=P*PORE/(VISO*(1-PORE)**3)
      TERM2=3*SURFACE*PORE/(VISO*GRAIN*(1-PORE))
      DESWA(1)=-3./4.*(TERM1+TERM2)*DTIME
      IF(P.EQ.0) P=1.E-6
      DESWA(4)=-3./4.*TERM1/P*DTIME
C
C  UPDATE SOLUTION DEPENDENT VARIABLES
            STATEV(1)=ESW0
            STATEV(2)=GRAIN
      STATEV(3)=KINC
            STATEV(4)=DTIME
            STATEV(5)=TEMP
            STATEV(6)=VISO
            STATEV(7)=3*SURFACE*(1-PORE)**2/(GRAIN/2)
            STATEV(8)=DENSITY
      RETURN
      END
***subroutine_end***
```

B.3.2 Compaction Simulation

```
***input_file_start***
*HEADING
ABAQUS job created for 6.3, CAP MODEL FOR SS316L-M83
one punch compaction analysis of ss316l
initial density=apparent density 0.381
final density=greeen density 0.813
friction=0.05
user subroutines:
'uvarm'---------relative density output
##step 1: pressing
Copyright by Rui Zhang@ Penn State University
Dec.08 2002
**_____________________________________
** Reference Nodes Generation
**_____________________________________
**_____________________________________
** Node Generation
**_____________________________________
**_____________________________________
**Node Set Generation
**_____________________________________
**_____________________________________
**ELEMENT GENERATION
**_____________________________________
```

```
**
**--------------------------------
**surface definitaion
**--------------------------------
**
*SURFACE, NAME=TSUR
TOP,S4
*SURFACE,NAME=ESUR
EDGE,S3
*SURFACE,NAME=BSUR
BOTTOM,S2
*SURFACE,NAME=UPUNCH,TYPE=SEGMENTS
START,0.0061,0.025776
LINE,-0.0001,0.025776
*SURFACE,NAME=DIEWALL,TYPE=SEGMENTS
START,0.006,-0.001
LINE, 0.006, 0.025776
CIRCL,0.0065,0.026276,0.0065,0.025776
LINE, 0.007, 0.026276
**small circular arc, radius=0.5mm, angle=90
*SURFACE,NAME=LPUNCH,TYPE=SEGMENTS
START,-0.001,0.
LINE,0.0061,0.
**--------------------------------
**rigid body surface definitaion
**--------------------------------
*RIGID BODY, REF NODE=9999, ANALYTICAL SURFACE=UPUNCH
*RIGID BODY, REF NODE=9998, ANALYTICAL SURFACE=DIEWALL
*RIGID BODY, REF NODE=9997, ANALYTICAL SURFACE=LPUNCH
**--------------------------------
**contact pair definitaion
**--------------------------------
*CONTACT PAIR,INTERACTION=SMOOTH1
TSUR,UPUNCH
*CONTACT PAIR,INTERACTION=SMOOTH2
BSUR,LPUNCH
*CONTACT PAIR,INTERACTION=SMOOTH3
ESUR,DIEWALL
*SURFACE INTERACTION,NAME=SMOOTH1
*FRICTION
0.05
*SURFACE INTERACTION,NAME=SMOOTH2
*SURFACE BEHAVIOR,NO SEPARATION
*FRICTION
0.05
*SURFACE INTERACTION,NAME=SMOOTH3
*FRICTION
0.05
**CONSTANT FRICTION COEFFICIENT
**________________________________________
**INITIAL CONDITION
**________________________________________
**APARENT DENSITY
*INITIAL CONDITIONS, TYPE=RATIO
ALL, 1.625
```

```
*INITIAL CONDITIONS, TYPE=STRESS, GEOSTATIC
ALL, -500, 0.0, -500, 0.025776, 1.0
**_____________________________________
**MATERIAL PROPERTY DEFINITION
**_____________________________________
*SOLID SECTION, ELSET=ALL, MATERIAL=SS316L
*MATERIAL, NAME=SS316L
**ELASTIC PROPERTIES
*POROUS ELASTIC
0.01, 0.35
**PLASTIC PROPERTIES
*CAP PLASTICITY
0.01E6, 70.42, 0.50, 0.01, 0.05, 1.0
*CAP HARDENING
0.015E6, 0
7.88E6, 0.01
8.32E6, 0.02
9.29E6, 0.04
10.37E6, 0.06
11.57E6, 0.08
12.92E6, 0.10
14.42E6, 0.12
16.10E6, 0.14
17.97E6, 0.16
20.06E6, 0.18
22.39E6, 0.20
25.00E6, 0.22
27.91E6, 0.24
31.15E6, 0.26
34.77E6, 0.28
38.82E6, 0.30
43.33E6, 0.32
48.37E6, 0.34
53.99E6, 0.36
60.27E6, 0.38
67.28E6, 0.40
75.10E6, 0.42
83.83E6, 0.44
93.58E6, 0.46
104.46E6, 0.48
116.61E6, 0.50
130.17E6, 0.52
145.30E6, 0.54
162.20E6, 0.56
162.97E6, 0.58
181.06E6, 0.60
225.61E6, 0.62
251.85E6, 0.64
281.13E6, 0.66
313.82E6, 0.68
350.31E6, 0.7
391.04E6, 0.72
436.51E6, 0.74
487.27E6, 0.76
543.93E6, 0.78
```

```
620.00E6, 0.8
*USER OUTPUT VARIABLES
2,
**_____________________________________
**BOUNDARY CONDITION
**_____________________________________
*BOUNDARY
AXIS, XSYMM
9999,1,1
9999,6,6
9998, ENCASTRE
9997,1,1
9997,6,6
**_____________________________________
*RESTART, WRITE, FREQUENCY=1
**---------------------------------
**##step 1: pressing---done
**---------------------------------
*STEP, NLGEOM, UNSYMM=YES, INC=1000
step 1: pressing
*STATIC
0.05, 10.0, 1D-7
*BOUNDARY
9999, 2, , -0.013776
9997, 2
**---------------------------------
**output the selected result into *.dat
**---------------------------------
*EL PRINT, ELSET=ALL, FREQUENCY=1000
VOIDR, UVARM
*EL PRINT, ELSET=ALL, POSITION=AVERAGED AT NODES, FREQUENCY=1000
VOIDR, UVARM
*NODE PRINT, NSET=ALL, FREQUENCY=1000
COORD
**---------------------------------
**output the selected result into *.odb
**---------------------------------
*OUTPUT, FIELD, FREQUENCY=1, OP=ADD
*ELEMENT OUTPUT, ELSET=ALL
UVARM,S,E
*NODE OUTPUT, NSET=ALL
U,RF
*OUTPUT, HISTORY,  OP=ADD
*NODE OUTPUT, NSET=TOP
U2
*ENDSTEP
**_____________________________________
```

input_file_end

subroutine_start

```
C  *********************************************
C  for generating element output
C  *********************************************
      subroutine uvarm(uvar,direct,t,time,dtime,cmname,orname,
```

```
     1 nuvarm,noel,npt,layer,kspt,kstep,kinc,ndi,nshr,coord,
     2 jmac,jmtyp,matlayo,laccfla)
c
      include 'aba_param.inc'
c
      character*80 cmname,orname
      character*8  flgray(15)
      dimension uvar(nuvarm),direct(3,3),t(3,3),time(2),
     * coord(*),jmac(*),jmtyp(*)
      dimension array(15),jarray(15)
c
c Get components of strain from previous increment
c
      call getvrm('E',array,jarray,flgray,jrcd,
     $ jmac, jmtyp, matlayo, laccfla)
      term1=array(1)+array(2)+array(3)
      term2=array(1)*array(2)+array(2)*array(3)+array(1)*array(3)
      term3=array(1)*array(2)*array(3)
      eqistrain=term1+term2+term3
c da is the apparent density
      da=0.381
      uvar(1)=da/(1+eqistrain)
c
c Get void ratio from previous increment
c
      call getvrm('VOIDR',array,jarray,flgray,jrcd,
     $ jmac, jmtyp, matlayo, laccfla)
      uvar(2)=1/(1+array(1))
      if (jrcd .ne. 0) then
       write(6,*) 'request error in usdfld for element number', noel,
     1 'integration point number', npt
      endif
      return
      end
```

subroutine_end

B.3.3 Heat Transfer Simulation

input_file_start

```
*HEADING
using deformed mesh from pressing & spring-back problem(c0307-01&02)
applying sintering cycle
getting temperature field
holding time
by Rui Zhang @ PennState
July 23 2002
**_____________________________________
** Node Generation
**_____________________________________
*NODE
```

```
       1,            0.,      0.00793
      41,            0.,            0.
    1231,         0.006,      0.00793
    1271,         0.006,            0.
*NGEN,NSET=AXIS
1,41,10
*NGEN,NSET=EDGE
1231,1271,10
*NFILL,NSET=ALL
AXIS,EDGE,3,410
**_____________________________________
**Node Set Generation
**_____________________________________
*NSET, NSET=BOTTOM, GENERATE
      41,1271, 410
*NSET, NSET=TOP
       1,1231, 410
**_____________________________________
**ELEMENT GENERATION
**_____________________________________
*ELEMENT, TYPE=DCAX4
       1,       1,       11,      421,      411
*ELGEN, ELSET=ALL
1, 3, 410, 4, 4, 10, 1
*ELSET, ELSET=AXIS, GENERATE
       1,4,1
*ELSET, ELSET=EDGE, GENERATE
    9,12,1
*ELSET, ELSET=TOP, GENERATE
       1,9,4
*ELSET, ELSET=BOTTOM, GENERATE
       4,12,4
**-----------------------------
**material model
**-----------------------------
*SOLID SECTION, ELSET=ALL, MATERIAL=SS316L
*MATERIAL, NAME=SS316L
*DENSITY
6.0E3,18
*CONDUCTIVITY, TYPE=ISO
      .60,          0.
      .63,        100.
      .94,        200.
      .95,        400.
     1.26,        600.
     2.38,        800.
     3.94,       1000.
    10.00,       1200.
    20.00,       1300.
    25.00,       1350.
**
*SPECIFIC HEAT
      440,          0.
      480,        100.
      505,        200.
```

```
      530,        400.
      530,        600.
      520,        800.
      592,       1000.
      625,       1200.
      645,       1300.
      650,       1350.
**-----------------------------
**uniform initial temp
**-----------------------------
*INITIAL CONDITIONS, TYPE=TEMPERATURE
ALL,         18.
**
**-----------------------------
**thermal analysis
**-----------------------------
*STEP, AMPLITUDE=STEP, INC=7000
*HEAT TRANSFER, END=PERIOD, DELTMX=500.
0.1,10405.2,2.E-5,50.
*AMPLITUDE,DEFINITION=TABULAR,NAME=SINCYCLE,TIME=TOTAL TIME
0,18.0, 751.8,54.42, 6937.2,1115.23, 10405.2,1155.62
*BOUNDARY, AMPLITUDE=SINCYCLE
EDGE, 11, ,  1.
BOTTOM, 11, ,  1.
TOP, 11, ,  1.
**sintering cycle applied on 3 edges(need to modify by real condition
in dilatometer)
**axi-symmetric problem
*BOUNDARY
AXIS,XSYMM
**-----------------------------
**output to *.dat & *.fil
**-----------------------------
*NODE PRINT, FREQ=1
NT,
*NODE FILE, FREQ=1
NT,
*EL PRINT, POS=INTEG, FREQ=7000
*EL FILE,  POS=INTEG, FREQ=7000
*END STEP
***input_file_end***
```

Appendix C

Derivation of the Gradient of the Deviatoric Stress Potential

$$
\begin{aligned}
\underline{\mathbf{n}} = \frac{\partial \tilde{\mathrm{q}}}{\partial \underline{\boldsymbol{\sigma}}} &= \sqrt{\frac{3}{2}}\,\frac{\partial \sqrt{\underline{\boldsymbol{\sigma}'}\underline{\boldsymbol{\sigma}'}}}{\partial \underline{\boldsymbol{\sigma}}} && \left(\tilde{\mathrm{q}} = \sqrt{\frac{3}{2}\,\underline{\boldsymbol{\sigma}'}\underline{\boldsymbol{\sigma}'}}\right)\\
&= \sqrt{\frac{3}{2}}\,\frac{\partial \sqrt{\left(\sigma_{\mathrm{ij}} + \mathrm{p}\delta_{\mathrm{ij}}\right)\left(\sigma_{\mathrm{ij}} + \mathrm{p}\delta_{\mathrm{ij}}\right)}}{\partial \sigma_{\mathrm{kl}}}\,\underline{\mathbf{e}}_{\mathrm{k}}\,\underline{\mathbf{e}}_{\mathrm{l}} && \left(\underline{\boldsymbol{\sigma}'} = \underline{\boldsymbol{\sigma}} + p\underline{\mathbf{I}}\right)\\
&= \sqrt{\frac{3}{2}}\,\frac{\partial \sqrt{\sigma_{\mathrm{ij}}\sigma_{\mathrm{ij}} + 2\mathrm{p}\sigma_{\mathrm{ij}}\delta_{\mathrm{ij}} + \mathrm{p}^2\delta_{\mathrm{ij}}\delta_{\mathrm{ij}}}}{\partial \sigma_{\mathrm{kl}}}\,\underline{\mathbf{e}}_{\mathrm{k}}\,\underline{\mathbf{e}}_{\mathrm{l}}\\
&= \sqrt{\frac{3}{2}}\,\frac{\partial \sqrt{\sigma_{\mathrm{ij}}\sigma_{\mathrm{ij}} + 2\mathrm{p}\sigma_{\mathrm{ii}} + \mathrm{p}^2\delta_{\mathrm{ii}}}}{\partial \sigma_{\mathrm{kl}}}\,\underline{\mathbf{e}}_{\mathrm{k}}\,\underline{\mathbf{e}}_{\mathrm{l}} && \left(\delta_{\mathrm{ii}} = 3\right)\\
&= \sqrt{\frac{3}{2}}\,\frac{\partial \sqrt{\sigma_{\mathrm{ij}}\sigma_{\mathrm{ij}} + 2\mathrm{p}\sigma_{\mathrm{ii}} + 3\mathrm{p}^2}}{\partial \sigma_{\mathrm{kl}}}\,\underline{\mathbf{e}}_{\mathrm{k}}\,\underline{\mathbf{e}}_{\mathrm{l}} && \left(\mathrm{p} = -\frac{1}{3}\sigma_{\mathrm{ii}}\right)\\
&= \sqrt{\frac{3}{2}}\,\frac{\partial \sqrt{\sigma_{\mathrm{ij}}\sigma_{\mathrm{ij}} - \frac{2}{3}\sigma_{\mathrm{ii}}\sigma_{\mathrm{jj}} + \frac{1}{3}\sigma_{\mathrm{ii}}\sigma_{\mathrm{jj}}}}{\partial \sigma_{\mathrm{kl}}}\,\underline{\mathbf{e}}_{\mathrm{k}}\,\underline{\mathbf{e}}_{\mathrm{l}}\\
&= \sqrt{\frac{3}{2}}\,\frac{\partial \sqrt{\sigma_{\mathrm{ij}}\sigma_{\mathrm{ij}} - \frac{1}{3}\sigma_{\mathrm{ii}}\sigma_{\mathrm{jj}}}}{\partial \sigma_{\mathrm{kl}}}\,\underline{\mathbf{e}}_{\mathrm{k}}\,\underline{\mathbf{e}}_{\mathrm{l}}\\
&= \sqrt{\frac{3}{2}} \times \frac{1}{2}\,\frac{\dfrac{\partial \sigma_{\mathrm{ij}}\sigma_{\mathrm{ij}}}{\partial \sigma_{\mathrm{kl}}} - \dfrac{1}{3}\dfrac{\partial \sigma_{\mathrm{ii}}\sigma_{\mathrm{jj}}}{\partial \sigma_{\mathrm{kl}}}}{\sqrt{\sigma_{\mathrm{ij}}\sigma_{\mathrm{ij}} - \frac{1}{3}\sigma_{\mathrm{ii}}\sigma_{\mathrm{jj}}}}\,\underline{\mathbf{e}}_{\mathrm{k}}\,\underline{\mathbf{e}}_{\mathrm{l}}
\end{aligned}
$$

where $\underline{\mathbf{e}}_k$ and $\underline{\mathbf{e}}_l$ are unit vectors. Since

$$
\begin{aligned}
\frac{\partial \sigma_{\mathrm{ij}}\sigma_{\mathrm{ij}}}{\partial \sigma_{\mathrm{kl}}} &= \sigma_{\mathrm{ij}}\,\frac{\partial \sigma_{\mathrm{ij}}}{\sigma_{\mathrm{kl}}} + \frac{\partial \sigma_{\mathrm{ij}}}{\sigma_{\mathrm{kl}}}\,\sigma_{\mathrm{ij}}\\
&= \sigma_{\mathrm{ij}}\delta_{\mathrm{ik}}\delta_{\mathrm{jl}} + \delta_{\mathrm{ik}}\delta_{\mathrm{jl}}\sigma_{\mathrm{ij}}\\
&= \sigma_{\mathrm{kl}} + \sigma_{\mathrm{kl}}\\
&= 2\sigma_{\mathrm{kl}}\ ,
\end{aligned}
$$

and

$$\begin{aligned}\frac{\partial \sigma_{ii}\sigma_{jj}}{\partial \sigma_{kl}} &= \sigma_{ii}\frac{\partial \sigma_{jj}}{\sigma_{kl}} + \frac{\partial \sigma_{ii}}{\sigma_{kl}}\sigma_{jj} \\ &= \sigma_{ii}\delta_{jk}\delta_{jl} + \delta_{ik}\delta_{il}\sigma_{jj} \\ &= \sigma_{ii}\delta_{kl} + \delta_{kl}\sigma_{jj} \\ &= 2\delta_{kl}\sigma_{ii},\end{aligned}$$

the result of the gradient of the deviatoric stress potential is

$$\begin{aligned}\underline{\mathbf{n}} = \frac{\partial \tilde{q}}{\partial \underline{\boldsymbol{\sigma}}} &= \sqrt{\frac{3}{2}} \times \frac{1}{2} \frac{\left(2\sigma_{kl} - \frac{2}{3}\delta_{kl}\sigma_{ii}\right)}{\sqrt{\sigma_{ij}\sigma_{ij} - \frac{1}{3}\sigma_{ii}\sigma_{jj}}} \underline{\mathbf{e}}_k \underline{\mathbf{e}}_l \\ &= \sqrt{\frac{3}{2}} \times \frac{1}{2} \frac{2 \times \left(\sigma_{kl} + p\delta_{kl}\right)}{\sqrt{\sigma_{ij}\sigma_{ij} - \frac{1}{3}\sigma_{ii}\sigma_{jj}}} \underline{\mathbf{e}}_k \underline{\mathbf{e}}_l \\ &= \sqrt{\frac{3}{2}} \frac{\left(\sigma_{kl} + p\delta_{kl}\right)\underline{\mathbf{e}}_k \underline{\mathbf{e}}_l}{\sqrt{\underline{\boldsymbol{\sigma}'}\underline{\boldsymbol{\sigma}'}}} \\ &= \sqrt{\frac{3}{2}} \frac{\underline{\boldsymbol{\sigma}'}}{\sqrt{\underline{\boldsymbol{\sigma}'}\underline{\boldsymbol{\sigma}'}}} \\ &= \frac{3\underline{\boldsymbol{\sigma}'}}{2\tilde{q}}.\end{aligned}$$

Appendix D

Summary of Material Parameters in Compaction and Sintering Simulation

The material is stainless steel 316L. Based on different powder particle sizes, 3 groups of samples are categorized. They are referred to using S, M and L designations. Powder characteristics can be found in Table **3.1**.

Material parameters used in the sintering simulation are listed in Table **D.1**.

Table **D.1**: Material Parameters in Sintering Model

Parameter	Input			Data Source
Mean particle size	33.4μm	52.5μm	72.5μm	Measurement
Transition temperature	918°C	958°C	983°C	Measurement
Initial average grain size	4.31μm	5.77μm	5.68μm	Measurement
Elastic modulus	69.3 GPa (82% dense)			[**1**]
Poisson's ratio	0.28			[**1**]
Thermal conductivity	16.0 W/(m °C)			[**1**]
Thermal expansion coefficient	$\alpha = c_1 \mathrm{T} + c_2$ delta T c_1: 4.47×10^{-9} K^{-2} c_2: 12.1×10^{-6} K^{-1}			Measurement
Activation energy of grain growth	315.8 kJ/mol (T<1200°C) 50.0 kJ/mol (T>=1200°C)			[**34**]
Material constant for grain growth	7.39 $\times 10^{-13} m^2/s$	8.80 $\times 10^{-13} m^2/s$	11.7 $\times 10^{-13} m^2/s$	Measurement
Surface tension energy	2.0 J/m^2			[**3**]
Pre-exponential factor of viscosity	770 MPa s	855 MPa s	1010 MPa s	Curve Fitting
Activation energy of viscous flow	20.0 kJ			[**58**]

The material parameters used in the Cap model for the compaction simulation are listed in Table **D.2**. The material parameters used in the porous elasticity model are the

logarithmic elastic bulk modulus, 0.01, and the Poisson's ratio, 0.35. The Cap hardening parameters are listed in Appendix.B.3.2.

Table **D.2**: Material Parameters in CAP Model [44]

Material Cohesion	Material Angel of Friction	Cap Eccentricity Parameter	Transition Surface Radius Parameter	Initial Cap Yield Surface Position	Ratio of the Stress in Tension and Compression
0.01MPa	70°	0.5	0.01	0.05	1.0

The conductivity and specific heat as functions of temperature used in the heat transfer analysis are listed in Appendix B.3.3.

Appendix E

Nontechnical Abstract

This research focuses on the study of the dimensional change during the manufacturing processes of metal powder parts. Industrial products such as gears and filters can be made from loose powders that are pressed tightly in molds. After compaction, the part is weak because the particles are loosely joined. An additional step to bond the particles together occurs when the part is subjected to a sintering cycle—high temperature in a controlled environment. In addition to the part being stronger, it is also denser.

The problem in the sintering process is that while the part becomes denser, it also changes shape and size. These changes may be undesirable if they require extra cost to machine the parts after sintering. The goal of this research is to develop a numerical model that can predict the shape change and thereby reduce the cost. In order to achieve this task, three questions are to be answered. First, how can we link the material characteristics of the problem with the mechanical response. Second, how can we prove that the model is valid and appropriate for this problem. Third, how can we implement the model with a computational approach that can be practiced and verified. All of the three questions have been investigated in this research and the numerical model has been applied to the sintering simulations of cylindrical stainless steel 316L parts. The experimental and numerical results that predict axial shrinkage consistently agree for a range of particle size distribution. The result refines the understanding of sintering and

provides an approach that can be expanded to address complex shapes that are encountered in industrial applications.

VITA

Rui Zhang

Rui Zhang was born in Luoyang, China on May 12, 1976. He received his B.S and M.S. in Engineering Mechanics from Tsinghua University in Beijing, China in 1998 and 2000 respectively. He began to pursue his Ph.D. degree in the Department of Engineering Science and Mechanics at the Pennsylvania State University in 2000.

While a student at Penn State, Mr. Zhang was employed as a graduate research assistant in the Center for Innovative Sintered Products of the Pennsylvania State University since August, 2000. He also served as a graduate teaching assistant where he tutored undergraduates in basic solid mechanics in the 2003-2004 academic year.

His current research interests include viscoelasticity theory, thermal induced creep analysis, numerical simulation on sintering and compaction process, and metallographic analysis on grain growth measurement for porous material. He has presented his work in four conference proceedings. He is an ASME student member.